Master's thesis

NTNU
Norwegian University of Science and Technology
Faculty of Natural Sciences
Department of Chemistry

Yu Liu

Automated Self-Optimising Synthesis Platform for Nanocrystals

Master's thesis in Nanotechnology
Supervisor: Prof. John de Mello
Co-supervisor: Dr. Andrew Harvie
July 2021

NTNU
Norwegian University of
Science and Technology

Yu Liu

Automated Self-Optimising Synthesis Platform for Nanocrystals

Master's thesis in Nanotechnology
Supervisor: Prof. John de Mello
Co-supervisor: Dr. Andrew Harvie
July 2021

Norwegian University of Science and Technology
Faculty of Natural Sciences
Department of Chemistry

NTNU
Norwegian University of
Science and Technology

Preface

This thesis is submitted in partial fulfilment of the requirements for the degree of Master of Science in Nanotechnology at Norwegian University of Science and Technology.

I declare that the contents in this thesis are results of my own work at Department of Chemistry at NTNU, except where specific reference is made. This work includes part of a preliminary project (TKJ4530) carried out in autumn 2020 and masters project (TKJ4905) carried out in spring 2021 under supervision of Professor John de Mello and Dr. Andrew Harvie.

Yu Liu
July, 2021

Abstract

Nanocrystals are semiconductor nanoparticles with proven potential to enhance many applications including bioimaging and optoelectronics. Traditional colloidal synthesis methods typically do not provide the necessary control and uniformity of the reaction conditions needed for reliable reproducibility, resulting in large variations in the size, shape and properties of the nanocrystals. Flow chemistry is an emerging branch of synthetic chemistry that has proven to provide superior control and uniformity in the reaction environment with continuous reagent delivery and production formation. In this report I describe a self-constructed flow platform for high temperature synthesis of copper indium sulphide based photoluminescent nanocrystals. The flow synthesis platform consists self-built components that are interfaced to a PC to achieve synthesis automation with real-time optical detection of the formed products. The inclusion of an on-line analysis system allows for rapid product assessment such one can sample and test multiple reaction conditions within a single reaction run. It also enables self-optimising synthesis in which the reactor automatically finds reactoin conditions that give particles with desired properties by coupling the platform with an optimisation algorithm.

The adaptation of $CuInS_2$ nanocrystal synthesis was done in two-phase flow, with high temperature perfluorinated polyethylene being employed as an inert ''carrier" fluid to enable the formation of two-phase flow, aiming to minimising reactor fouling associated with nanocrystal syntheses. The results showed it is possible to achieve reproducible nanocrystal synthesis using the platform. The approach is inherently scalable for straightforward expansion to the industrial scale. Additionally, sampling experiments showed the reactor is able to rapidly update reaction condition without compromising the desired reproducibility, which gives the user possibility to carry out large self-optimising runs involving experiments for tailored product features.

Self-optimising syntheses were carried out by coupling the platform to a global optimisation algorithm, SNOBFit, with the aim to maximise the emission intensity or achieve a target emission peak wavelength. The algorithm was able to rapidly identify an optimum parameter range that corresponded to the desired high emission as well as synthesis conditions for achieving the targeted wavelength. This allows for tailored products with on-demand capability, which is crucial for applications.

Acknowledgements

Firstly I would like to thank my supervisors Professor John de Mello and Dr. Andrew Harvie for their continuous support and guidance (and their tolerance for my nonsenses) throughout the past year. I would like to thank Sihai Luo, Bicheng Gao and Andrew for making the lab life more enjoyable.

I would also thank my parents for their unconditioned love, support and encouragement throughout my studies. I would like to thank Thea Guldbrandsøy for her honest advices and support as genuine friend. Other big thanks goes to everyone that accompanied me throughout different phases of my study.

My final thank goes to myself for coming through. It's never too far down to come back!

CONTENTS

Preface i

Abstract ii

Acknowledgements iii

1 Introduction 12
- 1.1 Nanocrystals . . . 12
- 1.2 Semiconductor and 0D Quantum Confinement . . . 13
- 1.3 Colloidal Nanoparticle Synthesis . . . 16
- 1.4 Flow Chemistry . . . 18
- 1.5 Automation and Optimisation . . . 21
- 1.6 Summary . . . 23

2 Hardware Development and Flow adaptation 24
- 2.1 Construction of Automated Flow Synthesis Platform . . . 24
  - 2.1.1 Development of the Solid-State Heater . . . 25
  - 2.1.2 Optical Detection Flow Cell . . . 28
  - 2.1.3 Spectrometer Configuration . . . 35
  - 2.1.4 Automated Liquid Separator . . . 40
  - 2.1.5 Delivery System and Refilling Mechanism . . . 44
  - 2.1.6 Automation . . . 47
- 2.2 Batch Synthesis and Adaptation to Flow . . . 49
  - 2.2.1 General Materials . . . 49
  - 2.2.2 Batch Synthesis of $CuInS_2$ and $ZnCuInS_2$ . . . 49
  - 2.2.3 Adapting to Flow . . . 53
  - 2.2.4 Summary . . . 60

3 Rapid Parameter Screening by Automated Synthesis 61
- 3.1 Latin Hypercube Sampling . . . 61
- 3.2 Sampling Experiment 1 . . . 62
- 3.3 Sampling Experiment 2 . . . 70
- 3.4 Summary . . . 73

4 Self-optimising Synthesis of $CuInS_2$ Nanocrystals **75**
4.1 Self-optimisation 75
4.2 2D Intensity Optimisation 75
4.2.1 Experiment 1 76
4.2.2 Experiment 2 79
4.2.3 Experiment 3 82
4.2.4 Experiment 4 85
4.3 Wavelength Optimisation 89
4.4 Summary 93

5 Conclusion and Further Work **94**
5.1 Conclusion 94
5.2 Further Work 96

Bibliography **97**

A Microcontroller Code for Control the Automated Reactor Components **103**

B MATLAB Code for Control the Automated Reactor Components **113**

LIST OF FIGURES

1.1 Schematic representation of the band structure for an insulator, semiconductor and metal at 0 Kelvin. Grey area represent filled valence band and unfilled conduction band is represented by uncoloured area. For semiconductors at 0K, the material dependent band gap ranges from 0.1 K_BT to 100 K_BT 14

1.2 A schematic representation of the possible recombination pathways, green colour indicates non-radiative recombination, and red is radiative recombination 16

1.3 a) LaMer's diagram of Nucleation and Growth, here concentration represents precursor concentration. I) Increasing saturation from unsaturated to critically saturation ($C > C_{min}$ for stable nuclei formation, II)Rapid nucleation occurs, III) Particle growth by diffusion driven process, b) Total Gibbs free energy for nucleation at different temperatures or supersaturation. The critical Gibbs free energy decreases with increasing temperature, T2>T1, same for increasing supersaturation S2>S1 17

1.4 Types of flow: i) Single phase flow of the reagents, channel contact leads to a parabolic flow profile; ii) two-phase segmented flow, the reaction mixture is divided by an immiscible fluid; and iii) droplet flow where the reaction mixture is isolated from the channel walls by the immiscible fluid. 20

1.5 A simple flow chart of an automated flow reactor for self-optimisation, showing reagent delivery to a reactor, followed by on-line analysis of the product. The analysed product information is fed into an optimisation algorithm, in our case SNOBFit. The algorithm will recommend subsequent reaction conditions to perform based on the analysed data, which creates a feedback-loop by interfacing the platform with a PC. 22

2.1 Schematic representation of the automated flow platform for a two-phase nanocrystal synthesis. 24

2.2 Diagrams of the solid-state heater from different perspective. The heater is made of aluminium, with four machined holes for inserting cartridge heating elements. 25
2.3 Previous set-up from the preliminary project. Here, the cooling is loosely attached above the heater with varying positions during operation. 26
2.4 Diagram of the designed enclosure for the heater, with securing for the PC fan at the top. 27
2.5 Temperature ramp of the PID tuned heating system, here the temperature is increases in 50 °C increments and held constant for 10 minutes until next target temperature. 28
2.6 Designed UV-LED based flow cell, here two UV-LEDs are inserted orthogonal to the FEP tube, and Optic fibre is inserted to transfer the emitted photons to the spectrometer. 29
2.7 Full core $CuInS_2$ spectrum recorded with Ocean Optics USB 4000, with 1 minute integration time and 2x 385 nm (25 mW) UV-LED as excitation source. Here the broad saturation region between 385 to 490 nm is due to the LED emission tail, and Quantum dot emission feature is found between 490 to 850 nm. . 29
2.8 ”Zoomed in” core $CuInS_2$ emission spectrum recorded with Ocean Optics USB 4000 with 1 minute integration time and two 385 nm (25 mW) UV-LEDs as excitation source. The quantum dot emission peak is found around 650 nm, and the emission spectrum is contaminated by substantial noise 30
2.9 a) New flow cell that can be attached to the front of laser, the tubing is inserted horizontally and optic fibre on top. b) Technical drawing of the laser from manufacturers data sheet. 31
2.10 Spectrum of the same product as figure 2.8 with 3 seconds integration time and 20 averages, taking a total of 1 minute was taken to perform the complete acquisition. The peak at 800 nm is the second harmonic peak of the laser, which always occurs in the same wavelength range and may be cropped out when analysing the data. 32
2.11 Diagram of the optical detection system. a) Solid-state laser, b) Beam splitter, c)OPT101 Photodiode d) Optic fibre insertion or direct insertion with Ocean Optics USB4000, e) FEP tube insertion. 32
2.12 Recording of the laser beam intensity by photodiode with 0.3 OD filter. The largest variation is observed to be around 7%, and is inconsistent with expectation for a solid-state laser. 34

2.13 a) Block diagram of OPT101, the external RC circuit is connected between pin 2 and 5 such that it bypasses the internal 1 MΩ gain resistor, b) New laser intensity recording with reduced responsitivity, showing $< 1\%$ intensity variation. 34
2.14 Blue) Single dark spectrum with 1 second integration time and thermoelectric disabled, Orange) Single dark spectrum with 1 second integration time and thermoelectric cooling set to -5 °C. Both spectrum were acquired with the QE65000. Here the noise level of cooled spectrum is lower compared to uncooled spectrometer setting. 36
2.15 Comparison between a single dark spectrum and 3000 times averaged dark spectrum. Both spectrum are acquired with QE65000 with with cooling enabled and 1 second integration time. 37
2.16 QE65000 spectrometer wavelength calibration against the mercury line of a fluorescence lamp, showing the spectrometer wavelength had less than 1 nm deviation. 38
2.17 Long pass filter with cut-on wavelength at 480 nm. The % transmission at laser wavelength was found to be 9% by using an absorption spectrometer, optical unfiltered region has a transmission rate around 83%. 39
2.18 a) Laser beam without long pass filter. b) Laser beam intensity with long pass filter. Spectrometer was configured to 8 microsecond integration time. A 85% reduction in the laser intensity was obtained 39
2.19 A typical $CuInS_2$ emission spectra in this work with signal to noise ratio > 290:1. 40
2.20 Annotated photograph of automated separator comprising a machined aluminium separator block for inducing phase separation, a sensor block containing a LED and two photodetector (PDs) for optically monitoring the two output channels, and a motorised needle valve for controlling the back-pressure at the through (T) channel outlet. This through channel configuration was used in this work for separating PFPE carrier fluid and 1-octadecene solvent. Reproduced with permission from Harvie *et al.*[1] 41
2.21 a) Kinematic viscosity of Fomblin 16/6 PFPE fluid at different temperatures. The viscosity is 60 cSt at 40 °C. b) Galden HT270 PFPE fluid at different temperatures. The viscosity is around 2 cSt at 40 °C. Data is taken from Solvay product datasheet. For reference, water has a kinematic viscosity around 0.65 cTs at 40 °C, and 1-octadecene has 3.8 cTs at 40 °C. 43

2.22 Photograph of separator in working condition with Galden HT270/ODE solvent combination at 350 μl/min flor rate. The transparent fluid is Galden HT270 carrier fluid, and the red fluid is synthesised $CuInS_2$ nanocrystals in 1-octadecene solvent. 44
2.23 KD Scientific Legato 210 dual syringe pump with serial communication (also touch screen) used in this work. 45
2.24 a) A schematic representation of the motorised valves, the servo is able to rotate to either infusion or refill (reservoir) upon specific serial commands. b) A flow chart of the refilling process. 46
2.25 An overview of complete automated platform for nanocrystal synthesis. a) KD Scientific pumps, b) motorised valves, c) Galden HT270 stock bottle, d) Precursor reservoir, e) Droplet generator, f) Boxed heater with fan, g) Heater terminal for power supply and PC connection, h) Separator (in fixed pressure mode) and i) Optical detection flow cell. 48
2.26 Schematic representation of the $ZnCuInS_2$ synthesis route. The precursor decomposes under high temperature and results in quantum dot formation. Here the 1-dodecanethiol serves both as a sulphur source and a ligand to prevent product aggregation. . . . 50
2.27 Schematic representation of the $CuInS_2$ synthesis route, in which the zinc precursor has been omitted from the reaction. This reaction occurs much faster due to absence of zinc precursor. . . . 50
2.28 a) Normalised emission spectrum from a series of core $CuInS_2$ QDs synthesis at 218 °C. The first product was collected 80 seconds after the reaction mixture reached 218 °C, subsequent products were taken at 80 second intervals. a) Normalised emission spectra from a series of core/shell $ZnCuInS_2$ QDs synthesis at 218 °C. The first product was collected after 78 minutes, and subsequent products were taken at 3 minutes intervals 51
2.29 Comparison between two flask syntheses with nominally identical synthesis procedures. The emission peak is shifted by 30 nm between the two batches. 52
2.30 A Photograph depicting reacted product droplets exiting the heater. A video of reacted droplets exiting the reactor can be seen here `https://youtu.be/s0EfO08EooM` 54
2.31 Overlaid emission spectra for flask and flow synthesised $ZnCuInS_2$ QDs. Flask product was obtained after 80 minutes reaction time. Flow product was obtained from the reaction after a 22.4 minutes residence time at 220 °C. 54

2.32 Three overlaid spectra from a five-hour synthesis run obtained using a 22.4 residence time at 220 °C. Products were collected at 90 minute intervals. The results show consistent absorption and emission features, indicating stable reactor performance over the five hour runs. 55
2.33 Emission spectrum of core $CuInS_2$ nanocrystals with 3 minutes reaction time at 220 °C in flow. The emission peak is 679 nm. . . 56
2.34 Overlaid emission spectra of core $CuInS_2$ quantum dots obtained using the old and new precursor solutions. For the quantum dots produced with old precursor solution, reaction conditions were set to 180 seconds residence time and 220 °C. For the quantum dots produced with the new precursor solution, the reaction conditions were set to 277 seconds and 160 °C. Here, the emission peak is at the same position, 680 nm, with new precursor solution has a 10 nm wider linewidth and found to be 127nm, the small peak around 500 nm corresponds to the emission of precursor mixture.[2] The emission spectrum for the old precursor product was acquired with a bench top fluorescence spectrometer and had a scanning wavelength from 450 nm to 800 nm, such that the emission spectrum ended at 800 nm. 58
2.35 A schematic illustration of Fomblin induced fouling when channel is experiencing non-uniform heating. Here the viscosity difference is shown in the gradual colour change from red to purple. The product droplet is shown in orange colour, and aggregation zone caused by preferential wetting is shown in black colour. This behaviour occurs as the droplet shape are elongated due to the shear force as flow rate difference caused by different viscosity profile.[3, 4] 59
2.36 A photograph of a fouled tube using Fomblin as a carrier fluid. The black materials are wetted aggregated quantum dots due to long usage. 60

3.1 A graphical representation of a Latin hypercube sampling. Here, the number of variable is a N=2, and the number of points M = 6. N and M form a two-dimensional grid with $M^N = 6^2 = 36$ nodes representing the possible reaction conditions. The nodes marked in red are of the conditions selected for sampling. 62
3.2 Parameter space for Latin Hypercube sampling experiment 1. The red dots are the reaction conditions to be investigated. 63

3.3 Box plot of the emission peak for synthesis conditions. We observe the emission peak variations in each synthesis are within 3 nm error, confirms the desired synthesis reproducibility. 64
3.4 Scatter plot of wavelength and corresponding intensities in each reaction condition in experiment 1. 65
3.5 Box plot of intensity values from sampling experiment 1. Red line is the mean value, with whiskers representing the extreme intensities in each reaction condition. 66
3.6 Normalised laser intensity vs time as determined by uncooled spectrometer and laser diode. The orange line represents the laser intensity recorded by photodiode. The intensity value recorded by the spectrometer drifted by around 20% over an 80-minute recording interval. 67
3.7 Normalised laser intensity vs time recorded with photodiode and a cooled spectrometer, the orange line represents the laser intensity recorded by photodiode. Here the spectrometer CCD detector cooling was set to -5 °C. 68
3.8 Laser intensity measurements recorded by spectrometer and photodiode. Here photodiode recording is indicated in yellow colour. a) The spectrometer was cooled to -8 °C, the measured intensity variation as determined by the spectrometer was around 4%, while according to the photodiode the laser variation was lesser than 1%. Right) The spectrometer was cooled to -10 °C; the intensity measured by spectrometers varies around 4% similar to -8 °C measurement without improvement. 69
3.9 Overlaid data measurements from both cooling temperatures. No clear reduction or trend in intensity variation. 69
3.10 Parameter space for Latin Hypercube sampling experiment 2. The red dots are the reaction conditions to be investigated. 70
3.11 Box plot of the emission peak wavelengths for sampling experiment 2, here we see majority of the wavelengths are highly consistent similar to previous experiment 71
3.12 Scatter plot of wavelength and corresponding intensities in each reaction condition in experiment 2. 72
3.13 Box plot of intensity values from sampling experiment 2 with spectrometer cooling enabled. Red line is the mean value, with whiskers representing the extreme intensities in each reaction condition. 73

4.1 Scatter plot of 30 reaction conditions evaluated during Experiment 1. The optimisation was a 2-dimensional optimisation with varying temperature and residence time. The algorithm preferentially sampled the high temperature region that should provide higher intensity values. 76
4.2 Surface fitted contour plot based on the results from optimisation experiment 1. Lower merit values correspond to higher intensities. 77
4.3 Interpolated 3D contour plot based on the results from optimisation experiment 1. The red marked point highlights the best reaction condition returned by SNOBFit based on the merit values. 77
4.4 Merit values plotted against the measurement number. Here we see measurement 13 and 14 are extremely close. The reaction condition for 13 is 185 °C and 360 seconds, while for 14 the residence time is 140 seconds. 78
4.5 Surface fitted results of Experiment 2, here we have overall smooth surface with two extreme high merit values 80
4.6 Emission spectrum from condition 13 in blue and 14 in red. 80
4.7 Refitted surfaces excluding measurement 13 and 14. Here, we obtain an increasing consistent surface with clear gradual decline towards the blue region. 81
4.8 Surface fitted results from optimisation experiment 3. Here, we observe large merit value variations in the same region. 82
4.9 Surface fit with separated datasets, a) is fitted with first batch of 16 points, and b) is fitted with second batch of 16 points. 83
4.10 A 3D gradfit of the first dataset, with second dataset superpositioned to the fitted surface and is represented in red markers. 84
4.11 Surface fitted results from optimisation experiment 4. Here, we observe overall similar diminishing trend in the merit value as previous experiments. The large local variation being investigated is around 300 seconds residence time and around 170 °C and is marked with red circle. 85
4.12 Merit values against measurement numbers in experiment 4. Again, we observe the periodic search logic represented by merit values. 86
4.13 Overlaid spectra from datapoints around 330 seconds and 170 °C. Measurement number 37 exhibits extremely low emission intensity compared to other measurements in the local region. . . . 87
4.14 Refitted surface excluding measurement 37. Here we see an increasing consistency in the data trend that declines towards high temperatures and reaction times. 88

4.15 Surface fitted results from wavelength optimisation at a targeted wavelength at 675 nm. Here we see an extremely high gradient that is made up by few points at upper parameter limits. Rest of the points are spread in lower temperature region. 89
4.16 Refitted surface without the three extreme measurements. Here we can see the features at the lower temperature region that was previously dominated by the large gradient at upper boundaries. . 90
4.17 Merit values against the measurement number. Here we see four large merit values that corresponds upper parameter range and small merit values suggesting the overall measurements are close to the target peak wavelength. 91
4.18 Overlaid spectra measured during targeted wavelength optimisation experiment at 675 nm. Here we see most of the spectrum have emission peak around 675 nm, close to the target value. However, the intensities varies depending on the exact reaction conditions. . 92

LIST OF TABLES

3.1 Table of emission peak wavelengths measured in the first sampling experiment. The spectrometer cooling was disabled in this experiment. 63
3.2 Table of emission intensity corrected for laser intensity at emission peak in the first sampling experiment. Here, the spectrometer cooling was disabled. In the intensity data, we are obtaining large emission intensity fluctuation with minimum 15%. 65
3.3 Table of emission peak wavelengths measured in the second sampling experiment with spectrometer cooling enabled. 71
3.4 Table of emission intensity corrected for laser intensity at emission peak in the second sampling experiment. Here, the spectrometer cooling is set to -5 °C. 72

CHAPTER 1

INTRODUCTION

1.1 Nanocrystals

Semiconductor nanocrystals, commonly referred as Quantum dots (QDs), are semiconductor nanoparticles with a dimension usually of a few nanometres. The size reduction to the nm-scale often alters the properties and behaviour of a material. Materials that are metals or insulators in their bulk form with continuous energy levels can behave as semiconductor in the nanoscale and exhibit discrete energy levels. This, in turn, leads to interesting properties such the ability to tune photoluminescence (PL) spectra by manipulating the particle size, similar to fluorescence molecules.[5]

Additionally, quantum dots can be functionalised with chemical groups on their surface, leading to tailored chemical properties. This tuneability in the physical and chemical properties enables QDs to be applied in a range of novel applications including, optoelectronics [6], bioimaging[7] and nanomedicine [8]. Quantum dot technology has already made its way to the consumer market, a notable example being commercially available displays.[9] Biological imaging and sensing are application area for QDs due to that use QDs as the emitters.[10] Their tuneable and narrow emission wavelength and high photoluminescence, making them attractive substitutes for traditional fluorescence dyes.[11] In addition, quantum dots are resistant to photobleaching, a common problem with dye-base bio-labels, thus provides longer fluorescence lifetime and more sampling opportunities.[12] QDs can also be functionalised with different chemicals groups for targeted bio-sensing.[13] Moreover, QDs have a broad optical excitation spectrum, which allows them to be used as absorbent material in photovoltaics, thus non-emitting quantum dots are also interesting for applications.[14, 15] Tertiary chalcopyrite $CuInS_2$ based nanocrystals studied in this work are considered to be a benign alternative to cadmium and lead based nanomaterials which are known to be toxic due to their use of heavy metals.[16] This class of nanocrystals have the ability to reach high photoluminescent quantum yield above 80% [17], making them suitable for many of the above mentioned applications. They are especially promising for biological applications due to their absence of heavy metals.[18, 19]

1.2 Semiconductor and 0D Quantum Confinement

This section discusses briefly the underlying physical properties of colloidal nanocrystals and their size dependence.

Semiconductors

Semiconductors are a group of materials having electrical conductivities between insulators and metals at room temperature. Semiconductors can either be pure elements, such as silicon, or compounds such as gallium arsenide or cadmium selenide. For a bulk crystalline material, the atoms are arranged in a periodic fashion with repetition of constituent atoms. Electrons are fermions and obey the Pauli Exclusion Principle, that no two fermions can occupy the same quantum state. A consequence of this is the electron orbitals in two interacting constituent atoms splits into different electron orbitals of different energy that are closely spaced. A bulk material usually contains large number of atoms (N$\sim 10^{22}$), such the number of electron orbitals are very large and are very closely spaced between each other. The energy different between two adjacent levels are so small that they can be considered as a continuum of energy, an energy band. Band gap is the ”forbidden” region in the continuum of electronic states where there are no available energy state. [20]

For a metal at 0 kelvin, electrons are filled up to the Fermi level, that describes the highest energy level filled at 0K, which lies within the continuum of electronic states due to the overlapping energy bands due to delocalised orbitals in metal, such the material is conductive and requires no energy to reach next available state. For both insulators and semiconductors at 0K, there is a gap between a band that is filled with non-conducting electrons, termed the valence band (VB) and the unfilled higher energy band, termed the conduction band (CB). For insulators, the Fermi level lies centrally within the wide gap between the two bands, such that no electrons can reach the next energy band due to the large energy gap. In a semiconductor, the band gap is narrow enough that with sufficient energy, charge carriers can be excited to the conduction band via thermal excitation, and the material is able to conduct under this condition. For an intrinsic semiconductor, the Fermi level lies exactly midway between the conduction and valence band, which is illustrated in figure 1.1.

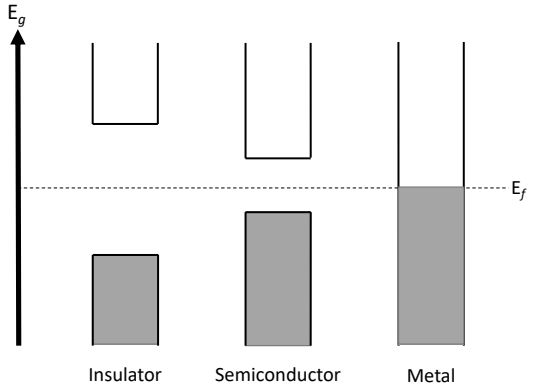

Figure 1.1: Schematic representation of the band structure for an insulator, semiconductor and metal at 0 Kelvin. Grey area represent filled valence band and unfilled conduction band is represented by uncoloured area. For semiconductors at 0K, the material dependent band gap ranges from 0.1 K_BT to 100 K_BT

When an electron is excited from the valence band to the conduction band by thermal excitation or other means, it will create a hole in the valence band. This results in the creation of an electron hole pair termed an exciton, due to the electrostatic attraction of the opposite charge. The exciton tends to relax to a more energy favourable lower state via a recombination event which may be radiative or non-radiative.

When the size of the semiconductor is near or blow the characteristic Bohr radius a_0 ($a_0 = \epsilon_r \frac{m_e}{\mu} a_b$, with ϵ_r, m_e, μ, a_b being respectively the relative permitivity, mass of free electron, reduced mass of exciton and hydrogen Bohr radius, and is typically around 10 nm.), any generated excitons become confined within the material, causing the continuous energy bands observed in bulk materials to become discrete energy states, similar to energy levels in an atom. Thus the band gap, is now the energy gap between ground state and the first excited state for the nano-scaled semiconductor. To find this band gap for spherical nanocrystals, a ''particle in box" treatment with spherical shaped nanocrystal was used here.[21] Solving the time-independent Schrödinger equation for the spherical particles, one obtains the band gap energy for spherical quantum dots:

$$E_{g,QD} = E_{g,bulk} + \frac{\pi^2 \hbar^2}{2\mu r^2} - \frac{1.786 e^2}{\epsilon r} \tag{1.1}$$

Here μ is the reducted mass of exciton ($\mu = \frac{1}{m_e^*} + \frac{1}{m_h^*}$,$m_e^*$ and m_h^* is respectively the effective mass of electron and hole), ϵ the absolute permititvity, and $\hbar$ reduced Plank constant. The two terms has the radius of quantum dots r, and includes both $1/r$ from electrostatic attraction between the charged electron and hole. The important term for small quantum dot is $1/r^2$ size dependence,

which predicts and explains the size dependency of photoluminescence for narrower quantum dots. For smaller quantum dots, the band gap is large, leading to short emission wavelengths. As the quantum dots grow during synthesis, the $1/r^2$ term decreases, and band gap becomes narrower, leading to decreasing energy requirment to excite an electron over the band gap. Therefore, one usually observes increasing emission wavelength in nanocrystals with increasing reaction time and growth.[22]

CuInS2 based quantum dots have a tetrahedral shape [23, 24], which requires very complicated calculations to find the exact energy gap, and equation 1.1 is only useful to approximate the particle sizes.

Photon Emission

In the previous section an expression was derived to find the minimum energy required to excite an electron from the valence band to the conduction band, thereby forming an exciton. For QDs, the energy required to excite an electron typically lies within the visible spectrum. Photons with energy larger than the band gap ($E = \hbar\omega \geq E_{g,qd}$), are absorbed, and lead to exciton formation.

When the exciton recombines by excited electron relaxing back to the VB, a quantised amount of energy that corresponds to the difference in energy between excited state and VB maximum is emitted. The decays occur radiatively or non-radiatively. Radiative recombination means that the energy is emitted in the form of photons, while non-radiative means the energy are emitted into other forms, such as thermal energy. [25, 26]

The excited electrons can relax from many possible energy levels, either from the edges of the bands or within the gap. The ideal case where relaxation occurs from CB minimum to VB maximum is classified as band-edge recombination. However, colloidal nanocrystals are not always formed perfectly, with usually defects within the structure. These defects leads to the formation of intra-gap traps and are common in chalcopyrite nanocrystals.[27] These intra-gap states usually have lower energy states, and therefore emit longer wavelengths compared to band edge recombination. Radiation due to defects is classified as defect state recombination.[28, 29]

Quantum dot diameter are in order of few nanometres, and as a consequence a significant proportion of the constituent atoms are associated to the surface of the nanocrystals.[30] This leads to existence of ‘’dangling bonds”, which are uncoordinated radicals present on the surface. QDs are typically treated with organic ligands, which coordinate these radicals and prevent aggregation which is common to colloidal nanocrystals. Therefore, one would expect increasing emission intensity by coordinating the surface with organic ligands. However, due to steric limitations of the surface, not all dangling bonds can be coordinated.

These uncoordinated surface sites can provide ‘’trap” sites for both electrons and holes, and are often associated with non-radiative recombination as they provide decay pathways for excitons. This usually leads to an undesired reduction in the photoluminescence quantum yield (PLQY).[31] To minimise the surface trapping, the ‘’core” nanocrystals are commonly passivated with a shell material with a close-matching lattice and wider band gap, in order to keep the excitons away from defect rich surface and so to increase the PLQY.[32, 33] Possible recombination pathways are shown in figure 1.2.

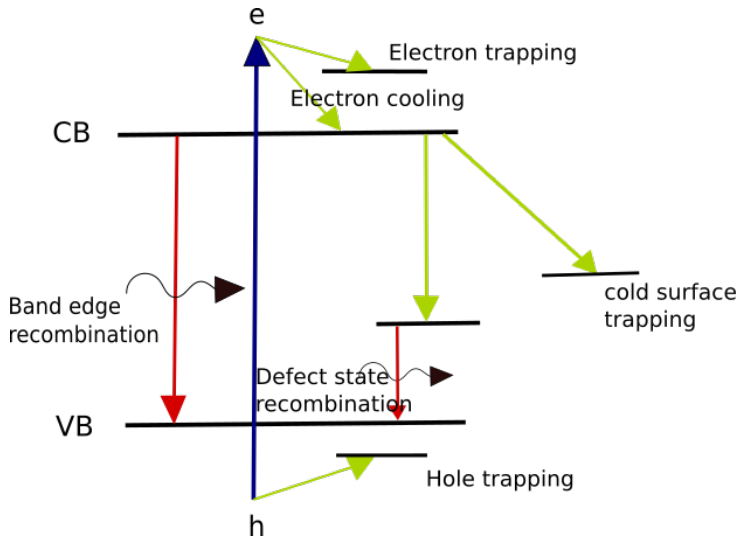

Figure 1.2: A schematic representation of the possible recombination pathways, green colour indicates non-radiative recombination, and red is radiative recombination

1.3 Colloidal Nanoparticle Synthesis

Typically colloidal synthesis of nanoparticles involves nucleation and growth of the precursor solution prepared by dissolution of suitable reagents. In nucleation stage, small clusters of atoms are constantly formed and dissolved until sufficient change in the free energy is achieved to surpass the energy barrier for stable nuclei formation. This energy barrier can be reduced by either increasing the precursor concentration or temperature and reduces to promote a accelerated nucleation. Nuclei can now provide available surface sites for free atoms in the solution to attach to, leading to nanocrystal growth. [34]

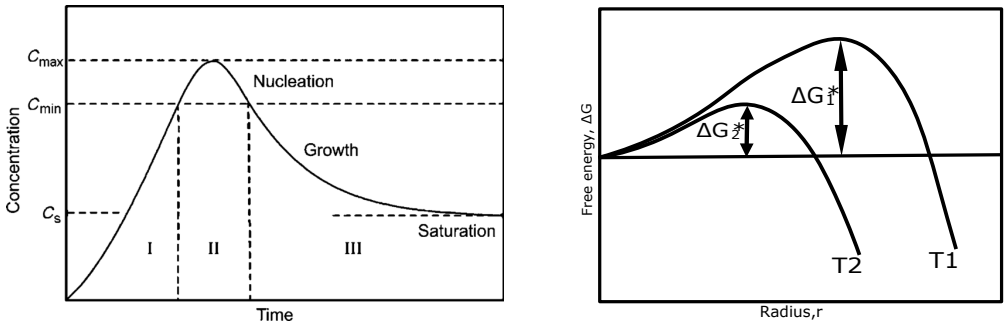

(a) (b)

Figure 1.3: a) LaMer's diagram of Nucleation and Growth, here concentration represents precursor concentration. I) Increasing saturation from unsaturated to critically saturation ($C > C_{min}$ for stable nuclei formation, II)Rapid nucleation occurs, III) Particle growth by diffusion driven process, b) Total Gibbs free energy for nucleation at different temperatures or supersaturation. The critical Gibbs free energy decreases with increasing temperature, T2>T1, same for increasing supersaturation S2>S1

One of the fundamental concepts in colloidal nanoparticle synthesis is supersaturation. Supersaturation describes the concentration of a solution being greater than its equilibrium concentration. There are three stages in a colloidal nanoparticle synthesis proposed by Lamer as seen in figure 1.3a, firstly supersaturation, followed by nucleation and lastly growth. As discussed, stable nuclei are need for nanoparticle formation, which means the system must surpass C_{min}, critical supersaturation level in figure 1.3a for nucleation. From classical nucleation theory, nucleation occurs when the system has reached a maximum in the Gibbs free energy, which is dependent on temperature and supersaturation. From figure 1.3b, it can be seen that how increasing the temperature or supersaturation reduces the required free energy, leading to faster nucleation.[35]

The particle size and the size distribution are closely related to the control over nucleation and the subsequent growth, for example minimising the nucleation time leads to increasing uniformity in the product particle size distribution.

As synthesised nanoparticles tends to aggregate with nearby particles to minimise their surface energy, leading to precipitation of large crystals. This is commonly prevented with surface organic ligands, such the particles are forming a stable suspension in the solvent due to steric hindrance imposed by the ligands. [36]

Challenges with Nanoparticle Synthesis

Colloidal synthesis is considered to be the most economical and efficient approach to obtain large quantities of high-quality nanoparticles. However, it can be challenging to obtain batch-to-batch consistency with traditional flask reactors especially when reactions are carried out manually. In a laboratory setting, minor changes in time, heating and precursor addition rate for example can have strong impacts on the final product, which leads to significant product variation from one batch to another. This undesired product inconsistency between batches is a severe obstacle that prevents being applied in an industrial setting.

This issue is further exacerbated when scaling up the synthesis from lab-scale to industrial scale. The scale up process is usually carried out by increasing the reactor volume, which can be problematic for temperature sensitive synthesis. In laboratory scale synthesis, the temperature gradient in the fluid is homogenised by rigorous stirring, to ensure a uniform temperature and precursor distribution in the solution. However, in industrial synthesis, the fraction of solution volume in contact with the heat source is significantly reduced.[37] This leads to local variations in temperature within the reactor and is unfavourable for nanocrystal synthesis that are highly sensitive to the temperature. Additionally, large reactors tend to have lower stirring efficiency compared to lab-scale stirring, which can cause local concentration variations that also impact the product quality.[38] Therefore, there is an urgent need for production methods that can produce nanocrystals quantitatively with high reproducibility.

1.4 Flow Chemistry

Flow chemistry is a branch of synthetic chemistry where reactions are carried out by flowing reagents through narrow channels. To conduct synthesis ”in flow” is different from using standard laboratory glassware, the obvious part is the confined dimensionality of the reaction channels that are typically on the millimetre-scale. In flow synthesis, the synthesis process is a continuous process, where the reactions occur as the reactive mixture is pumped though the reactor channel. Typically, the reaction starts at a well-defined point in the flow network, where the individual reagents are brought together via a mixer and proceeds further in the flow network at a user-defined flow rate. The product is then collected in a continuous fashion from the reactor as it exits the reaction channel, which differs from batch synthesis where the products are collected at once after reaching the set reaction time.[39]

In conventional batch synthesis, the heat source is applied around the flask, and heats up the mixture, such that only a fraction of the flask is in direct contact

with the heat source, leading to a temperature gradient that must be homogenised by rigorous stirring. For a batch synthesis with volume 25 ml, the surface area-volume ratio is on the order of 100 m^2/m^{-3}. Increasing the volume to 2 L this ratio is drops to 25 m^2/m^{-3}. This large decrease in the surface-volume ratio causes inefficient heat transfer and leads to local temperature variations in the mixture as one scales up the reactor.

In contrast, flow chemistry utilises reaction channels with a typical diameter of 80-1000 micrometers, with a surface area-volume ration of 50000 m^2/m^{-3} to 4000 m^2/m^{-3}. This means the flow reactor can provide the sought improvement in heating efficiency and uniformity. In addition, with the reduced cross section dimension in the channel, diffusive mixing comparatively faster to a flask.[40, 41] These benefits enable user to gain precision control over the reaction conditions leading material synthesis with highly reproducible quality. Throughout this thesis, 1 mm inner diameter tubing has been used, which corresponds to a surface area-volume ratio of 4000 m^2/m^{-3}.

Adapting to Flow Chemistry

Flow chemistry is a developing field at its early stage. Batch syntheses are constantly being adapted to flow with the aim to utilise aforementioned advantages to improve reaction conditions. When synthesising in flow, it is common to separate the reagents to individual solutions that are combined in a mixer and then proceeds to a reaction channel. This allows for precise control over the reaction time, stoichiometry and reaction environment, leading to increasing consistency in the products.[42]

There are commonly three types of flow pattern associated with flow chemistry as seen figure 1.4: 1) continuous flow, 2) segmented flow and 3) droplet flow. In continuous flow, the reagents are injected to the reactor channel as a single continuous phase, hence continuous flow. This is the simplest implementation of flow chemistry, with ability to easily add additional reagents during the synthesis. A major drawback of this type of flow is existence of a parabolic flow profile caused by frictional force at interface with the channel wall. This causes an unwanted variation in reaction time in the reactor, as the fluid in the middle has a faster flow rate compared to fluid that is in contact with the wall. In addition, continuous flow reactions are more susceptible to fouling, especially for nanomaterial synthesis, as the product might preferentially wet the channel to minimise their surface energy. Prolonged usage in continuous flow tends to cause product precipitation on the channel and leads to undesired reactor fouling. [43]

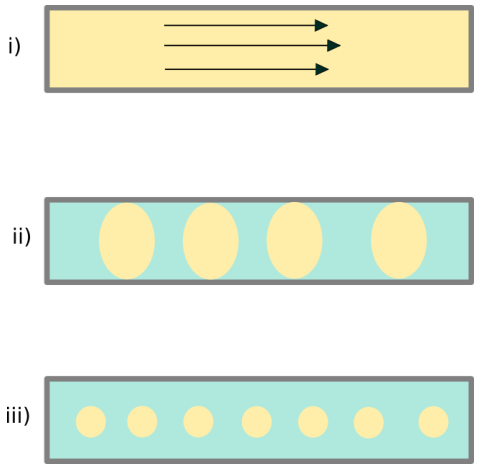

Figure 1.4: Types of flow: i) Single phase flow of the reagents, channel contact leads to a parabolic flow profile; ii) two-phase segmented flow, the reaction mixture is divided by an immiscible fluid; and iii) droplet flow where the reaction mixture is isolated from the channel walls by the immiscible fluid.

One way to overcome the parabolic flow profile is implementing a segmented flow by injecting an immiscible non-reactive fluid alongside the reagents to create an alternating segment of each fluid, in which fluid in each segment experiences the same residence time in the reactor. Reactor fouling can also be minimised by employing droplet flow. Droplet flow is established by choosing carrier fluids that preferentially wet the reactor and can therefore encapsulate the reagent phase in the stream to prevent fouling. For synthesis chemistry, droplet flow is commonly employed to prolong the reactor lifetime and ensure consistent product formation.

Reactor Choice

Despite its many advantages, flow chemistry is yet to be implemented in every synthetic laboratory. There are certain considerations to take into account before adapting a synthesis to flow. If the synthesis proceeds efficiently and quantitatively in batch with good product uniformity, then adapting to flow would not bring significant benefits. Moreover, some syntheses are not suitable for adapting to flow synthesis, e.g., those that involve slurries or lead to excessive back pressures that blocks reactor. Therefore, these questions must be addressed before adapting a synthesis to flow.

If one decides to carry on with flow chemistry for a synthesis, the first consideration is the design of the flow reactor. Flow reactors are broadly categorised into two types: tube- and chip-based reactors. Tube based reactors are generally simpler in construction and use simple fluidic components joined

by appropriate tubing made from polymer or metal, which is the choice in this work. Chip reactors are fabricated from a suitable substrate, such as glass, silicon or selected polymers, using lithography techniques, etching or micromachining. This allows for precise engineering of reaction tailored features integrated into a single small foot-print device. However, the throughput is often limited with these small sized devices and considerable efforts are need to pattern the exact design. One can of course purchase commercially available flow reactors specific to your reaction, however they are often fixed to the order specifications and lack versatility. This can be limiting when discovers unexpected behaviour when adapting a synthesis to flow and reactor modifications must be made.[44]

1.5 Automation and Optimisation

A major advantage of constructing a flow reactor from scratch is ability to automate individual components. By doing so, one gains control over the flow reactors without needing. to manually handling the reactor set-up, which further increases the reproducibility. Additionally, one can translate the synthesis procedure into a set of commands for computer to execute on each component that will be executed in the same manner every time. Thus, one achieves an automated synthesis procedure. However, it is still necessary to carry out product analysis manually to optimise reaction conditions. [45]

Incorporating a real-time on-line analysis module in the reactor set up gives the user the ability to analysis the product properties as synthesised, and avoid inconvenient manual analysis with time delay, which increases the work efficiency and avoids potential human errors that comes with manual processes. An important aspect of incorporating on-line analysis is the possibility of real-time data feedback to the PC, which enables user to change the reaction conditions either manually or using an algorithm to optimise the desired product properties.

Self-Optimisation

The majority of problems in nanocrystal synthesis involve optimising certain product properties. For fluorescent nanocrystals, these properties are often associated with the emission properties of the nanocrystals. For other types of nanoparticles, such as magnetic nanoparticles or dendrimers, particle size and size distribution are more crucial to optimise for their applications. There are often several competing properties during a quantum dots optimisation, for example maximising the intensity of the quantum dot while tuning to a target wavelength or reducing the linewidth. To achieve an acceptable trade-off in such optimisation

manually in batch requires comprehensive understanding of the synthesis and considerable effort.[46]

The increased control of reaction conditions makes the automated synthesis platform ideal for performing synthesis optimisations. The platform which incorporates on-line analysis coupled with typically small precursor consumption allows a large number of reaction conditions to be tested in an efficient manner. A chemical synthesis can be viewed as a black-box optimisation, where the underlying relation between the inputs ('the reaction conditions') and the output properties are unknown to the user. This can be viewed as optimisation of an unknown function that may possibility have multiple optima, which can only be found by evaluating the function at different points in the parameter space. This comes at a cost of materials and time required to evaluate the parameter space. Therefore, self-optimisation of nanocrystals syntheses needs to balance the convergence to an optimum with as few evaluations as possible in the parameter space against the need to avoid getting stuck in any sub-optimal local optimum.[45] A flow chart of the optimisation is shown in figure 1.5.

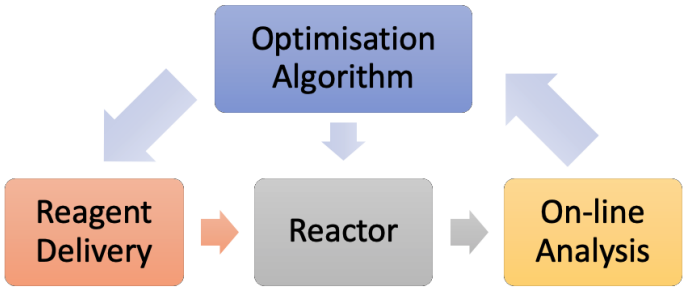

Figure 1.5: A simple flow chart of an automated flow reactor for self-optimisation, showing reagent delivery to a reactor, followed by on-line analysis of the product. The analysed product information is fed into an optimisation algorithm, in our case SNOBFit. The algorithm will recommend subsequent reaction conditions to perform based on the analysed data, which creates a feedback-loop by interfacing the platform with a PC.

In this work, the of global optimisation routine, Stable Noise Optimisation by Branch and Fit (SNOBFit), developed by Huer and Numaier is used to perform self-optimisation with competing objectives. This algorithm balances the evaluation of points around known minima by performing local fits, while carrying out global searches in unexplored areas in the parameter space for other minima that may also exist. The custom-written wrapper around the original SNOBFit algorithm by the Walker *et al.* was used here to perform the unconstrained chemical synthesis optimisation routine. It should be noted that

SNOBFit also allows for constrained optimisations, such one can optimise an objective while holding other objectives within a target value range.

Two interesting objectives for unconstrained optimisation of $CuInS_2$ nanocrystals in this work are to maximise the emission intensity and to control peak wavelength. The maximisation of emission intensity is desirable for applications needing efficient emission for detection purposes, while control the peak wavelength are important if one wants to control the emission colour. For unconstrained intensity optimisation, the algorithm seeks the global minimum of the objective function which is linearly scaled to the intensity value. The objective function used here was formulated as a linear function that decreases with increasing intensity:

$$f = 355 - I_{peak} \tag{1.2}$$

Here I_{peak} is the peak intensity value of the measured emission spectrum, 355 is an inspirational large scalar to make sure that merit value f will always be larger than zero. It is necessary to include this inspirational value as SNOBFit aims to minimise towards zero rather absolute negative. For unconstrained wavelength optimisation, we wish to find the reaction conditions for a target wavelength and the objective function is given as a parabolic function with the target wavelength at zero as seen:

$$f = (W_c - W_{Target})^2 \tag{1.3}$$

Here W_c is the peak wavelength measured extracted from the measured emission spectrum, and W_{Target} is the user defined target wavelength.

1.6 Summary

In this chapter, I have briefly discussed some fundamental concepts related to nanocrystals, including their properties, synthesis and challenges associated with obtaining reproducible nanocrystals. Flow chemistry as an emerging branch of synthetic chemistry with high levels of reaction control is a promising alternative approach to the tradition batch synthesis. The benefits of self-constructed flow reactors were discussed, where one can easily modify the reactor construction and realise automation by interfacing the reactor with a PC. Furthermore, the use of automated reactors coupled with real-time on-line analysis allows users to perform black-box chemical optimisation with global minimum optimisations algorithm such as SNOBFit. Thus, one can perform multi-dimensional unconstrained and constrained optimisations with different objectives. This work aims to develop a tube-based modular synthesis platform for automated self-optimising synthesis.

CHAPTER 2

HARDWARE DEVELOPMENT AND FLOW ADAPTATION

This chapter contains details of the methods and materials used to develop the automated flow synthesis platform and how a flask based procedure for $CuInS_2$ nanocrystal synthesis from literature has been adapted to flow.

2.1 Construction of Automated Flow Synthesis Platform

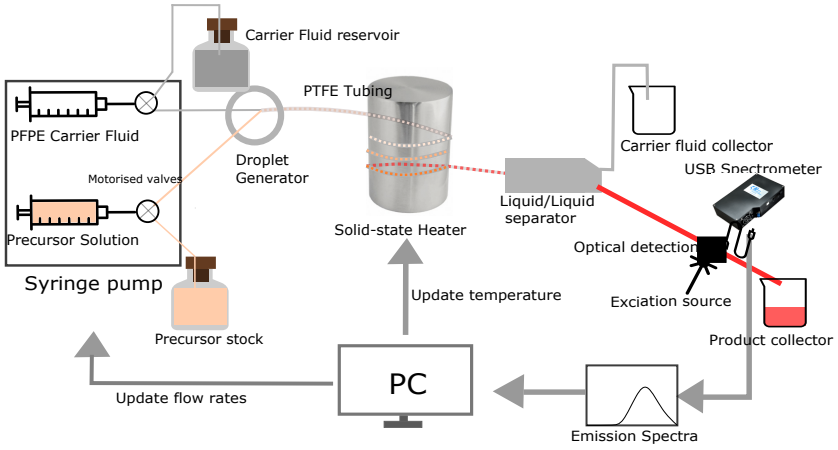

Figure 2.1: Schematic representation of the automated flow platform for a two-phase nanocrystal synthesis.

In construction of this platform, two main components were designed and built in this work: a solid-state heater to control the temperature of the reaction channel, and an optical detection flow cell to record the emission spectra of the produced nanocrystals. Motorised valves for refilling and a liquid-liquid separator used in this work were designed and built by Dr. Andrew Harvie and Prof. John de Mello. PTFE tubing (I.D. 1 mm, O.D. 2 mm) was used for the reactor and transparent

FEP tubing (I.D. 1 mm, O.D. 2 mm) was used for optical detection. A schematic representation of the complete reactor is shown in figure 2.1 .

2.1.1 Development of the Solid-State Heater

A reliable method for heating the reaction channel was required to ensure the reproducible results from the flow reactor. Oil-baths are commonly used in synthesis labs to heat reactions because of their versatility. However, nanocrystal synthesis often takes place at high temperatures above 180°C, where typical oil-bath oils start to degrade. From a practical perspective oil-baths are cumbersome and inconvenient to use. As an alternative I designed a solid-state heater, in which the tubing was wrapped around the heater to achieve consistent heating and hold the reaction channel in place.

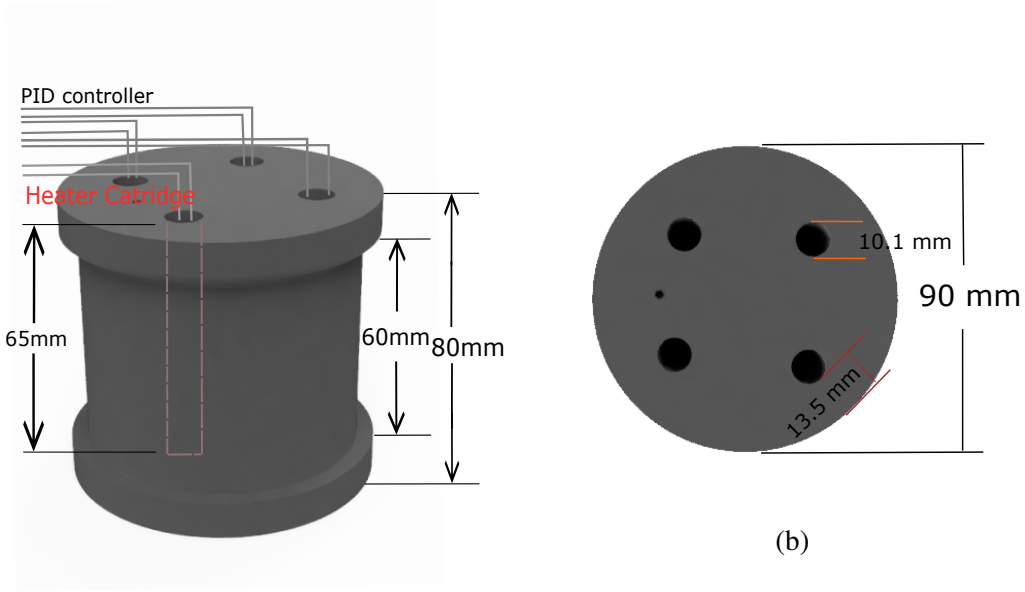

Figure 2.2: Diagrams of the solid-state heater from different perspective. The heater is made of aluminium, with four machined holes for inserting cartridge heating elements.

The body of this solid-state heater was formed from a block of aluminium and machined to have a cylindrical shape with 5 mm lip at both ends to allow the reactor tubing to be threaded and held in place on the heater. Four 10.1-mm in diameter hole were drilled at a distance of 26.5 mm from the centre for insertion of cartridge heaters (Acim Jouanin, 230V 250W, Ø10 mm, H 40 mm).

Three Bakelite feet were attached to the bottom via M3 screws. A K-type PTFE thermocouple was attached to the side of the aluminium block to measure the surface temperature. A schematic representation is shown in figure 2.2.

The heating elements were connected to a terminal box that delivered 230V AC. The terminal box included a single-phase solid-state relay to deliver AC to the heating element, a 12V AC-DC converter that supplies the DC current to a cooling fan and a thermocouple module amplifier chip (MAX31855, Maxim Integrated), to which the thermocouple was connected. The terminal box was controlled by a Teensy 3.2 microcontroller, with a PID control script, using the Arduino PID library (`https://playground.arduino.cc/Code/PIDLibrary`). The code written by Dr. Andrew Harvie (Appendix A) allowed the user to send serial commands from the computer to read the current temperature of the heater, control the set-point, and switch the heater on and off. The heater was in a default off-state with set temperature of 0 °C when connected to a power supply and PC for safety purposes.

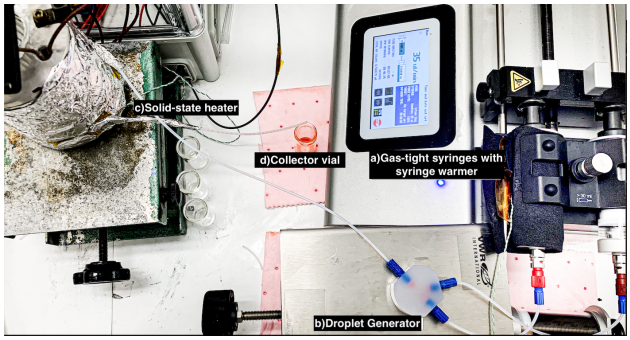

Figure 2.3: Previous set-up from the preliminary project. Here, the cooling is loosely attached above the heater with varying positions during operation.

During the preliminary project, the heater was placed in open air with a PC fan placed loosely above the heater as depicted below in figure 2.3. This configuration was sub-optimal for two reasons. Firstly, the system took. approximate 10 minutes to stabilise to the desired temperature when cooling and exhibited large temperature fluctuations up to 2°C due to the loose placement of the fan. Fast stabilisation is important for achieving rapid changes of reaction parameters. Having the heater open increases the wait time (approximately 5 minutes) to the set-point due to the unreliable air flow from the fan, reduced the efficiency of the reactor. Secondly, 2 °C temperature fluctuation resulted in poor reproducibility, which is one of the intended advantages of having a flow synthetic platform. Moreover, working with poorly secured heat source at high temperatures (170-220 °C) leads to increasing risk factors for the operator and should be avoided.

To overcome the aforementioned disadvantages and potential risks, a box was designed and made from PMMA (also known as Perspex) to enclose the heater and hold it in a fixed position. A PC cooling fan on the top of the box accelerated the cooling process and avoids melting of the box. The enclosure for the heater was 175 mm in height with openings on the body and bottom allowed for good air flow.

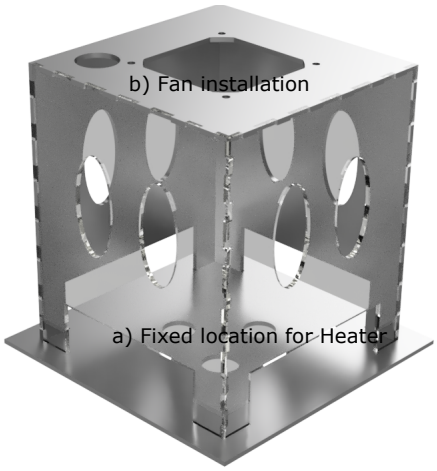

Figure 2.4: Diagram of the designed enclosure for the heater, with securing for the PC fan at the top.

Using four heating elements provided up to 1000 W of electrical heating power and ensured the heater could heat up rapidly. However, the goal was to heat up the both rapidly and precisely to the set-point. This required a systematic tuning of the PID parameters coupled with the cooling fan. The fan was enabled when the current temperature was 10 °C below the set-point during heating. It was kept on constantly when the temperature had stabilised or cooling down to a lower set-point. The behaviour of a PID control system can be changed by the three parameters: proportionality (P), integration (I) and derivative (D) constants. These were systematically tuned by starting with a high proportional constant (200), while the other constants were set to 2. The integral constant was then increased until the overshoot behaviour from set-point was reduced to an acceptable level, and lastly the derivative constant was increased to minimise any steady-state oscillations. The resulting optimised PID parameters were P=200, I=15 and D=5, which gave a heating rate of 1 °C/s and required approximately 80 seconds from overshoot state to stabilise to the set-point. The steady-state oscillations from the set-point is found to be 0.3 °C, close to the 0.25 °C thermocouple module resolution. Figure 2.5 shows the temperature ramp after PID tuning.

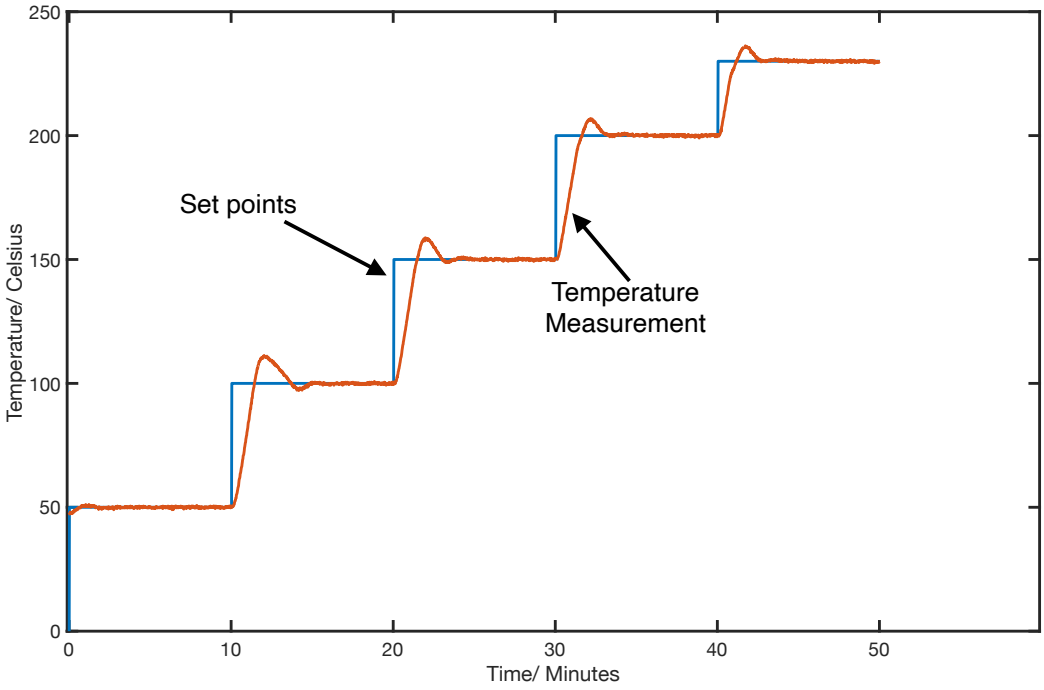

Figure 2.5: Temperature ramp of the PID tuned heating system, here the temperature is increases in 50 °C increments and held constant for 10 minutes until next target temperature.

From figure 2.5 it is evident that the self-built solid-state heater provides a stable precise temperature that could be both increased and decreased relatively quickly, providing good control over the reaction temperature in the automated platform.

2.1.2 Optical Detection Flow Cell

A crucial component to realise automation and optimisation is the on-line real-time analysis system. This makes it possible to analyse product properties in real-time as the reaction mixture exits the reaction channel. In this work, fluorescent nanocrystals were produced by the flow reactor, and therefore, it was desired to investigate the emission features from the produced nanocrystals in real time. This was realised by using an optical flow cell, where the tube, excitation source and spectrometer were orthogonal to each other. The flow cell works by exciting the fluorescent nanocrystals with an excitation source, and using a spectrometer to record the emission spectrum due to nanocrystals. In this work, the designed flow cell modules were printed by a hobby 3D printer (Anycubic Mega i3) and material

used was black coloured polylactic acid (PLA).

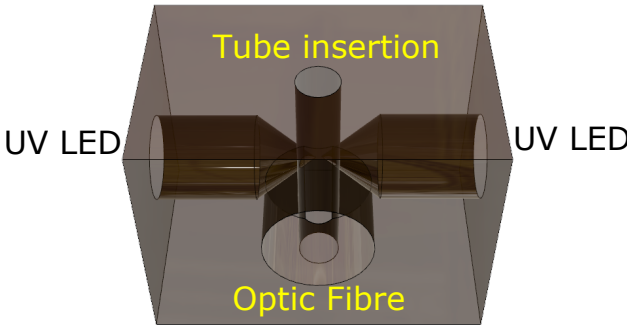

Figure 2.6: Designed UV-LED based flow cell, here two UV-LEDs are inserted orthogonal to the FEP tube, and Optic fibre is inserted to transfer the emitted photons to the spectrometer.

In the first design iteration, commercially available UV-LEDs (25 mW, 385 nm excitation wavelength) were used as the excitation source, an Ø600 um optic fibre was used to transfer the emitted light to a USB spectrometer (Ocean Optics USB 4000). The designed flow cell for this UV-LED configuration is shown in figure 2.6 and fits with standard 5 mm LED packaging. Transparent FEP tubing with the same dimension as reactor channel (I.D. 1 mm, O.D. 2 mm) was used to in the optical flow cell to maximise optical accessibility.

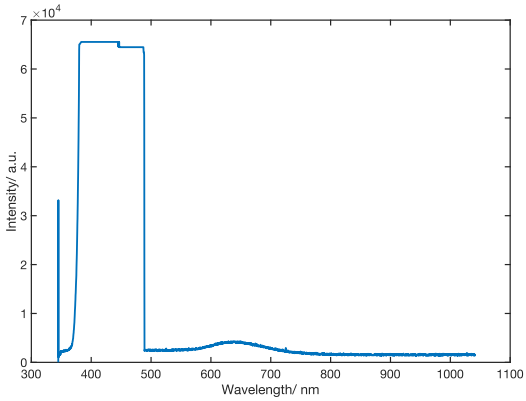

Figure 2.7: Full core $CuInS_2$ spectrum recorded with Ocean Optics USB 4000, with 1 minute integration time and 2x 385 nm (25 mW) UV-LED as excitation source. Here the broad saturation region between 385 to 490 nm is due to the LED emission tail, and Quantum dot emission feature is found between 490 to 850 nm.

In order to record meaningful emission signals from the QDs, the integration time for the USB4000 spectrometer had to be set to at least 1 minute. A detailed discussion about spectrometer integration time is found in the following section in spectrometer configuration. Figure 2.7 shows a full spectrum obtained using this optical flow cell with freshly produced core $CuInS_2$ nanocrystals. Here we can see the emission features around 650 nm from the nanocrystals and a saturated region from 385 to 490 nm due to the tail from LED emission.

Figure 2.8 below shows a ”zoomed in” region from 495 nm to 900 nm, where we can see the emission peak around 650 nm and a typical Gaussian-like emission spectrum to the right of the peak. However, on the left side we observe the emission intensity level is increased, which is caused by the emission tail from the LED and results in compromised spectral data. Excitation light is often blocked by installing a long pass filter in front of the fibre optic, but since the led tail overlaps the quantum dots emission wavelength, a long pass filter would not help here. Therefore, we are motivated to find a method to eliminate the undesired LED-tail.

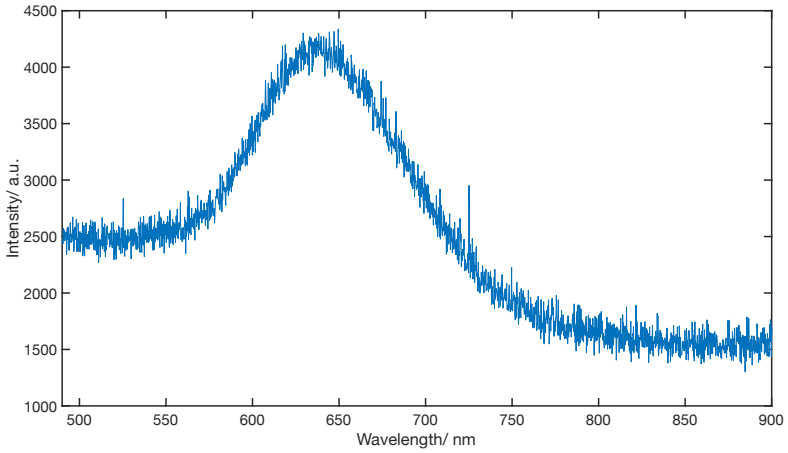

Figure 2.8: ”Zoomed in” core $CuInS_2$ emission spectrum recorded with Ocean Optics USB 4000 with 1 minute integration time and two 385 nm (25 mW) UV-LEDs as excitation source. The quantum dot emission peak is found around 650 nm, and the emission spectrum is contaminated by substantial noise

In this design, the implementation of dual UV-LEDs with low (25mW) effect led to the products were not efficiently excited (with majority of the product in the tube remain unexcited), and therefore requires long integration time on the USB4000 spectrometer. Long integration time is not favoured for practical reasons as it causes more noise and requires substantial spectral averaging to obtain low noise spectra, which further increases the measurement time. From these observations, it was decided that the most appropriate way to improve the

spectral data quality and time efficiency was to substitute the UV-LED with a more intense and narrower excitation source with minimum tail, preventing spectral overlap between the light source and QD emission and reduce the measurement time.

Traditionally, a bench-top spectrometer uses a Xeon lamp as excitation source with monochromator to get desired excitation wavelength, but it can also be achieved by using a laser. Thus, a diode-pumped solid-state laser with 355 nm wavelength (NanoUV 355, JDS Uniphase) was used in this project as an excitation source. A new flow cell was designed to attach to the front of the laser, with optic fibre insertion made available on the top of the flow cell to couple collected light to the spectrometer. The new design is shown below in figure 2.9a together with the technical drawing of the laser in figure 2.9b

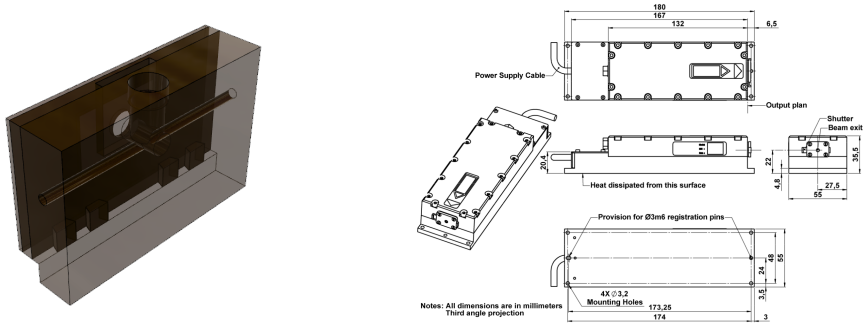

(a) (b)

Figure 2.9: a) New flow cell that can be attached to the front of laser, the tubing is inserted horizontally and optic fibre on top. b) Technical drawing of the laser from manufacturers data sheet.

The change of excitation source eliminated the spectral overlap and reduced the noise level by shortening the required integration time for a quality spectrum as seen in figure 2.10. Here a 3 seconds integration time was sufficient for the USB4000 to record clean emission spectra from the product. The 20-fold reduction in integration time allowed the user to perform 20 averages within a minute, thus increasing the signal to noise ratio.

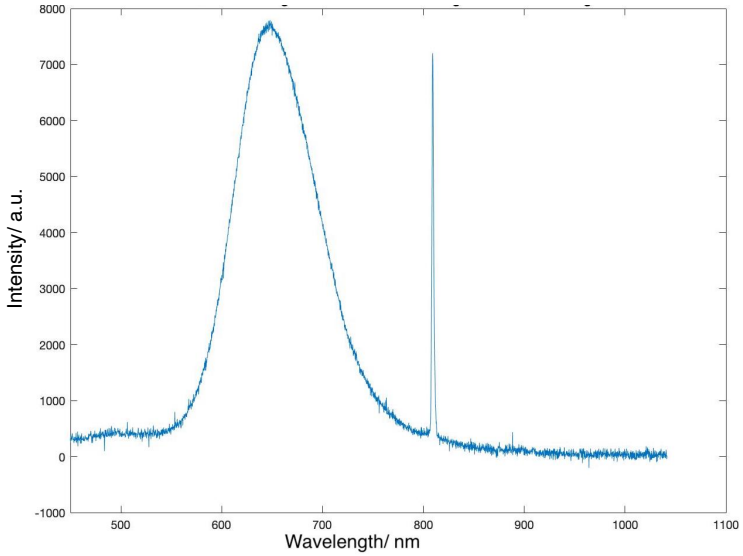

Figure 2.10: Spectrum of the same product as figure 2.8 with 3 seconds integration time and 20 averages, taking a total of 1 minute was taken to perform the complete acquisition. The peak at 800 nm is the second harmonic peak of the laser, which always occurs in the same wavelength range and may be cropped out when analysing the data.

Incorporating Intensity Monitor

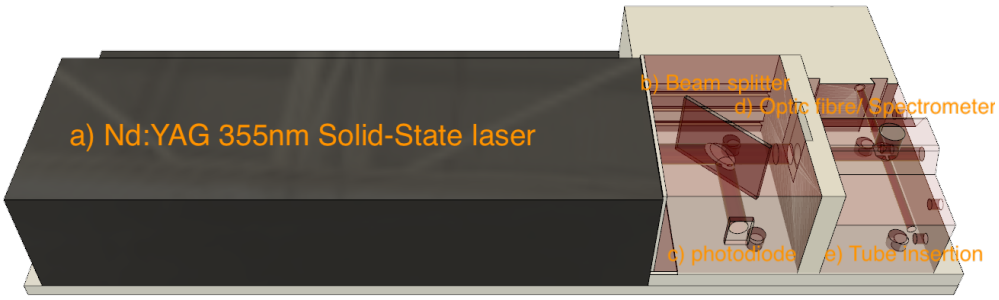

Figure 2.11: Diagram of the optical detection system. a) Solid-state laser, b) Beam splitter, c)OPT101 Photodiode d) Optic fibre insertion or direct insertion with Ocean Optics USB4000, e) FEP tube insertion.

The laser used in this project is more than 10 years old, and consequently the beam intensity can was found to vary during operation. This leads to varying intensity in the emission measurement due to the beam intensity variation. Therefore, a correction of the spectral data based on the laser intensity value was required. A beam splitter was placed in the laser beam to direct part of the laser beam towards a photodiode that monitored the intensity. The intensity monitor module in the work was printed from black PLA by 3D printing and is indicated by label b) and c) in figure 2.11. A glass microscope slide is positioned 45 degrees to the incoming laser beam and the photodiode, this leads to around 4% of the light being directed to the photodiode while rest 96% is directed towards the flow cell. A diagram of the new optical detection system is shown in figure 2.11, a baseplate and side support were printed to secure the module in place. A modification of the flow cell was made to accommodate the USB4000 spectrometer directly, this aims to remove the signal loss by using an optic fibre and reduce the cost from buying high end spectrometer. In this project, an Ocean Optics QE65000 spectrometer was chosen for analysis due to its high resolution and sensitivity that provided better time-efficiency in the acquisition procedure.

The photodetector used in this work was a OPT101 amplified photodiode which was secured to the beam splitter module by hot glue and connected to a Teensy 3.2 microcontroller to convert the analogue output voltage to digital signal. The digital data was filtered by a time exponential filter with time constant τ = 10 seconds, and a smoothing factor α = 0.0001, with 1 millisecond delay in the readout. This filtered data was then averaged 250 times to provide a stable readout. It was observed that 4% of the laser beam was able to saturate the photodiode readout, therefore it was necessary to reduce the laser signal to get meaningful readout values.

In the first approach, an 0.3 Optical Density (OD) plastic filter was placed in front of the photodiode and reduces around 50% of the incoming beam intensity, thus approximate half of the intensity is measured by photodiode. It is observed around 7% intensity variation in the laser beam in recorded by using this configuration as seen in figure 2.12, which is unexpectedly high for a solid-state laser. From experience we expected around 1% variation maximum and stable beam intensity.

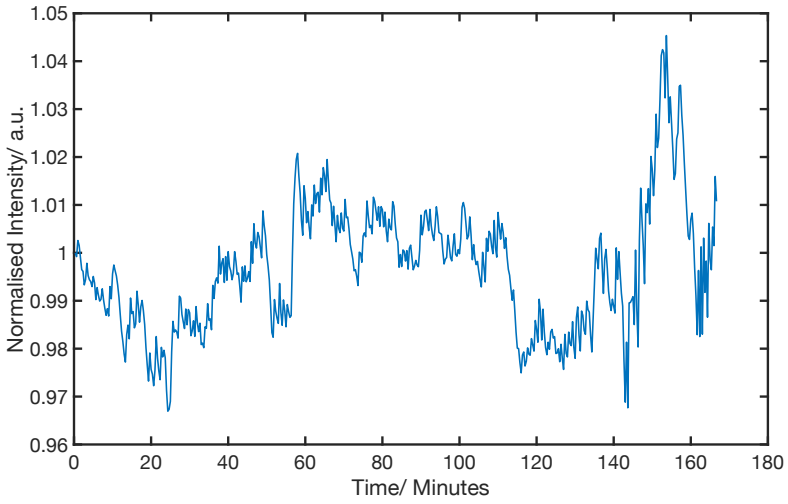

Figure 2.12: Recording of the laser beam intensity by photodiode with 0.3 OD filter. The largest variation is observed to be around 7%, and is inconsistent with expectation for a solid-state laser.

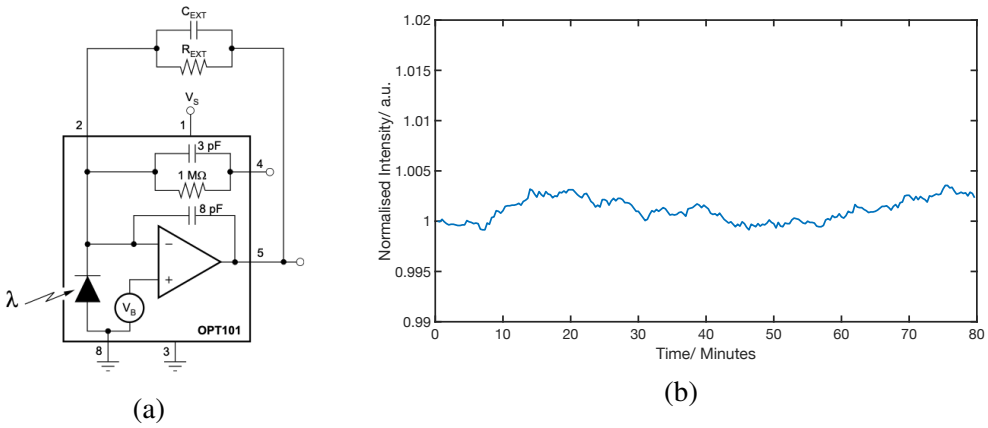

(a) (b)

Figure 2.13: a) Block diagram of OPT101, the external RC circuit is connected between pin 2 and 5 such that it bypasses the internal 1 MΩ gain resistor, b) New laser intensity recording with reduced responsitivity, showing $< 1\%$ intensity variation.

It is suspected that the large fluctuations were partly due to the large internal resistance gain coupled with reduced signal uptake. The gain of the OPT101 amplified photodiode may be reduced by connecting an external RC circuit in specific pins, as shown in figure 2.13a. An 0.1 MΩ external resistance and 33 pF external capacity were used to reduce the DC gain from 10^6 V/A to 10^5 V/A. This configuration (with the OD filter removed) gave a the laser beam

intensity variation within 1% range as seen in figure 2.13b and was consistent with expectation. Therefore, this configuration was used for the rest of this work.

2.1.3 Spectrometer Configuration

In this work, compact USB spectrometers with different grades were used during development to test the system and analyse the product features during automated synthesis. This type of spectrometers are designed to be compact and portable, with low power consumption, so that a 5V supply from a USB port is sufficient to power them. Different from traditional bench-top scanning spectrometers, this class of spectrometer uses a charge-coupled device (CCD) as a detector rather a photomultiplier tube. Photomultiplier tube detectors are large devices that provides high sensitivity, low noise data with high energy consumption and are rather expensive. Scanning optics are also required to measure individual wavelengths in sequence, therefore hard to realise good portability.[47] CCD on the other hand are compact detectors that are more cost efficient and able to measure all the wavelengths simultaneously. In a CCD based spectrometer, CCD can convert incoming photons into an electric charge and is used to measure the amount of photon entered the system at each wavelength. In order to separate the incoming photon into individual wavelengths, a diffraction grating is used within the spectrometer that disperses the incident photon to constituent wavelengths and reflects on to the detector. As photons land on different pixels of a CCD detector, electrons are generated and stored as analogue information. After appropriate recording period, the accumulated charge is transferred from the CCD detector, converted to digital data with the on-board processor and sent to computer for analysis.[48] The output data is shown as a spectrum.

There are several types of noise associated with a CCD spectrometer, the common noises are: 1) dark noise, 2) readout noise and 3) electronic noise.[49] Here, dark noise is caused by thermally generated electron-hole pairs in the detector and is temperature dependent, readout noise is generated from reading a pixel's accumulated charge and electronic is due to the are circuitry of the on-board processing units. These noises make up for a so-called baseline offset and is the main contributor to the fixed pattern noise. Therefore, to reduce those noises, spectral averaging and cooling of the detector is required, a comparison between fixed pattern noise with and without cooling enabled is shown in figure 2.14.

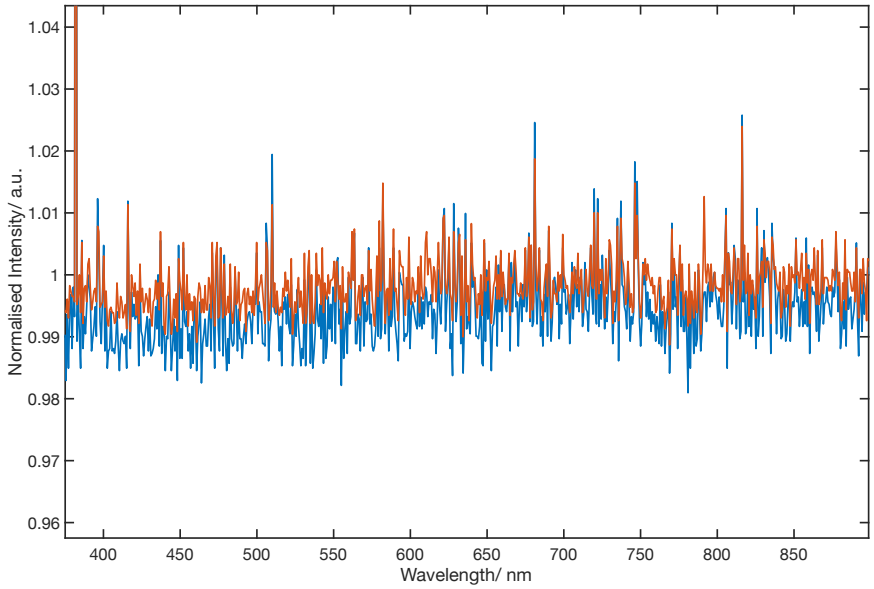

Figure 2.14: Blue) Single dark spectrum with 1 second integration time and thermoelectric disabled, Orange) Single dark spectrum with 1 second integration time and thermoelectric cooling set to -5 °C. Both spectrum were acquired with the QE65000. Here the noise level of cooled spectrum is lower compared to uncooled spectrometer setting.

One can observe the noise level in the orange spectrum with enabled thermoelectric cooling is less noisy compared to the blue spectrum obtained without thermoelectric cooling. It should be noted that not all USB spectrometers have thermoelectric cooling feature, for example the USB4000 spectrometer used during early development lacked this capability. Therefore, QE65000 spectrometer is used in this work with thermoelectric enabled and set to -5 °C. To record a reliable dark spectrum (and baseline offset) for the system with minimal readout and electronic noises, one should take many averages as possible. Figure 2.15 shows a comparison between a 3000 averaged and single dark spectrum.

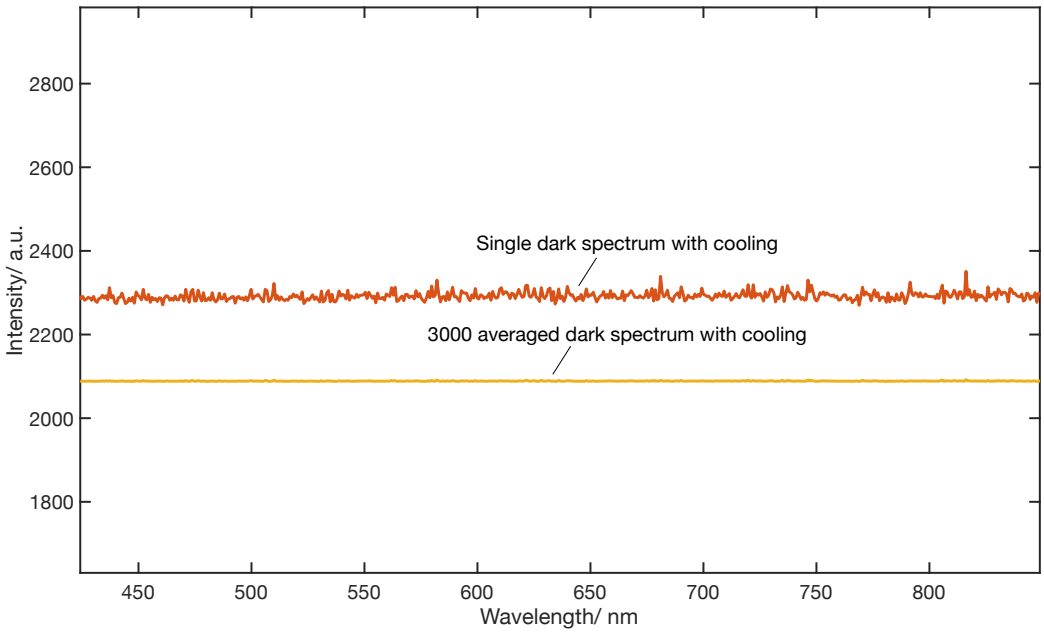

Figure 2.15: Comparison between a single dark spectrum and 3000 times averaged dark spectrum. Both spectrum are acquired with QE65000 with with cooling enabled and 1 second integration time.

The aforementioned photon recoding time before passing the accumulated charge to the A/D converted for processing is termed the *integration time*. The minimum integration time is the shortest time for the CCD to read out all the pixel information and is different from the concept of data transfer speed, which is the speed for spectrometer to transfer the processed data to a PC. Since dark current is a continuous production of electron-hole pairs, a longer integration time results in higher numbers of dark electrons, thus higher dark noise. During the development phase, an Ocean Optics USB4000 spectrometer was used to test various light source and it was observed that the USB4000 yielded noisy data, due to the absence of cooling features and low detector sensitivity. The low sensitivity required longer integration time (around 5 seconds with laser, 5 times more than the QE65000), and generated more dark noise and therefore required more spectral averaging (more than hundred) to obtain quality data with sufficient signal to noise ratio (SNR) for reliable analysis, e.g., 290:1. This added up to more than 5 minutes for one spectral analysis, which is long time when considering one residence time was typically around 3-6 minutes.

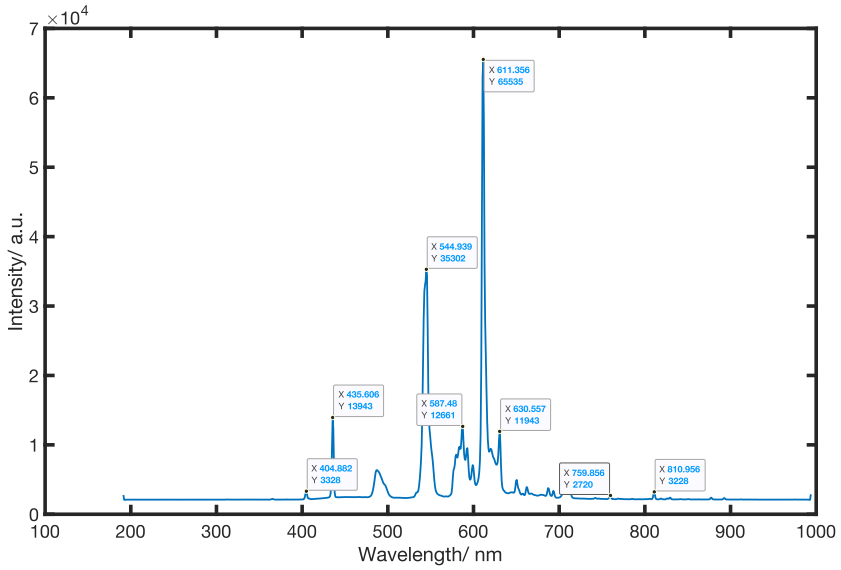

Figure 2.16: QE65000 spectrometer wavelength calibration against the mercury line of a fluorescence lamp, showing the spectrometer wavelength had less than 1 nm deviation.

For this work I therefore used a scientific grade Ocean Optics QE65000 spectrometer with high sensitivity and ability to cool down the detector to maximum -15 °C, as previously mentioned. An optic fibre with Ø600 um was used in this work to transmit the emitted light from optical flow cell to the spectrometer. The spectrometer was wavelength calibrated against the mercury lines of a fluorescence lamp and shows less than 1 nm in deviation, indicating reliable wavelength measurements as seen above in figure 2.16.

A plastic long pass filter with 480 nm cut-on frequency was inserted in the flow cell before installing the optic fibre to attenuate scattered excitation light. The aim was to prolong the spectrometer lifetime and minimise the current leakage to neighbouring detector pixels due to intense laser emission.[50] The % transmission at the laser wavelength was measured to be to be 9% in absorption spectrometer and around 83% from cut-on region. The spectral behaviour of the long pass filter is shown in figure 2.17

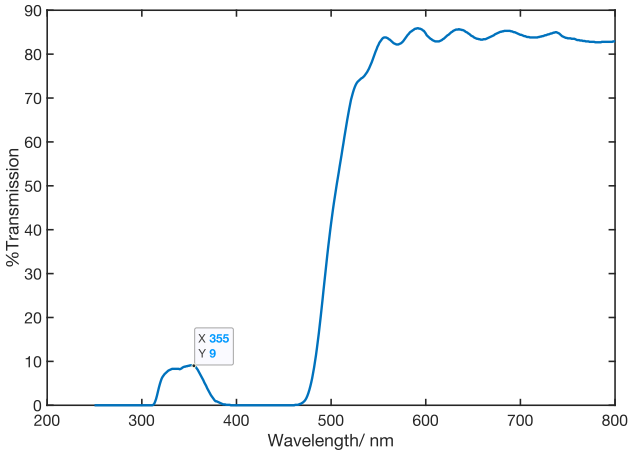

Figure 2.17: Long pass filter with cut-on wavelength at 480 nm. The % transmission at laser wavelength was found to be 9% by using an absorption spectrometer, optical unfiltered region has a transmission rate around 83%.

A side-by-side comparison of the laser beam intensity prior and after installing long pass filter is shown in figure 2.18. The spectrometer was configured to 8 microseconds integration in order to not saturate the detector for this measurement. The result showed a successful reduction in intensity by around 85% at the laser wavelength, close to the expected value determined by absorption spectrometer.

Finally, to avoid ambient light pollution to the photodiode and flow cell, a cover was printed to shield the front half of the optical detection. This is again wrapped in aluminium foil to minimise ambient light pollution.

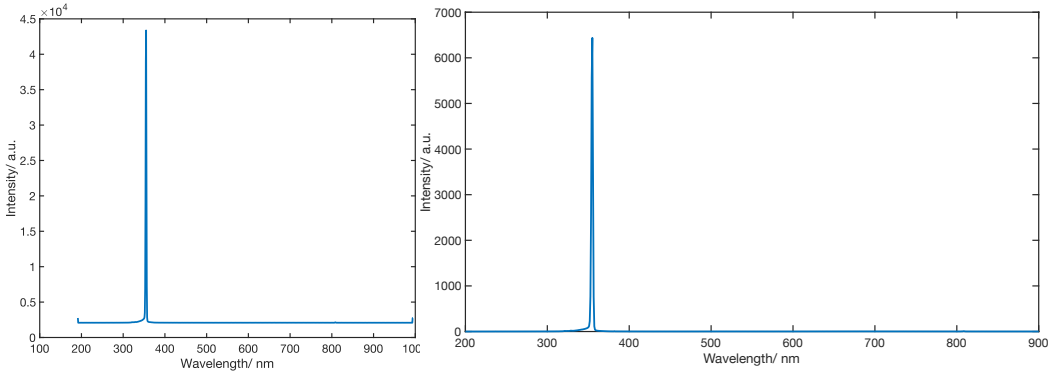

(a) (b)

Figure 2.18: a) Laser beam without long pass filter. b) Laser beam intensity with long pass filter. Spectrometer was configured to 8 microsecond integration time. A 85% reduction in the laser intensity was obtained

The spectrometer configuration used in this work for optical detection of produced nanocrystals was 1 second integration time, thermoelectric cooling enabled and set to -5 C, and continuous averaging until a target signal-to-noise ratio of 290:1 was reached (30 maximum averages). This led to a maximum 40 seconds detection time which overcomes synthesis stalling and increases time efficiency. For $CuInS_2$ nanocrystals produced in this work, low fluorescence situations typically required about 20 averages to reach a signal to noise ratio of 290:1 and moderate to high fluorescence situations could reach this ratio by few averages (usually around 5). An example of a typical spectrum is shown in figure 2.19 with a signal-to-noise ratio of 290:1.

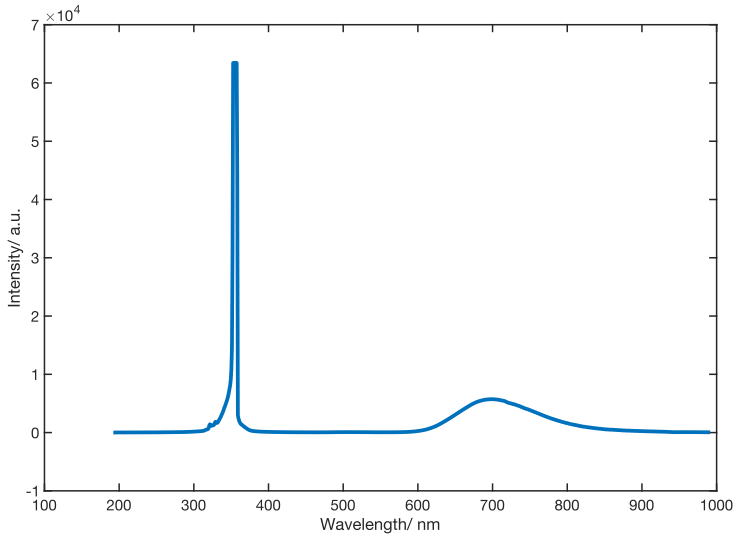

Figure 2.19: A typical $CuInS_2$ emission spectra in this work with signal to noise ratio $>$ 290:1.

From the spectrometer and photodiode data, we can conclude a working optical detection flow cell that is able to provide high quality, low noise, reliable emission data for analysis within short acquisition time. In the current design, the spectrometer detects fluorescence signal emitted from the product, but the design can be changed relatively easy to accommodate other techniques such as absorption analysis.

2.1.4 Automated Liquid Separator

A liquid-liquid separator allows user to separate a two-phase flow in the reactor into continuous phases in two different channels. This process is critical in flow chemistry with applications including: 1) multi-stage synthesis, where it might be

necessary to switch between two-phase and continuous flow to carry out specific steps of a reaction; 2) on-line/inline analysis, where change from two-phase to continuous flow can simplify the sample analysis; and 3) purification, where it is necessary to separate a target material in one of the solvents from the other solvent in the reactor

During the development of the flow cell USB4000 spectrometer was used that required 5 minutes acquisition time. As we are working in a biphasic flow, the flow pattern is alternated between carrier fluid and product, therefore it was not possible to analyse the product reliably. To analyse the product in a biphasic flow required one to pause the flow, and it could not be guaranteed that the product droplet resides at the exact location as laser beam every time and leading to unreliable data. Therefore, an automated liquid-liquid separator developed by Dr. Andrew Harvie was integrated into the platform to separate the product from carrier fluid and enabling long analysis time. An annotated photograph of the automated liquid-liquid separator is shown in figure 2.20.

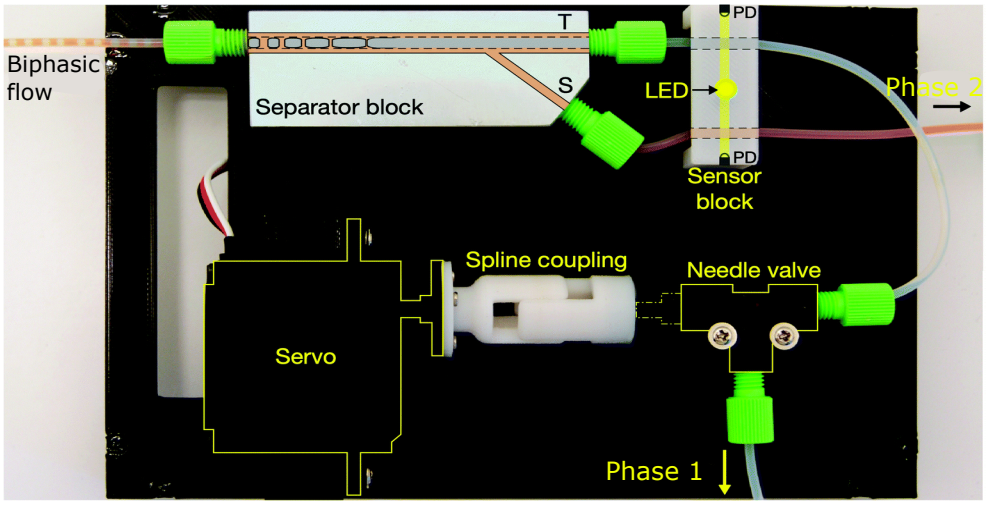

Figure 2.20: Annotated photograph of automated separator comprising a machined aluminium separator block for inducing phase separation, a sensor block containing a LED and two photodetector (PDs) for optically monitoring the two output channels, and a motorised needle valve for controlling the back-pressure at the through (T) channel outlet. This through channel configuration was used in this work for separating PFPE carrier fluid and 1-octadecene solvent. Reproduced with permission from Harvie *et al.*[1]

The working principle of this separator relies on the difference in wettability of the two liquids to the wall of the porous capillary used in the separator block. The liquid with better wetting to the porous capillary will leak through the porous wall

to the cavity, while the other liquid passes unhindered though the interior channel. To achieve flow separation, a flow restriction is required for the under-pressured outlet to establish an appropriate pressure differential between the two outlets. If the pressure is too high in the through channel (the porous capillary), both liquids will be push into the cavity and flow out through side channel. If the pressure is too low, then both liquids will flow straight through the channel without separation. There are many factors involved for the correct pressure setting in the needle valve to create appropriate flow restriction, including the viscosities, densities and interfacial tensions in the liquid combination. In order to achieve automated separation, the needle valve is coupled to a stepper motor to dynamically vary the flow resistance at the under-pressured outlet. The correct valve setting is determined by monitoring the optical transmittance of the fluid streams at both outlets by photodiodes by automatically adjusting the valve position gradually until smooth time-invariant signals were observed at both outlets. This allows user to obtain complete separation without the need for manual intervention.

In case of complete separation, a single continuous phase is flowing uniformly through each channel outlet, and the photodetectors in both ends will generate stable, time-invariant signals. On the other hand, if the separation is imperfect, at least one of the photodetectors will generate a fluctuating signal due to different optical transmission in the liquids. The onboard microcontroller with pre-programmed firmware will adjust the valve position accordingly to the fluctuating signals until the time-invariant signal is re-established.

The automated separator uses a microcontroller with custom written firmware uploaded to the microcontroller for adjusting the motorised valve. Since the flow rate and liquid combination are different for each adaptation process, there are a few parameters in the firmware that can be tuned to fit the current synthesis. These parameters are maximum turning of the servo per iteration, acceptable signal differential range without making an adjustment, sampling time, delay time between two sampling and proportional coefficient that determines the level of adjustment. The parameters used in this work were 6 seconds sampling time, maximum 30 degrees turning per adjustment, acceptable differential was set to 0.004, 7 seconds delay between two sampling time and a proportional coefficient of 2000. These parameters were used to accommodate a flow rate ranging from 200 μl/min to 500 μl/min for Galden HT270 carrier fluid and 1-octadecene (ODE) solvent. After the separator has identified a feasible position for the needle valve in this parameter range, the separator is taken to manual mode by unplug the power supply to prevent accidental rotation from possible data sampling errors.

The choice of carrier fluid here is important for the separator, for this project both Fomblin YL-Vac 16/6 and Galden HT270 were tested for the separator, these carriers are PFPE fluids with different viscosities. PFPE fluid has a very good wettability with the porous capillary tube in the separator block, and therefore is

a good candidate to use as carrier fluid. However, the viscosity is an important factor to consider, if the fluid is too viscus, the force is dominated by frictional force with the tube wall rather interfacial wetting, causing imperfect separation. The synthesis is mainly conducted around 180 °C in this work, and the viscosity of both carrier fluids (2 cTs for Fomblin and around 0.8 cTS for Galden HT270) are quite low in this temperature. However, as the flow exits the reactor towards separator, the fluids within are rapidly cooled by the air from the cooling fan. This leads to a dramatic change in the fluid viscosities, and by the time the fluids reach the separator, the temperature might be around 40 °C or less. In this temperature range, Fomblin has a kinematic viscosity of 60 cTs and Galden has a viscosity of 2 cTs from manufacturer's technical data as seen in figure 2.21. Therefore, it is very hard to coerce the Fomblin carrier fluid through the porous wall when the frictional force is the dominate force. This is consistent with experimental observation, as we were unable to separate the Fomblin/ODE combination with the separator.

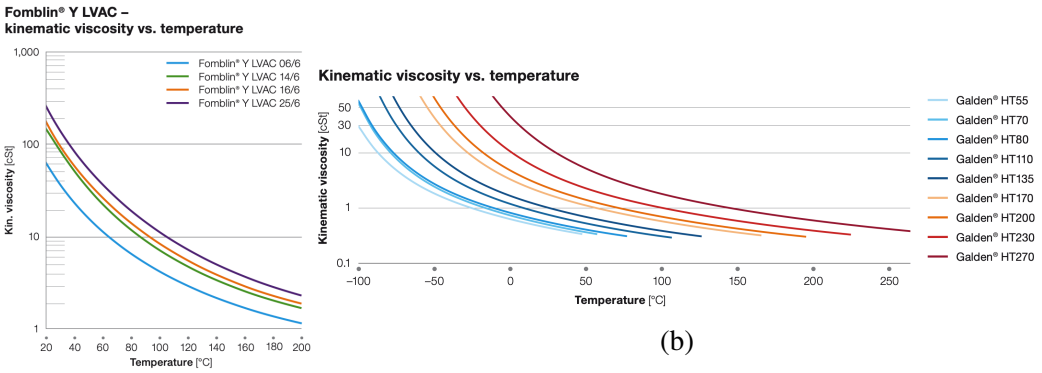

Figure 2.21: a) Kinematic viscosity of Fomblin 16/6 PFPE fluid at different temperatures. The viscosity is 60 cSt at 40 °C. b) Galden HT270 PFPE fluid at different temperatures. The viscosity is around 2 cSt at 40 °C. Data is taken from Solvay product datasheet. For reference, water has a kinematic viscosity around 0.65 cTs at 40 °C, and 1-octadecene has 3.8 cTs at 40 °C.

Since Fomblin was too viscous for the separator, and the viscosity of Galden HT270 was found to be around 2 cTs at the temperature range. It was deviced to switch the carrier fluid to Galden. Which solved more than one problem during the adaptation process to flow which we will discuss later in the adaptation section in this chapter. It was observed the Galden HT270/ODE combination was able to achieve complete separation as seen in figure 2.22.

It should be noted the separator is susceptible to performance drop when

working with nanocrystals in this liquid combination. This was observed during self-optimisation synthesis with continuous working for over 45 hours in manual mode. The separator initially was able to achieve complete separation, but gradually product solution started to leak to the side channel into the collector. This means from time to time; a small fraction of the product ended up in the cavity and into the side channel. For analysis, this is not an important issue, and it was only necessary to increase the wait interval to be able to achieve reliable spectral analysis. However, for other synthesis that involve additional steps and rely on the separator working perfectly, other liquid combination might be required.

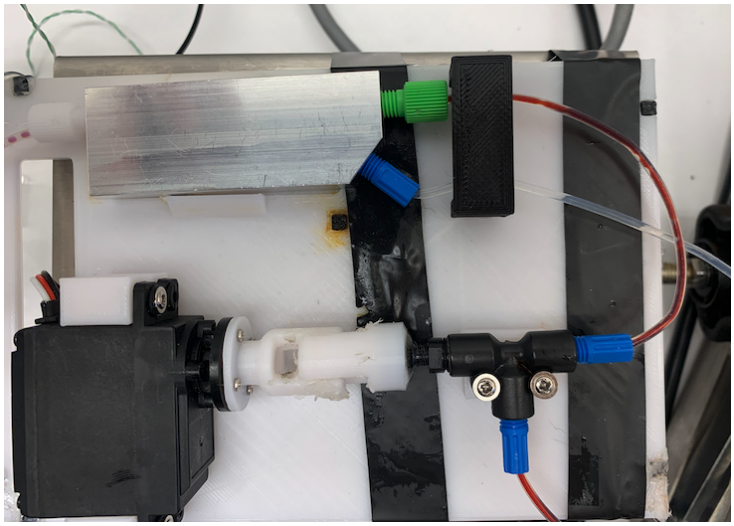

Figure 2.22: Photograph of separator in working condition with Galden HT270/ODE solvent combination at 350 μl/min flor rate. The transparent fluid is Galden HT270 carrier fluid, and the red fluid is synthesised $CuInS_2$ nanocrystals in 1-octadecene solvent.

Incorporating the separator into the system made it easier to obtain reliable spectral analysis, especially for low fluorescence materials that required long acquisition time. In this work, the maximum spectral analysis time was 30 seconds. Here is a video of the liquid separator working in real-time in manual mode: `https://youtu.be/9r2EveYI1Nk`

2.1.5 Delivery System and Refilling Mechanism

One of the fundamental requirements for a working flow reactor is reliable and precise delivery system. There are many systems available in the market, or one can design a custom delivery system that works under specific conditions

depending on the need. In this work, two KD Scientific Legato 210 syringe pumps were used for reagent and carrier fluid delivery. This model is able to perform both infusion and withdraw with high flow rate precision (down to 3 pl/min with 0.5 μl syringe) within 0.35% standard deviation and 99.5% reproducibility, which is ideal for this work that requires frequent changes in the flow rate and high reliability. The syringes used in this work to contain the fluids are Hamilton 1050TLL and 1100TLL gas-tight syringes that were respectively 50 ml and 100 ml in volume with Teflon Luerlocks. One syringe was secured on each pump, this was due to practical reasons such as system flushing and individual refilling process. The linear force level of the syringe pumps was set to 100% due to large syringe dimension, this force level corresponds to 34 Kg according to manufacturer's technical information. A photograph of the syringe pump is shown in figure 2.23 below.

Figure 2.23: KD Scientific Legato 210 dual syringe pump with serial communication (also touch screen) used in this work.

The syringe pumps were connected to a computer via USB and are able to execute received commands from the computer, and provide feedback to the computer after executing the commands. This feature was crucial for the project, since it allowed me to control the delivery system from computer terminal and realise automation. The limiting factor from achieving fully automated synthesis was the limited volume of syringes. The largest commercially available syringe contained 100 ml of liquid, and for this project, this was sufficient for testing around 35 reaction conditions, which is fine for a parameter screening, but far from enough for large optimisation routine with long residence delay between each measurement. Additionally, a filled 100 ml syringe has a centre of gravity in

the front part of the syringe and is not positioned on the syringe pump bed itself. This can in turn cause deviations in the flow rate, as the plunger might have an angle to the driver plate and leads to reducing the sought reproducibility in the product.

As previously mentioned, the Legato 210 model supports withdraw, and I utilised this withdraw function to achieve fully automated operation. This was done by incorporating motorised valves that could rotate between infusion and refill mode . A schematic representation of the motorised valves is shown in figure 2.24a, with a flow chart to explain how the automated refill works in figure 2.24b.

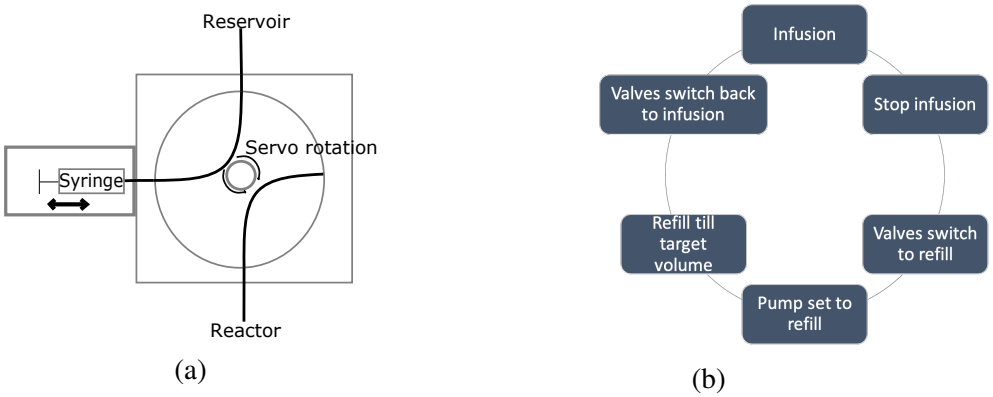

Figure 2.24: a) A schematic representation of the motorised valves, the servo is able to rotate to either infusion or refill (reservoir) upon specific serial commands. b) A flow chart of the refilling process.

The motorised valves were able to change modes upon receiving serial commands from the computer, which caused the servo to rotated to the correct position (and stay inactive when repeating commands of the same position). The withdraw rate was different for carrier fluid and precursor solution due to different viscosities, for Galden HT270 a withdraw rate of 1.5 ml/minute is found to be appropriate with no air bubble intake within the syringe due to possible leakage in the Luerlock connector. For precursor solution, a withdraw rate of 2 ml/minute was sufficient to eliminate air bubble.

By incorporating two motorised valves designed by Prof. John de Mello and Dr. Andrew Harvie, I successfully realised an automated synthesis platform that was able to perform long synthesis operation with varying flow rate and optimisation routine by on-line analysis.

2.1.6 Automation

The heater, optical detection system, syringe pumps with refill and automated separator were controlled by a computer via Universal Serial Bus (USB). For automated operation, MATLAB functions (Appendix B) were written to control each unit and a parent script to call each unit. The parent script accepted a list of temperatures and residence times as input. The script would then set the reactor to run each of conditions and analyse the product using on-line optical detection after a certain user defined delay time.

The user could also define whether the reactor should stop for optical detection and temperature change to save precursor solution, or continuously pump to reduce delay time needed to establish reliable flow. In order to minimise loss in reproducibility, it was preferred to work in the continuous pumping mode, as it causes less disturbance to flow within the reactor. A photograph of the entire synthesis platform is shown in figure 2.25. The schematic representation of the platform can be seen in figure 2.1 at the start of this chapter.

The optimisations were carried out using a custom-written class-based wrapper around Huyer and Nuemaier's original MATLAB implementation of SNOBFit by Walker *et al*.[45] This optimisation algorithm would recommend a list of reaction conditions to the reaction script and receive emission properties from the reaction script upon completing the recommended points. This information was fed back to SNOBFit for analysis, which the algorithm returning a new set of conditions based on the acquired data.

Figure 2.25: An overview of complete automated platform for nanocrystal synthesis. a) KD Scientific pumps, b) motorised valves, c) Galden HT270 stock bottle, d) Precursor reservoir, e) Droplet generator, f) Boxed heater with fan, g) Heater terminal for power supply and PC connection, h) Separator (in fixed pressure mode) and i) Optical detection flow cell.

2.2 Batch Synthesis and Adaptation to Flow

This section contains details of the chemicals and methods used for batch synthesis and their adaptation to flow. The optimisation of the synthesis procedure is described and a comparison of two carrier fluids.

2.2.1 General Materials

Solid metal precursors used in this work were: copper iodide (CuI), indium acetate (InAc), zinc acetate (ZnAc) and Sulphur (S). All of these were purchased from Sigma Aldrich. The non-coordinating solvent 1-octadecene (ODE), surfactant Oleic acid (OA) and surface ligand 1-dodecanthiol (DDT) were also obtained from Sigma Aldrich. Carrier fluids used in this work were Solvay Fomblin YL-Vac 16/6 and Galden HT270 from Kurt Lesker, UK.

2.2.2 Batch Synthesis of $CuInS_2$ and $ZnCuInS_2$

Flask (batch) synthesis was first carried out based on a published batch synthesis report (Lisensky *et al.* [2]) before adapting to flow synthesis. It should be noted work by Lisensky *et al.* only contains synthesis procedure for $ZnCuInS_2$ core/shell nanocrystals, and different behaviour in terms of reaction time is observed when removing the zinc shell precursor in the precursor combination. This step allowed user to familiarise with the synthesis routine for $CuInS_2$ based quantum dots, and gain empirical knowledge of the reaction behaviour, such as temperature dependency.

Methods

The reaction scheme for $ZnCuInS_2$ and $CuInS_2$ nanocrystals are shown in figure 2.26 and 2.27. In both cases 1-octadecene (ODE) serves as a non-coordinating solvent with high boiling point, and 1-dodecanethiol (DDT) acts as a sulphur source and surface ligand to prevent product aggregation. The metal precursor is dissolved with the assistance of oleic acid (OA) at 150 °C and DDT is thermally decomposed above 190 °C to provide sulphur to the reaction. For the $CuInS_2$ synthesis, the zinc precursor was omitted from the reaction mixture. Substantially shorter reaction times were obtained in the absence of zinc precursor.

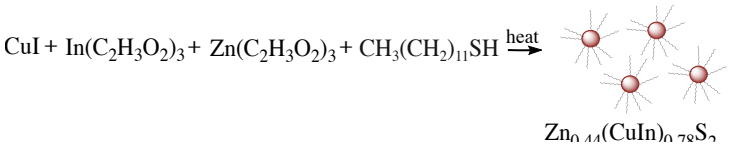

Figure 2.26: Schematic representation of the $ZnCuInS_2$ synthesis route. The precursor decomposes under high temperature and results in quantum dot formation. Here the 1-dodecanethiol serves both as a sulphur source and a ligand to prevent product aggregation.

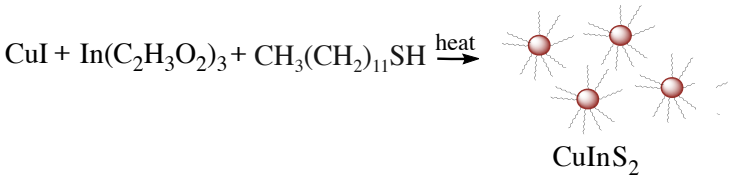

Figure 2.27: Schematic representation of the $CuInS_2$ synthesis route, in which the zinc precursor has been omitted from the reaction. This reaction occurs much faster due to absence of zinc precursor.

The flask synthesis was carried out in a three-neck flask and connected to a Schlenk line with vacuum and nitrogen supply. For $ZnCuInS_2$ quantum dots, 0.0267 g (0.14 mmol) of CuI, 0.0409 g (0.14 mmol) of InAc, 0.22 g (0.14 mmol) of ZnAc, 1 ml of 98% 1-Dodecanethiol (DDE), 0.23 ml of oleic acid and 16 ml of octadecene (ODE) were added to the three-neck flask. For core $CuInS_2$ quantum dots, the zinc precursor was omitted from the reaction mixture. The reagent mixture was degassed for 1 hour before heating up by a heating mantle under nitrogen atmosphere. The reaction mixture was first heated up to 150 °C. At this temperature, it was observed that metal precursors were completely dissolved, and the mixture became a clear fluid with a light-yellow colour. This observation is consistent with both core and core/shell synthesis. To heat up the reaction mixture from room temperature to the set-point, here 218 °C, required approximately 45 minutes.

For core $CuInS_2$ quantum dots, the reaction mixture was heated up to 218 °C, and a rapid colour change from light yellow to red-orange was observed once the mixture had reached this temperature. This rapid colour change is an indicator of quantum dots formation, as the emission wavelength increases with increasing size of the quantum dots. Samples were collected at 80 second intervals and left to cool down to room temperature for further analysis. It is observed that the longest reacted products tend to aggregate into large visible sand-like clusters.

For $ZnCuInS_2$ quantum dots, the precursor mixture was heated for 45 minutes at 218 °C, and a similar colour change to red-orange was observed after 45

minutes induction period. Samples were taken at 3 minute intervals from 45-minute mark and left to cool down to room temperature. The last sample had a very dark red colour. It was observed that for temperatures below 210 °C, the reaction required about 2 hours to reach a similar stage as for 45 minutes heating at 218 °C. It was again observed that the longest reacted products tended to aggregate into large visible sand-like clusters.

In both syntheses, a red shift of the emission peak was observed with increasing reaction time as shown in figure 2.28 below, which is the consequence of particle growth and is consistent with decreasing quantum confinement, see introduction chapter.

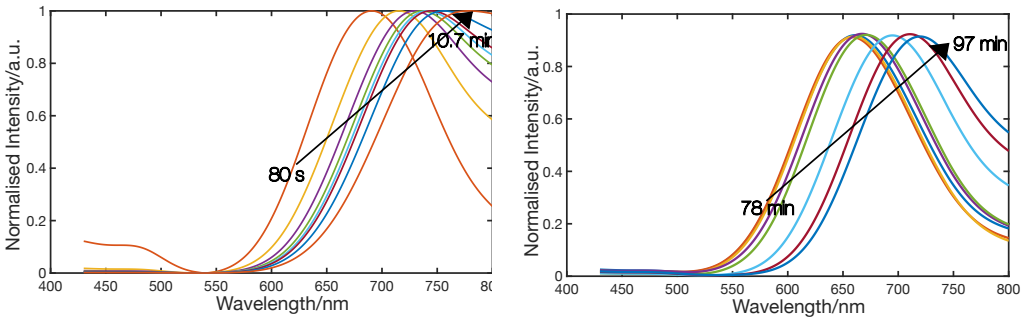

(a) (b)

Figure 2.28: a) Normalised emission spectrum from a series of core $CuInS_2$ QDs synthesis at 218 °C. The first product was collected 80 seconds after the reaction mixture reached 218 °C, subsequent products were taken at 80 second intervals. a) Normalised emission spectra from a series of core/shell $ZnCuInS_2$ QDs synthesis at 218 °C. The first product was collected after 78 minutes, and subsequent products were taken at 3 minutes intervals

Core $CuInS_2$ synthesis was first conducted, and the rapid colour change was observed as the reaction mixture reached 218 °C. This reaction was then repeated with zinc precursor added, and the induction time was noticeable prolonged. The reaction time required for nucleation and growth went from 80 seconds without zinc to around 78 minutes with. From other reports [51, 52], the incorporation of zinc shell occurs via a cation exchange process with the Zn substitute some of the Cu ions in the crystal lattice. This process requires longer time and is consistent with our experimental observations. The photoluminescence quantum yield (PLQY) was not measured in this work, but it has been observed that higher PLQY were obtain for core/shell QDs under illumination with an excitation source compared to core QDs. This is preferred for fluorescence applications that requires high luminescence property.[53] This increase in PLQY is mainly due

to the reduction in defects in the core nanocrystals that led to increasing radiative recombination pathways in the material.

Reproducibility of a specific synthesis is an important factor for industrial quality production, and when using batch synthesis for nanocrystals, the products can vary significantly between nominally equivalent batches. A typical example of large product variation is shown in figure 2.29. The emission peak is shifted by 30 nm between the two core/shell $ZnCuInS_2$ synthesis that were carried out with nominally identical procedures. There are many factors that could account for this large variation between batches. These factors are most likely to be operation related, such as imprecision in weighing out the chemicals and subsequent transfer to the reactor, or poor temperature control of the heating source.

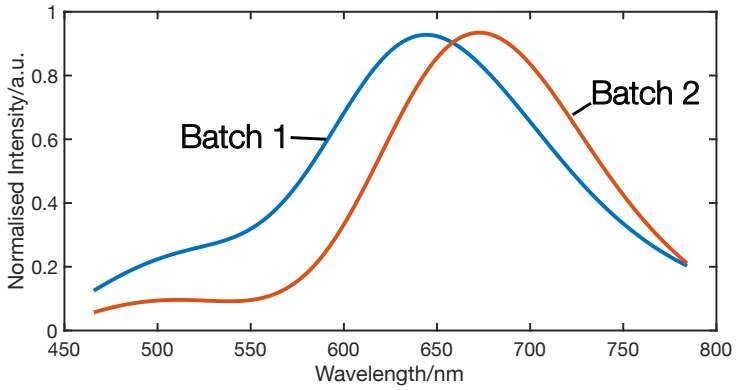

Figure 2.29: Comparison between two flask syntheses with nominally identical synthesis procedures. The emission peak is shifted by 30 nm between the two batches.

The aim of this work was to use our designed automated flow synthesis platform to achieve automated synthesis, aiming to improve the product reproducibility. In using the automated synthesis platform, one large precursor stock is often sufficient for a very long synthesis, eliminating the potential operation error in preparing many stock solutions. However, it is inevitable that one precursor stock runs out, and new stock solution might behave slightly different. Therefore, the reaction conditions should be reoptimised to the new stock with predetermined product features, either to match old product or improve based on the requirements. This can realised here by combining the automated flow platform with an optimisation algorithm, thus achieving on-demand product features for each new stock solution. One can for example carry out an optimisation of product features by constrained optimisation to match the previous products with different stock solutions for consistent products throughout different batches of precursor.

2.2.3 Adapting to Flow

Flow synthesis aims to improve the reproducibility of a synthesis and increase the efficiency by providing enhanced chemical and temperature uniformity as discussed in the introduction. In this work, synthesis procedures for $CuInS_2$ and $ZnCuInS_2$ were adapted to flow, and subsequent precursor optimisation and parameter screening was performed to identify the best parameter window for the automated and optimisation synthesis of core $CuInS_2$ nanocrystals. Additionally, Fomblin YL Vac 16/6 and Galden HT270 carrier fluids were tested to determine their suitability with respect to the flow reactor.

Initial Adaptation

In the initial adaptation phase, precursor stocks were prepared at same concentration as batch synthesis by identical procedures, i.e., degassing for 1 hour and heating up to 150 °C until the mixture became transparent with a light yellow colour. The reaction mixture was then left to cool to room temperature prior to transferring it to a syringe. PTFE tubes were were used for the reactor channel with a length of 1.5 meters, 1 mm inner diameter and 2 mm outer diameter. PTFE has an upper working temperature of around 240 °C. Below the temperature it can be used extensively without degradation and hence is suitable for the intended syntheses . For my initial work, chemically inert Fomblin YL-Vac 16/6 high density perfluorinated polyether (PFPE) was used as carrier fluid. The required flow rate was calculated by $Q(\mu/min) = \frac{250*pi*L_{reactor}(m)}{T_{reaction}(min)}$, where L is the length of the reactor channel in meters and T is the target residence time within the channel in minutes. A total flow rate of 52.4 μl/min corresponds to a residence time of 22.4 minutes and was used as target residence time in adapting the core/shell $ZnCuInS_2$ synthesis to flow. Hence the two syringe pumps were set to 26.2 μl/min each kaing a total flow rate of 52.4 μl/min. For core $CuInS_2$ nanocrystals, the total flow rate was set to 392.7 μl/min, corresponding to a residence time of 3 minutes. The heater was set to 220 °C for both syntheses. Both syringes were connected to tubing platform via Luer connectors. A photograph of reacted product droplet is shown in figure 2.30

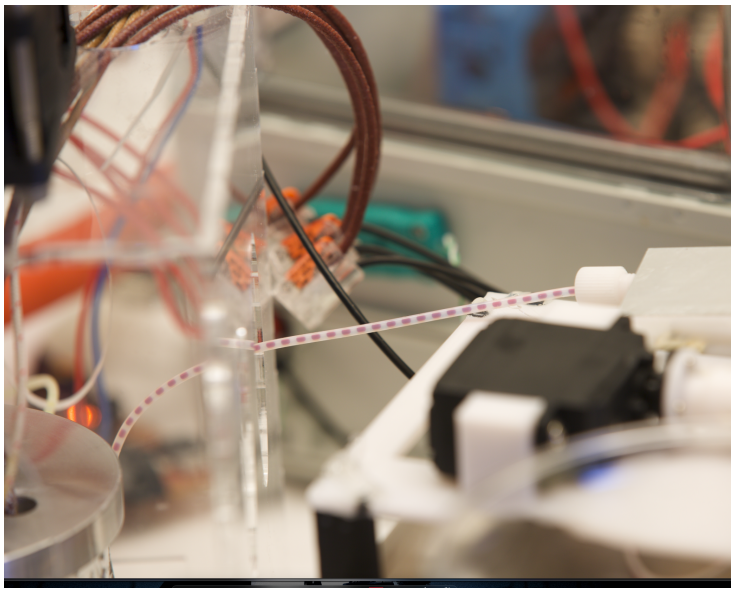

Figure 2.30: A Photograph depicting reacted product droplets exiting the heater. A video of reacted droplets exiting the reactor can be seen here `https://youtu.be/s0EfO08EooM`

Results from Initial Adaptation

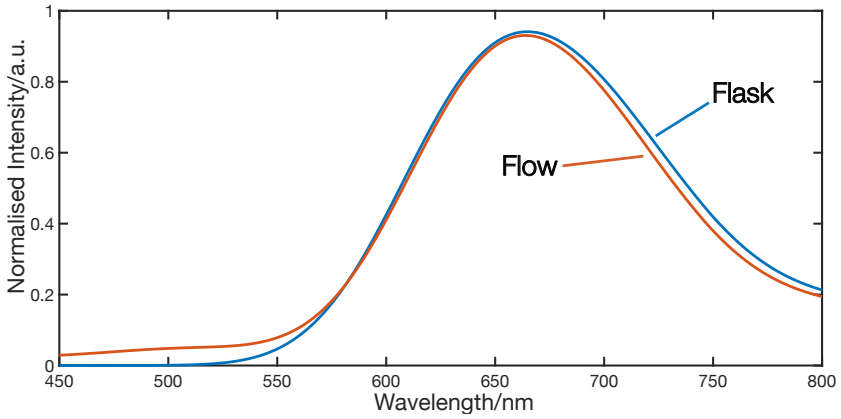

Figure 2.31: Overlaid emission spectra for flask and flow synthesised $ZnCuInS_2$ QDs. Flask product was obtained after 80 minutes reaction time. Flow product was obtained from the reaction after a 22.4 minutes residence time at 220 °C.

Flow synthesis typically increases the reproducibility of a synthesis and reduces the reaction time due improved heat and mass transfer in. the small channels

typically employed. This reduction in reaction time is particularly noticeable for the core/shell $ZnCuInS_2$ synthesis. With a target reaction time to 22.4 minutes, the product exhibited similar emission features to that obtained by a 80 minutes batch synthesis product as seen in figure 2.31.

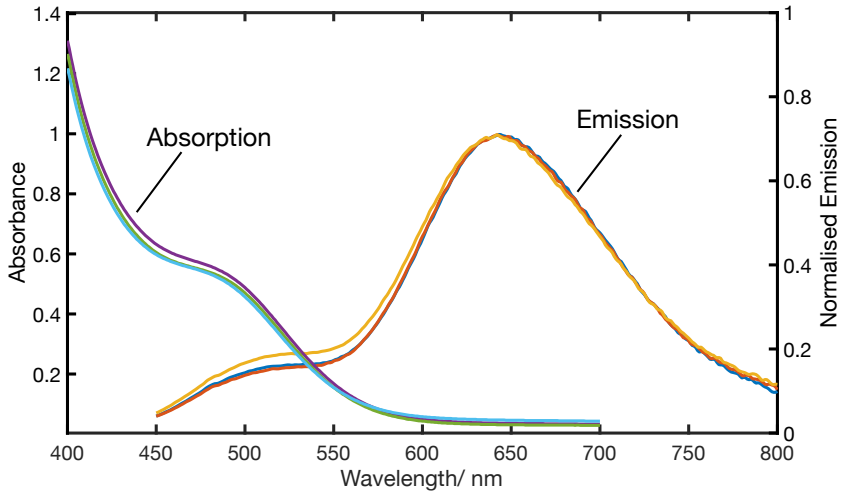

Figure 2.32: Three overlaid spectra from a five-hour synthesis run obtained using a 22.4 residence time at 220 °C. Products were collected at 90 minute intervals. The results show consistent absorption and emission features, indicating stable reactor performance over the five hour runs.

In these stages of the project flow syntheses were performed in a manual mode, meaning the user needs to reload the syringe manually, if the precursor or carrier fluid ran out in the syringe. However, choosing a syringe size of 100 ml allowed user to perform a synthesis for many hours. It was therefore possible to test the reproducibility of the reactor by performing a long synthesis experiment. Figure 2.32 shows an overlay of absorption and emission spectra for a five-hour synthesis run with a 22.4 minutes reaction time at 220 °C. The products were collected at 90 minut intervals. The closely overlapping spectra confirms the reactor is able to produce equivalent product consistently over a long synthesis experiment.

The typical 22.4 min reaction time used for the previous flow experiment is inconveniently long for an extensive screening of many reaction conditions or for performing an optimisation routine with limited time. Let us assume each reaction condition requires us to wait 3 residences time for the system to properly stabilise, then for a 20 min reaction time we would need one hour to test each synthesis condition. For a 40 points optimisation with an average 20 min reaction time, this would require almost two days to complete. This large time consumption is considered impractical for this work, despite the dramatic increase in efficiency

compare to its batch routine, as we wanted to perform rapid parameter probing for optimisation. From the batch measurement I had found that core $CuInS_2$ nanocrystals have a much short reaction time compared to the core/shell synthesis. Therefore, author decided to work with core $CuInS_2$ nanocrystals in this work for more efficient parameter screening and optimisation

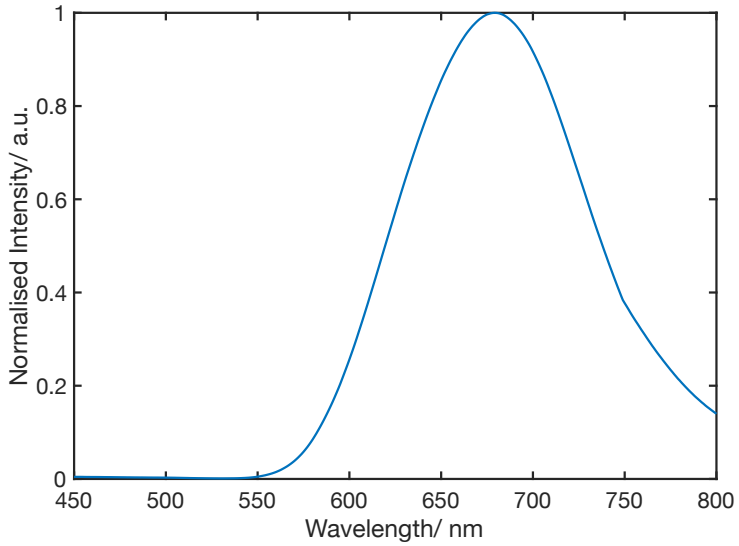

Figure 2.33: Emission spectrum of core $CuInS_2$ nanocrystals with 3 minutes reaction time at 220 °C in flow. The emission peak is 679 nm.

Figure 2.33 shows an emission spectrum of core $CuInS_2$ nanocrystal by flow synthesis. The reaction conditions used in this synthesis were 3 minutes residence time and 220 °C. Here we are observing an emission spectrum that is similar to the batch synthesised nanocrystals obtained 80 seconds after reaching 218 °C see figure 2.28a). However, this doesn't mean the flow reactor is inefficient compared to batch synthesis. In a batch synthesis, the reaction mixture was gradually heated up to the set-point over 40 mins, and this was not counted as part of the 80 s reaction time. During this heating up process, DDT gradually decomposes and therefore we were obtaining 80 seconds reaction time at the set-point (218 °C). In flow synthesis, the reagents are cold as they enter the reactor, and starts heating up only when they reach the heater. Thus, the entire heating process plus the quantum dots formation is in total 3 minutes, and in this regard flow reactor provides greatly enhanced production rate. A video showing the droplets within the reactor is shown here: `https://youtu.be/tVl0V1tBQyE`. The progressive darkening of the droplet colour seen in the video as the droplets proceed downstream is consistent with batch growth observation.

Precursor Optimisation

The above synthesis used a precursor composition of 0.14 mmol of solid precursor in 16 ml ODE, 1 ml DDT and 0.23 ml OA. This combination relied on 1-dodecanethiol decomposing during heating (above 190 °C) to provide a sufficient sulphur source for nanoparticle growth. In order to make this decomposition efficiently, I was forced to work at high temperatures above 215 °C in order to achieve residence times below 10 minutes. This had some practical consequences that we wished to avoid.

As previously mentioned, the upper temperature range for the PTFE tubes is around 240 °C, and author wanted to work in a safer region at least 15 °C below this upper limit to avoid any potential accident, e.g., overshooting of the heater. This left a very narrow window of usable temperatures from 215 °C to 225 °C for synthesis. This meant there was a limited opportunities to explore the effect of temperature parameter space. Therefore, we wished to find way to lower the lower temperature bound due to investigate a wider range of temperatures. This was realised by combining a preprepared sulphur solution and a more concentrated precursor stock solution at room temperature. Using the new stock solution quantum dots could be obtained at a lower temperature bound of 160 °C. The modified precursor preparation procedure is described below.

The new precursor stock composes 0.10475 g (0.55 mmol) CuI, 0.16057 g (0.55 mmol) InAc, 1 ml DDT, 1ml OA and 9 ml ODE. The chemicals were added to a three-neck flask, degassed for 1 hour and heated to 150 °C in nitrogen atmosphere for 90 minutes under stirring and left to cool down to room temperature. By this procedure we obtaineda 0.05M CuIn precursor solution, which was 40 times more concentrated compare to previous solution. For the sulphur solution, 0.03527 g (1.1 mmol) pure sulphur, 1 ml DDT and 10 ml ODE were added to a three-neck flask, degassed for 1 hour and heated up to 150 °C in nitrogen atmosphere for 90 minutes under stirring. This 0.1 M sulphur solution was then left to cool down to room temperature. Both solutions were mixed together before loading into a syringe, such that we obtained a stoichiometric ratio of 1:1:2 for Cu:In:S.

With the new stock solution, we have shifted from using 1-dodecanthiol as sulphur source to using pure sulphur and DDT is now used primarily as a surface ligand. This allow quantum dot formation at lower temperature, without the necessity to decompose the thiolate, enabling us to make quantum dots over a wider range of temperatures.[54] Figure 2.34 shows overlaid emission spectra of core $CuInS_2$ quantum dots with both the old and new precursor solution. The residence time and temperature for the new synthesis were 277 seconds and 160 °C, yielding an emission peak at 680 nm with the old precursor, a similaremission peak of 680 nm was obtained at a condition of 220 °C and 3 minutes residence

time. Hence using the new method, we were able to obtain $CuInS_2$ with close matching emission properties at 60 °C lower temperature and similar residence time. This precursor preparation method could be linearly scaled for preparing large stock solutions without further modification and was stable at room temperature, the reminder of the work reported here used this procedure to prepare stock solutions for both automated synthesis and optimisation.

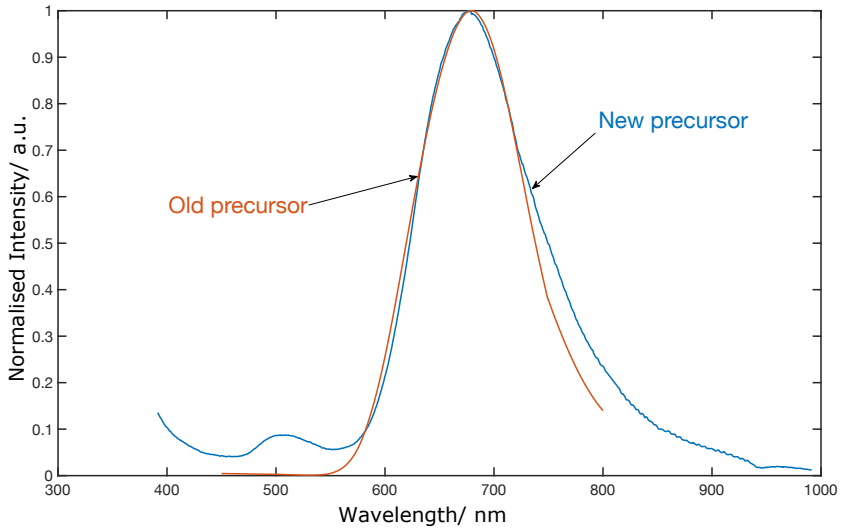

Figure 2.34: Overlaid emission spectra of core $CuInS_2$ quantum dots obtained using the old and new precursor solutions. For the quantum dots produced with old precursor solution, reaction conditions were set to 180 seconds residence time and 220 °C. For the quantum dots produced with the new precursor solution, the reaction conditions were set to 277 seconds and 160 °C. Here, the emission peak is at the same position, 680 nm, with new precursor solution has a 10 nm wider linewidth and found to be 127nm, the small peak around 500 nm corresponds to the emission of precursor mixture.[2] The emission spectrum for the old precursor product was acquired with a bench top fluorescence spectrometer and had a scanning wavelength from 450 nm to 800 nm, such that the emission spectrum ended at 800 nm.

Choice of Carrier Fluid

The carrier fluids used to establish a two-phase flow in this work were PFPE fluids with different temperature-dependent viscosities and high temperature tolerance. During the development and adaptation phase, Fomblin YL 16/6 was extensively used. However, we encountered two major issues with using Fomblin. One of them (as previously mentioned) was that it was difficult to achieve complete

separation of the two liquids. Another issue is Fomblin induced fouling, which is the exact problem we aim to avoid by using a carrier fluid.

The heater in this work was designed such the PTFE tubing could wrap around the heater, and a layer of aluminium was then wrapped over the tube aiming to provide a uniform heating to the tubing. But there was expected to be a small temperature gradient within the tubing due to constant airflow from the fan to the outer side of the channel. This is usually not a problem, as the droplets are around 6 microliters, and undergo efficient diffusive mixing within each droplet. However, this becomes problematic when using a carrier fluid that shows a large viscosity variation over a small temperature range, which is the case for Fomblin as seen in figure 2.21a. The side of the channel in contact with the heater has a higher temperature profile and outer side has a slightly lower temperature, such one obtains different viscosities of Fomblin within the same channel section. This means the frictional force with the wall is larger at outer side compared to the inner side that is in contact with heater, this leads to a difference in flow rate of the two side in each droplet. This leads to droplets having an elongated shape with more fluids in the high temperature region of the channel section.[55, 56] For long synthesis times, it is possible for quantum dots to wet and attach to the high temperature part of the tubing wall permanently, which leads to channel fouling, and was observed during the synthesis. A schematic illustration of this behaviour is shown in figure 2.35 and a fouled tube caused by this behaviour is shown in figure 2.36.

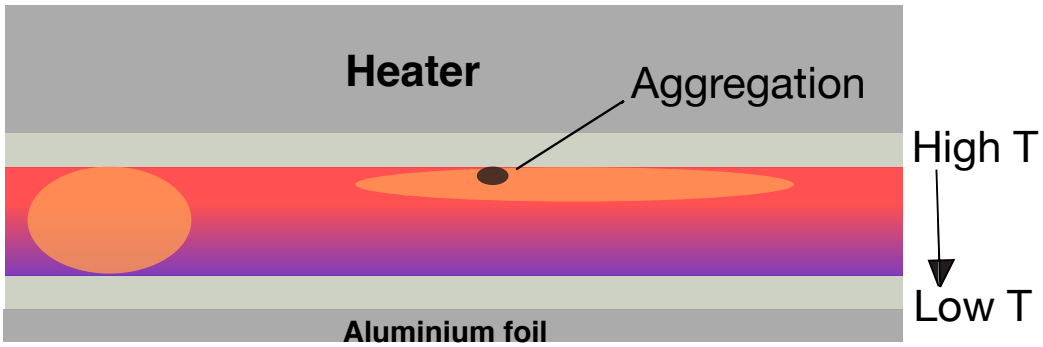

Figure 2.35: A schematic illustration of Fomblin induced fouling when channel is experiencing non-uniform heating. Here the viscosity difference is shown in the gradual colour change from red to purple. The product droplet is shown in orange colour, and aggregation zone caused by preferential wetting is shown in black colour. This behaviour occurs as the droplet shape are elongated due to the shear force as flow rate difference caused by different viscosity profile.[3, 4]

Figure 2.36: A photograph of a fouled tube using Fomblin as a carrier fluid. The black materials are wetted aggregated quantum dots due to long usage.

Therefore, inherently low viscosity and less temperature sensitive Galden HT270 was used for the rest of this work. Using Galden eliminated the carrier fluid induced reactor fouling behaviour and allowed for easier separation of ODE and the carrier fluid.

2.2.4 Summary

In this chapter I presented the development process for setting up an automated flow synthesis platform for nanocrystal synthesis, and the adaptation process of $CuInS_2$-based quantum dots to flow synthesis.

CHAPTER 3

RAPID PARAMETER SCREENING BY AUTOMATED SYNTHESIS

Automated synthesis with on-line analysis as discussed in the introduction enables a user to test multiple reaction conditions in a sequential order with the possibility to perform real-time analysis of the products for each condition. This gives the user the possibility to run large, automated sampling experiments in a time efficient manner. Such sampling experiments were conducted in this chapter with rapid change of conditions.

3.1 Latin Hypercube Sampling

Latin hypercube sampling (LHS) is a statistical sampling method that tests each reaction parameter over its full range of allowed value through sampling a limited randomised points in the user defined parameter space. This method offers great benefits in terms of sampling efficiency by using relatively few generated points to cover the defined parameter space.

The sampling works by dividing N variables in a function with M equally probable intervals. In this work, we are choosing temperature and residence time as sampling variables, thus we will obtain a M-by-M grid in a two-dimensional plane, representing a stratified two-dimensional parameter space. We will then make a randomised selection inside each stratum without double counting the variables. The sampling order is also randomised for this work, such the reactor undergoes bidirectional parameter changes to test its ability to accommodate such parameter change.

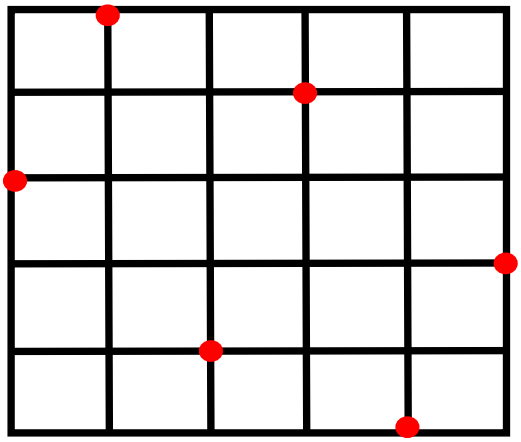

Figure 3.1: A graphical representation of a Latin hypercube sampling. Here, the number of variable is a N=2, and the number of points M = 6. N and M form a two-dimensional grid with $M^N = 6^2 = 36$ nodes representing the possible reaction conditions. The nodes marked in red are of the conditions selected for sampling.

In order to confirm the reproducibility in the synthesis platform, we will repeat the sampling sequence minimum three times. This allows user to analyse whether the obtained data from the platform are consistent, i.e. the same conditions always give broadly the same product. Consistency is important for automated reaction optimisation, as the algorithm depends on the consistent behaviour feedback to find the optimum input parameters.

3.2 Sampling Experiment 1

Method

For the first experiment, lower and upper temperatures were set to 180 °C and 225 °C respectively. The reaction time bounds were set to 100 seconds and 300 seconds. The parameters were partitioned into 6 equidistant values, shuffled and randomly paired. The parameter space and pairing for this experiment is shown in figure 3.2. The reaction conditions were tested in a randomised order, such that both syringe pumps and heater executed changes in both directions. This sampling was performed four times in a sequential order during one workday in one automated experiment. The delay between the start of a new condition and spectroscopic analysis was set to twice the current residence time. It should be noted that the spectrometer cooling was disabled due to absence of necessary component in this sampling experiment, and O.D. filter was installed in front of

the photodiode to reduce the laser beam (first configuration) for laser intensity monitoring, as previously mentioned in the chapter 2.

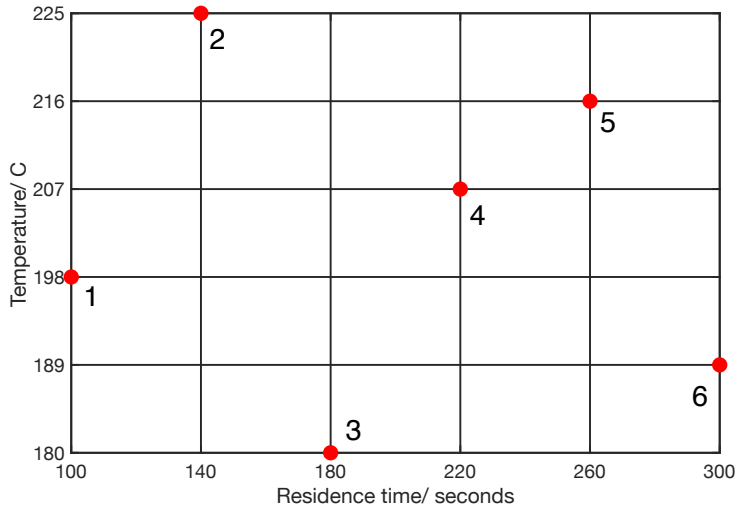

Figure 3.2: Parameter space for Latin Hypercube sampling experiment 1. The red dots are the reaction conditions to be investigated.

Results and Discussion

The reaction conditions for simplicity were labelled 1 to 6 in order of increasing residence time with their corresponding temperature as seen in figure 3.2. The first reaction condition pair was 100 seconds residence time with 198 °C temperature, the second condition was 140 seconds, 225 °C and so on. The sequential order for the conditions was 6, 4, 5, 1, 3, 2 during each sampling round. The emission peak and peak intensity results are given in table 3.1 and table 3.2 respectively.

Reaction Conditions	Synthesis 1	Synthesis 2	Synthesis 3	Synthesis 4	Standard Deviation
1	677.97 nm	677.21 nm	677.97 nm	680.26 nm	1.32 nm
2	733.42 nm	734.17 nm	734.17 nm	734.93 nm	0.62 nm
3	671.87 nm	674.92 nm	673.39 nm	674.92 nm	1.45 nm
4	710.68 nm	714.47 nm	711.44 nm	711.44 nm	1.68 nm
5	731.15 nm	731.15 nm	734.17 nm	731.15 nm	1.51 nm
6	694.72 nm	691.68 nm	693.96 nm	692.44 nm	1.39 nm

Table 3.1: Table of emission peak wavelengths measured in the first sampling experiment. The spectrometer cooling was disabled in this experiment.

From this data, we observe small standard deviations in wavelength with

maximum value of 1.68 nm for reaction condition 4. This deviation range was within the expectation and confirms overall reproducibility by using the platform.

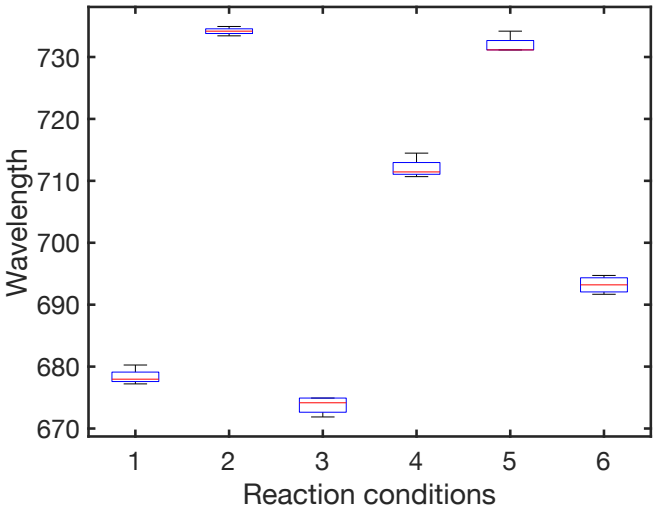

Figure 3.3: Box plot of the emission peak for synthesis conditions. We observe the emission peak variations in each synthesis are within 3 nm error, confirms the desired synthesis reproducibility.

In this run, the temperature was rapidly changed from lower to upper bound (condition 3 to 2), and from table 3.1 we observe close matching peak wavelengths for both conditions. The observed consistency in wavelength data suggests the heater designed in this work coupled with the syringe pumps are capable of perform large condition changes with high reproducibility, resulting in quantum dots with consistent peak wavelengths. This confirms the desired synthesis reproducibility when using the automated synthesis platform. However, undesired visible aggregates were observed in the reaction channel during condition 2, 4 and 5 which led to fouling in the separator. These conditions corresponds to the highest temperatures tested.

From table 3.1, we can observe an intuitive temperature dependency in particle growth. Condition 2 and 5 was respectively 140 seconds residence time, 225 °C and 260 seconds residence time, 216 °C, and similar product emission peak around 730 nm. The emission wavelength as discussed in introduction is a function of particle size, with larger particles emitting at longer wavelength due to smaller band gaps. This suggests similar particles sizes were formed with condition 2 and 5, where longer reaction time is required to compensate the lower temperature, due to reduced growth rate with same precursor solution.

Reaction conditions	Synthesis 1	Synthesis 3	Synthesis 3	Synthesis 4	% STD
1	18.55	11.70	19.49	23.783	27.21%
2	33.49	39.03	34.86	49.75	18.75%
3	8.10	8.23	15.47	13.13	32.67%
4	28.66	25.04	75.93	41.39	54.26%
5	63.23	63.66	56.16	44.49	15.73%
6	26.64	18.73	40.52	31.71	33.34%

Table 3.2: Table of emission intensity corrected for laser intensity at emission peak in the first sampling experiment. Here, the spectrometer cooling was disabled. In the intensity data, we are obtaining large emission intensity fluctuation with minimum 15%.

The corresponding intensity values of the emission peaks are presented in table 3.2. From table 3.2, it is evident that large standard deviations (around 30%) in the intensity values were observed for each reaction condition pair with the extreme case to be 54% of the mean value. I will discuss this behaviour in a bit. But firstly, I will look at the data from condition 2 and 5 which exhibited lower standard deviations of around 15% relative to the mean values.

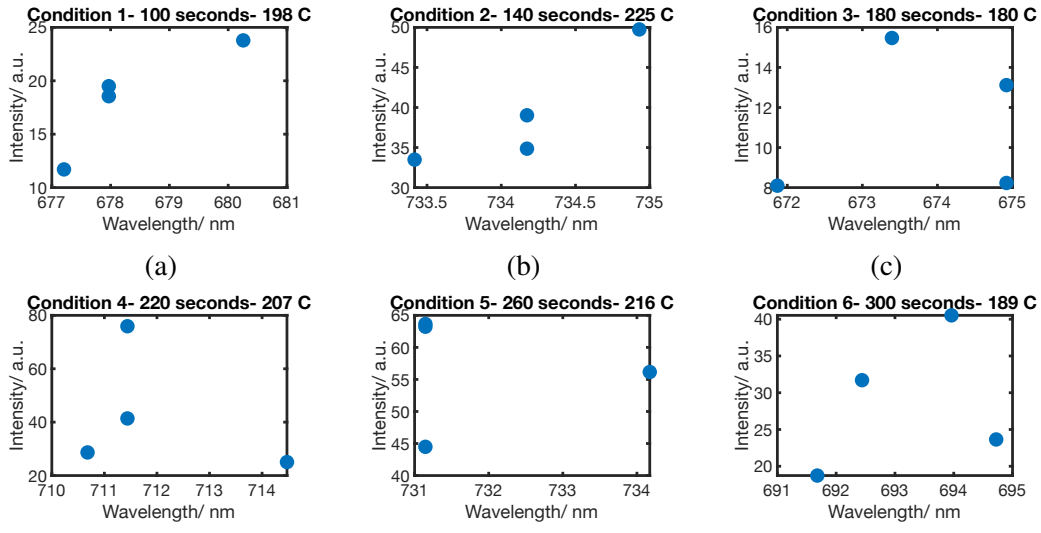

Figure 3.4: Scatter plot of wavelength and corresponding intensities in each reaction condition in experiment 1.

From table 3.1 it is clear that the emission peaks for condition 2 and 5 were closly matching at around 733 nm, implying similar particles size were obtained

from the two conditions. From scatter plots in figure 3.4 and the box plot in figure 3.5 below, we see that condition 2 had overall lower intensity values compared to condition 5. As discussed in the introduction, under-coordinated particles contain more surface defects that contribute to non-radiative recombination, which in turn reduces the photoluminescence in the products. Here thiolate acts as a passivation ligand, and the efficiency of passivation is dependent on the reaction time due to its diffusive process and the steric limitation.[57, 58] Such shorter residence time leads to more under-coordinated particles and leads to lower emission intensity. Thus, we obtain higher intensity with longer reaction time (condition 5) compared to shorter reaction time (condition 2) despite having the close matching emission peaks.

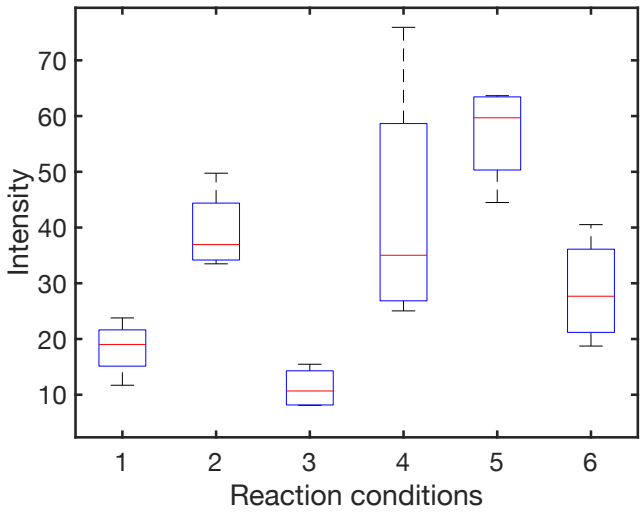

Figure 3.5: Box plot of intensity values from sampling experiment 1. Red line is the mean value, with whiskers representing the extreme intensities in each reaction condition.

The main observation from the intensity data is that there is a large standard deviation in the measured intensity (see the box plots in figure 3.5). As discussed in previous section, highly reproducible products were formed by the platform, therefore we can rule out synthesis hardware as the cause of the large deviations. The optical detection system is a potential candidate for the inconsistent intensity values. Therefore, we investigated possible source of error in the optical detection system.

The optical detection configuration in the previous experiment used a spectrometer detector with cooling disabled due to absence of necessary components. As previously discussed in Chapter 2, the TE cooling reduces the

dark noise in the CCD detector by cooling down the detector temperature.

To acquire a non-saturated laser spectrum, the integration time was set to 8 microseconds. The spectrometer was set to take 1500 averages with 1.5 microseconds between each acquisition to avoid overloading the spectrometer processor, the entire process required about 20 seconds to obtain an averaged laser spectrum. The averaging of the emission intensity reduced the influence of noise in the system. A typical spectrum for the laser can be found in figure 2.18 in Chapter 2, a single sharp peak at 355 nm with extremely narrow linewidth determined by the resolution ofthe spectrometer. Laser intensity measurements against time are present in figure 3.6 for both the photodiode and uncooled spectrometer, 240 measurements were recorded within 80 minutes time. The normalised intensities measured by the uncooled spectrometer drifted around 20% during acquisition period. However, the laser intensity by the photodiode remained stable to within 1%. This suggest that the intensities measured by the spectrometer with cooling disabled is the main cause of the large apparent changes in intensity seen in figure 3.5.

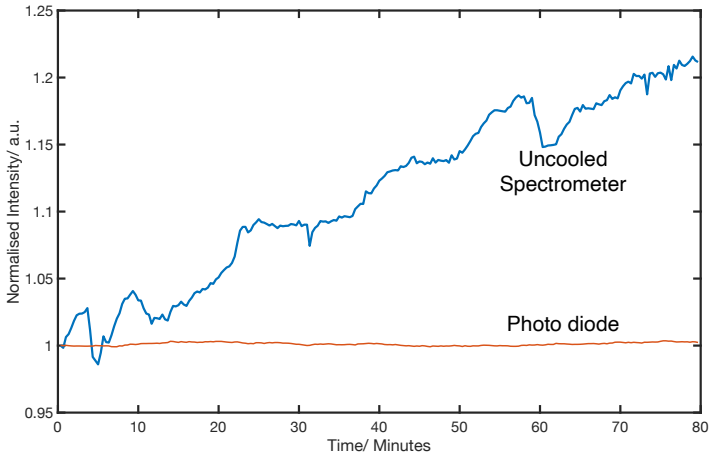

Figure 3.6: Normalised laser intensity vs time as determined by uncooled spectrometer and laser diode. The orange line represents the laser intensity recorded by photodiode. The intensity value recorded by the spectrometer drifted by around 20% over an 80-minute recording interval.

I tested whether the drift in the measured intensity by the spectrometer could be reduced by enabling the thermoelectric cooling system in the spectrometer. The spectrometer manual suggested the TE cooler should be set to -5 °C. Thus, a new

measurement was performed with TE cooling enabled to -5 °C. The laser intensity was sampled for approximately 1 hour by the cooled spectrometer and photodiode, as shown in figure figure 3.7. The laser intensity as determined by the photodiode varied within 1% (yellow line) as before and which the laser intensity measured by the spectrometer varied by about 4%, much less than without TE cooling. It is evidently important to enable TE cooling when utilising the automated platform to improve the data consistency.

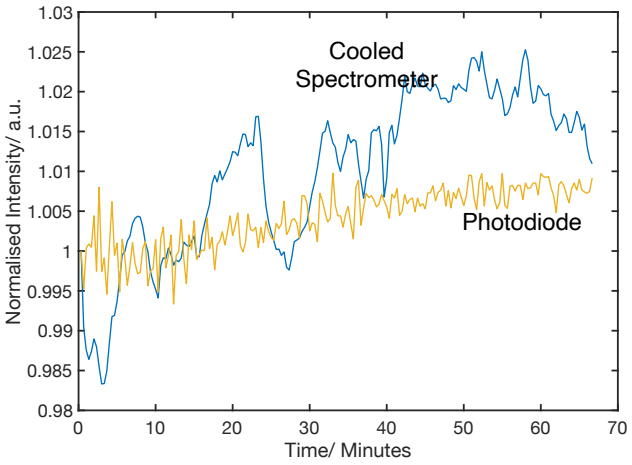

Figure 3.7: Normalised laser intensity vs time recorded with photodiode and a cooled spectrometer, the orange line represents the laser intensity recorded by photodiode. Here the spectrometer CCD detector cooling was set to -5 °C.

The spectrometer can be cooled to -15 °C, and it was therefore interesting to explore if the lower set-point would further improve the data consistency. The measurement was repeated with set-point to both -8 °C and -10 °C. The data from both samplings are given in figure 3.8 and 3.9. We can see that in both cases, the variation is around 4%, similar to previous data where the TE cooling set to -5 °C.

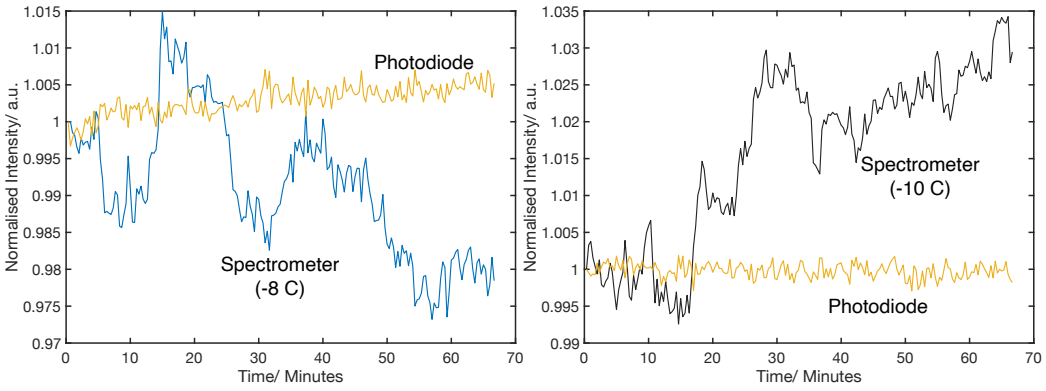

Figure 3.8: Laser intensity measurements recorded by spectrometer and photodiode. Here photodiode recording is indicated in yellow colour. a) The spectrometer was cooled to -8 °C, the measured intensity variation as determined by the spectrometer was around 4%, while according to the photodiode the laser variation was lesser than 1%. Right) The spectrometer was cooled to -10 °C; the intensity measured by spectrometers varies around 4% similar to -8 °C measurement without improvement.

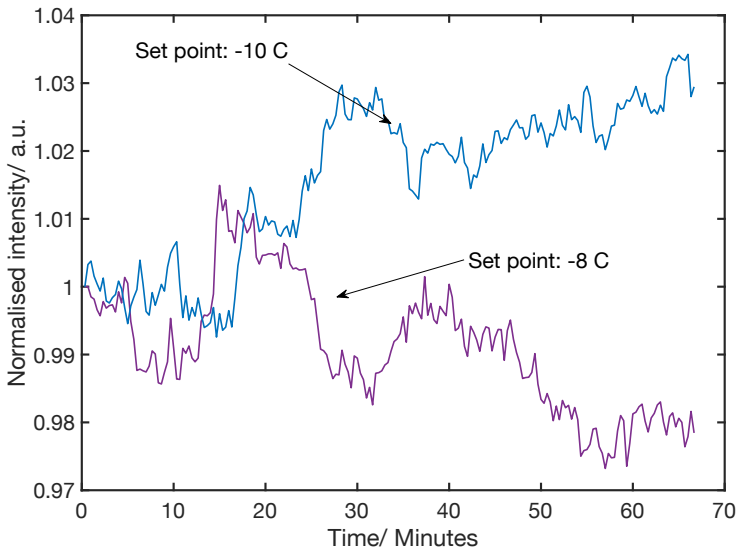

Figure 3.9: Overlaid data measurements from both cooling temperatures. No clear reduction or trend in intensity variation.

Thus, we can conclude that lower set-points in the TE-cooling do not provide improvement in data variation compared to the recommended set-point of -5 °C.

Therefore, for the second hypercube sampling, the optical detection configuration was improved using TE cooling at -5 °C.

3.3 Sampling Experiment 2

From the last sampling, we observed aggregate formation at high temperatures ($>$ 205 °C) conditions, which caused separator fouling. Thus, in this experiment, we reduced the upper temperature limit to 210 °C and the residence time to 220 seconds. The parameter space for the new experiment is presented in figure 3.10. Due to limited precursor, only five sets of conditions were tested this time.

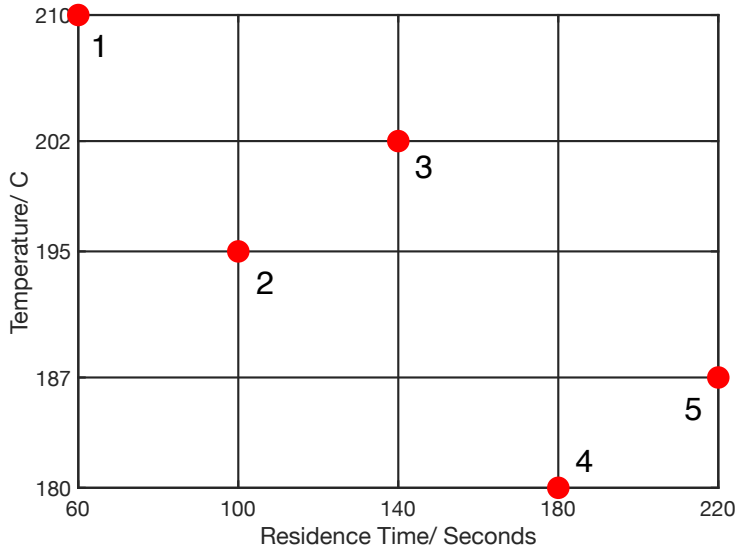

Figure 3.10: Parameter space for Latin Hypercube sampling experiment 2. The red dots are the reaction conditions to be investigated.

Results and Discussion

The five reactions conditions are labelled as condition 1 to 5 in the order of increasing residence time for simplicity, with condition 1 being 60 seconds and 210 °C, and condition 2 being 100 seconds and 195 °C and so on. The sequential order for the conditions was 4, 2, 3, 5, 1 during the sampling experiment. The sampling was again repeated four times, with corresponding wavelength and intensity data given in table 3.3 and 4.

Reaction Conditions	Synthesis 1	Synthesis 2	Synthesis 3	Synthesis 4	Standard deviation
1	701.57 nm	700.81 nm	700.81 nm	700.81 nm	0.38 nm
2	692.44 nm	698.52 nm	697.76 nm	697.00 nm	2.7336 nm
3	709.16 nm	709.92 nm	712.20 nm	709.16 nm	1.44 nm
4	685.60 nm	684.83 nm	686.35 nm	684.83 nm	0.73 nm
5	697.76 nm	700.81 nm	697.76 nm	700.81 nm	1.76 nm

Table 3.3: Table of emission peak wavelengths measured in the second sampling experiment with spectrometer cooling enabled.

The peak wavelength results from the second sampling were consistent from the previous experiment, with higher temperatures giving higher growth rates and longer peak wavelengths. Undesired aggregates were again observed in condition 3 which involved moderately high temperatures and reaction times.

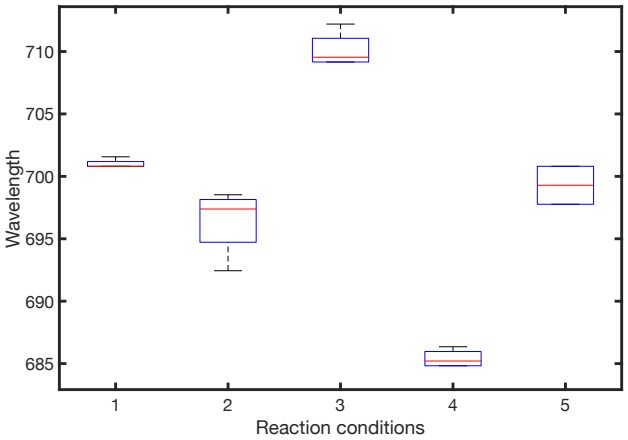

Figure 3.11: Box plot of the emission peak wavelengths for sampling experiment 2, here we see majority of the wavelengths are highly consistent similar to previous experiment

From the box plot in figure 3.11, we can see that in terms of peak wavelength the syntheses are highly reproducible, with one outlier in condition 2 that resulted in anomalously low wavelength. The corresponding intensities presented in table 3.4.

Reaction conditions	Synthesis 1	Synthesis 2	Synthesis 3	Synthesis 4	%STD
1	27.03	17.76	28.58	36.68	28.19%
2	21.81	27.98	22.93	20.28	14.35%
3	26.96	36.57	31.17	30.57	12.66%
4	18.42	22.93	22.00	18.41	11.58%
5	33.98	27.27	25.25	27.45	13.32%

Table 3.4: Table of emission intensity corrected for laser intensity at emission peak in the second sampling experiment. Here, the spectrometer cooling is set to -5 °C.

Here, we can see the standard deviations in percentage are around 15% besides condition 1, which is a significant reduction in variation compared to previous sampling, due to the improved stability of the CCD detector. The exception is condition 1 with high temperature and short residence time leading to varying concentration of surface defects which reduces the emission intensity between syntheses.

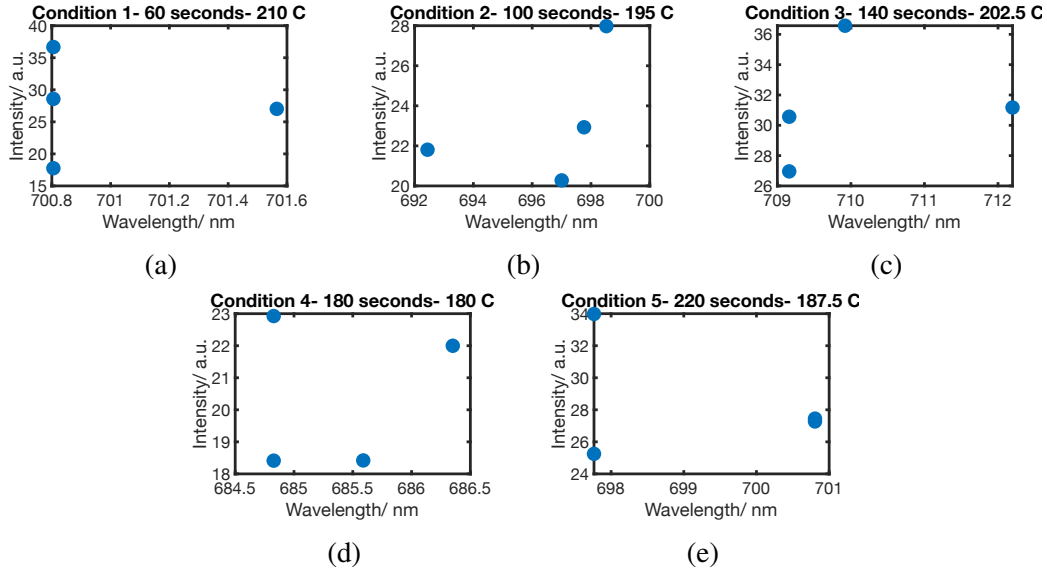

Figure 3.12: Scatter plot of wavelength and corresponding intensities in each reaction condition in experiment 2.

This data consistency is crucial for performing self-optimisation, as we require reliable intensity data that can distinguish spectroscopic behaviour between sequential syntheses. From data presented here I concluded that the

current optical detection configuration provided sufficient consistency to perform an automated self-optimising experiment. This was not case in the previous configuration, as the intensity deviations due to the spectrometer are too large.

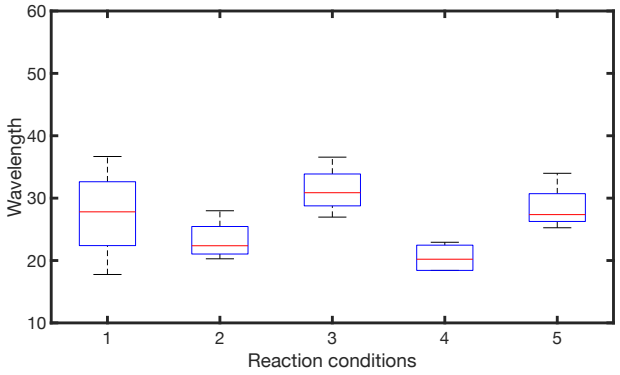

Figure 3.13: Box plot of intensity values from sampling experiment 2 with spectrometer cooling enabled. Red line is the mean value, with whiskers representing the extreme intensities in each reaction condition.

As particles grow, the surface-to-volume ratio decreases which means there are more available pathways within the particle for recombination. This in turn leads to increasing intensity, as excitons are not necessarily recombining in surface defect sites due to lack of recombination sites. Therefore, we expect larger particles to have higher intensity, which is the case here for condition 3 which yields the longest mean peak wavelength around 710 nm, and highest corresponding mean peak intensity in sampling 2. From this, we can reason that high growth rate and long reaction time leads increase in intensity in this work. Therefore, to maximise the intensity, high temperature and long reaction time are required conditions. However, the extended growth leads to undesired product aggregation as observed in both sampling experiments. This means a new parameter space is required to prevent aggregation when using the platform.

From the two sampling experiments, I defined a lower temperature range from 160 °C to 185 °C, and compensated with prolonged residence time range from 140 seconds to 360 seconds, which should avoid aggregation with the standardised precursor solution and preventing separator fouling.

3.4 Summary

In this chapter, two automated Latin Hypercube samplings were performed to map out the peak emission wavelength and emission intensity based on

temperature and residence time. A large variation in the intensity data was observed in the first sampling due to optical detection configuration. A systematic test on the spectrometer behaviour was performed and revealed the need to enable thermoelectric cooling for better consistency in the intensity measurements. The data presented in this chapter has successfully demonstrated the automated synthesis with on-line analysis by using the self-built automated synthesis platform.

From gathered data, I found the intensity dependency on the input parameters, and concluded that long residence time and high temperature is required to maximise the intensity by using standardised precursor. Additionally, I defined a new parameter space which was expected to avoid product aggregation for standardised precursor solution. On the basis of the data presented here, I proceed to carry out self-optimisation experiments with the automated platform coupled with a chemical optimisation algorithm based on SNOBFit.

CHAPTER 4

SELF-OPTIMISING SYNTHESIS OF $CuInS_2$ NANOCRYSTALS

4.1 Self-optimisation

In this chapter, we will focus on 2-dimensional unconstrained optimisation of a single parameter with reaction time and temperature as input parameters. However, SNOBFit is not limited to only 2-dimensional parameter space and a user can choose 3-dimensional or multi-dimensional parameter space to optimise. However it should be noted that more input parameters mean more evaluation points are necessary to find an optimum, which leads to increasing time and material consumption.

The parameters optimised in this work were the intensity and the emission peak wavelength.

4.2 2D Intensity Optimisation

It is necessary to define a parameter space prior to an optimisation experiment, and it is important the parameter space is defined within a region in which the system behaves reproducibility without aging or fouling. From Chapter 3, we learned that high temperature synthesis above 200 °C can easily cause unwanted aggregates. Thus, we have identified a new parameter space with lower temperature range and compensated with a slight increasing in residence time to allow sufficient particle growth. The new parameter space had a temperature range from 160 °C to 185 °C and residence time 140 seconds to 360 seconds.

By utilising SNOBFit optimisation algorithm the aim was to identify the reaction conditions within the parameter space that would maximise the emission peak intensity. Following the discussion in chapter 1, the merit function was defined as equation 1.2 ($f = 355 - I_{peak}$) with low merit value for high emission intensity.

4.2.1 Experiment 1

In this experiment,the delay from setting a condition to taking a measurement was set equal to twice the applied residence time of the current condition. The delay time was intended to allow the flow to stabilise, and to allow sufficient product to pass through the optical detection cell.

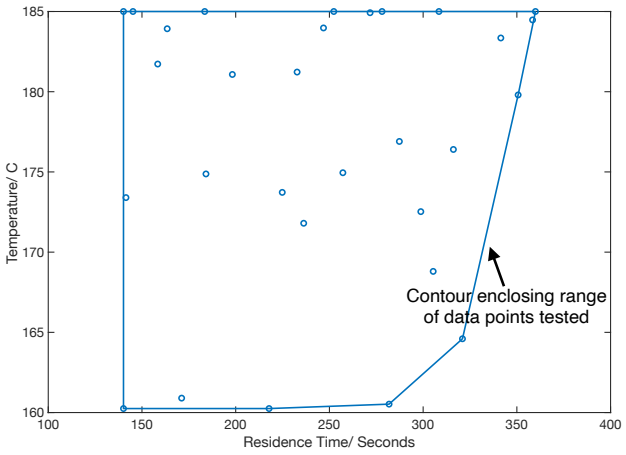

Figure 4.1: Scatter plot of 30 reaction conditions evaluated during Experiment 1. The optimisation was a 2-dimensional optimisation with varying temperature and residence time. The algorithm preferentially sampled the high temperature region that should provide higher intensity values.

The optimisation was run for 30 points, with 6 random starting points, with subsequent 6 points batches being recommended by each call to the SNOBFit algorithm. The evaluated reaction conditions recommended by SNOBFit can be seen in figure 4.1, with most points corresponding to temperatures above 170 °C, and few points below 165 °C. Hence, the algorithm preferentially sampled the higher temperature conditions, which typically provide higher intensity values as seen in the last chapter, due to increasing choices of recombination pathways.

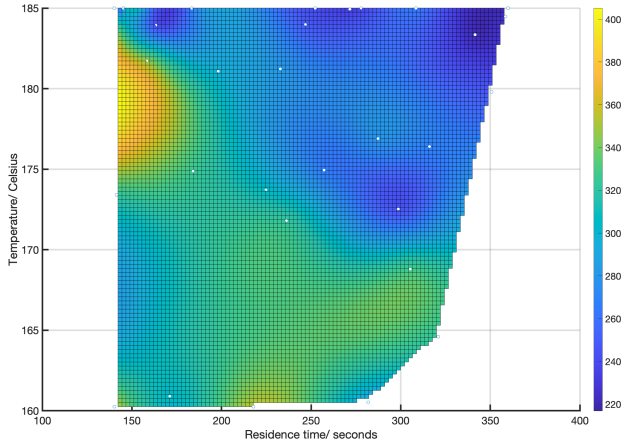

Figure 4.2: Surface fitted contour plot based on the results from optimisation experiment 1. Lower merit values correspond to higher intensities.

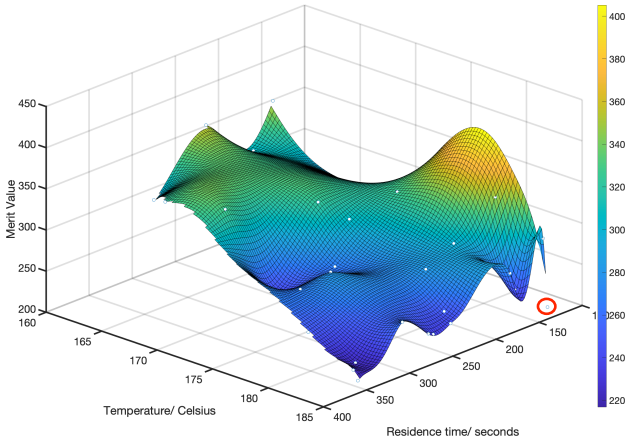

Figure 4.3: Interpolated 3D contour plot based on the results from optimisation experiment 1. The red marked point highlights the best reaction condition returned by SNOBFit based on the merit values.

The results from this experiment can be seen in figure 4.2 and 4.3. Figure 4.2 presents a contour plot of a surface fit to the results from the experiment. Here the blue colour represent low merit values, which correspond to higher intensity values as seen from equation 1.2. The anomalous bright yellow region at the upper left corner is a fitting artefact, which can also be seen figure 4.3. The existence

of such gradient is due to the applied gradient fitting method, as inconsistent datapoints can cause a varying gradient in the fitted surface, especially with few datapoints. In our case, there are only three points in the region to form this large gradient, and the one point at 158 seconds and 181 °C happens to have a higher merit value, which is the main contributor for the unexpected yellow curvature in the fitted plot. Figure 4.3 is a 3D surface fit to the results from the experiment, here the z-axis represents the calculated merit value based on the intensity results. In figure 4.3, we observe the fitted surface declines overall for higher temperatures and reaction times which gives large particles with high quantum efficiency, with several localised concave surfaces. These localised surface features represent the dark blue spots on the contour plot in figure 4.2.

This is a good representation of previously mentioned search logic with SNOBFit, as it searches both locally and other unexplored regions in the parameter space to prevent the search from becoming trapped in local minimum. From this experiment, SNOBFit returned the best reaction conditions to be at 140 seconds and 185 °C, which is interestingly against observations made from previous sampling experiment where the highest residence and temperature are often associated with large intensities.

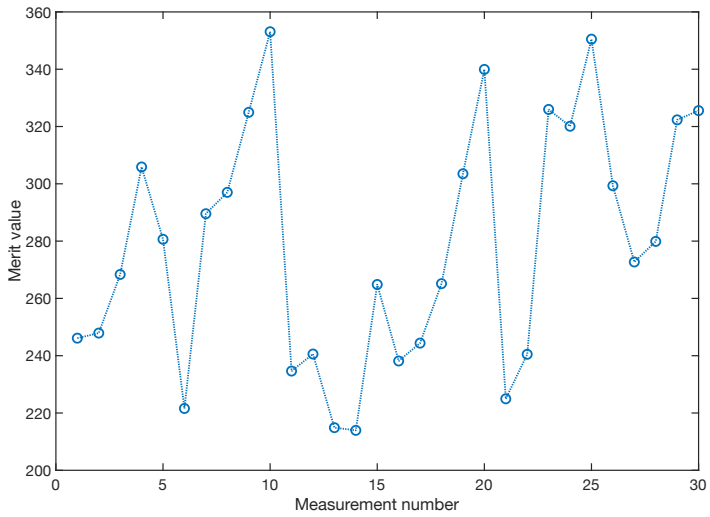

Figure 4.4: Merit values plotted against the measurement number. Here we see measurement 13 and 14 are extremely close. The reaction condition for 13 is 185 °C and 360 seconds, while for 14 the residence time is 140 seconds.

Figure 4.4 shows the merit values at each measurement, and the best conditions return by SNOBFit in this optimisation was obtained at measurement

14, which is the lowest merit value found in the experiment. However, we can see that measurement 13 has similar merit value, with reaction condition 360 seconds residence time at 185 °C. This leads to the question of what was the actual product being measured in point 14? From figure 4.1, we see that there is another datapoint with similar reaction condition to measurement 14, i.e. measurement 26, with 145 seconds at 185 °C. The merit value for this point is around 300, which is significantly higher merit value of measurement 14. Therefore, it is possible that the measurement 14 is contaminated by product from condition 13 which makes sense as the merit values are similar in the two conditions, and very different from measurement 26.

This insufficient flushing may also explain why we observe many points that lie away from. the fitted surface in figure 4.3. In order to overcome this issue, the time delay was increased from two residence time to three residence time to ensure the tube within the optical detection cell is properly flushed with new product.

Additionally, we see the merit values in figure 4.4 follows a periodic pattern and is a good representation of the global search logic by SNOBFit, that the algorithm did not explore just to one local minima, but regularly explored unknown regions that provided different merit values.

4.2.2 Experiment 2

It was found that two residence time delay was insufficient for the new product to flush through the optical detection cell in the previous experiment. Therefore, the experiment was repeated with the delay time increased to three residence times from setting a condition to taking a measurement. Additionally, the number of points per batch was decreased to four points from six points so that SNOBFit was called more often compared to previous case, which is beneficial as SNOBFit can have better use of acquired data to guide its selection of new points, potentially leading to a mapping with fewer datapoints.

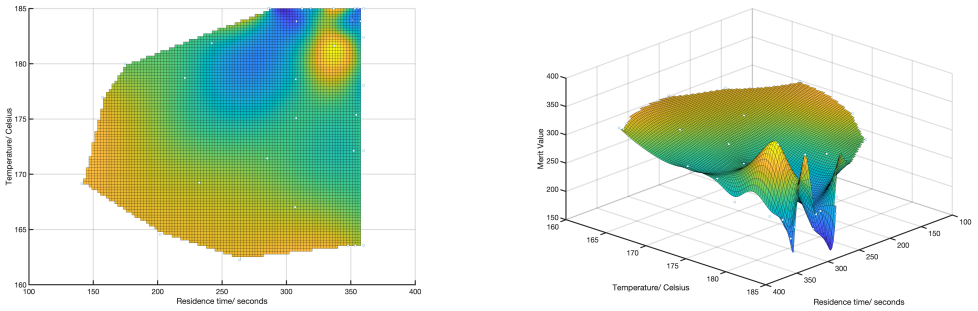

(a) (b)

Figure 4.5: Surface fitted results of Experiment 2, here we have overall smooth surface with two extreme high merit values

The optimisation was run for 32 points in 8 batches within the same parameter space. The results from the new experiment are presented in figure 4.5, which shows a smoother surface compared to figure 4.3 with fewer localised large surface gradients. The convex surfaces are due to unexpected high merit values obtained with measurements 13 and 14.

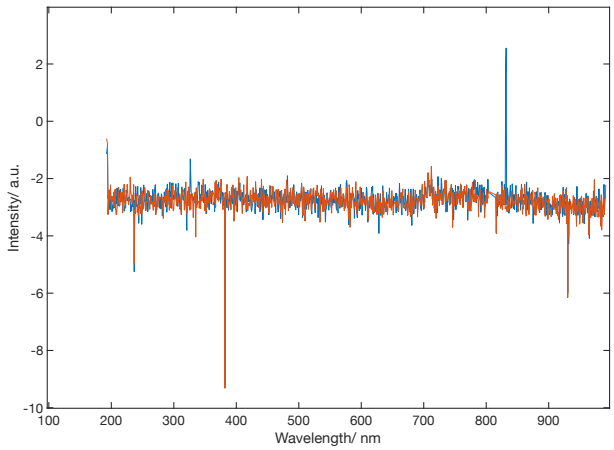

Figure 4.6: Emission spectrum from condition 13 in blue and 14 in red.

The merit values for the two measurements were found to be around 355, which essentially means no emission in these points. Figure 4.6 shows overlaid emission spectra obtained from run 13 and 14, which are totally flat, suggesting that no products were flowing through the optical detection cell during these measurements. This is likely to be caused by carrier fluid entering the product

channel in the separator. This seems to have been a ”one-off” incident, otherwise we would obtain more non-emitting peaks in the experiment.

As it was found that run 13 and 14 were unreliable, these two points were removed from the dataset, yielding the smoother surface shown in figure 4.7.

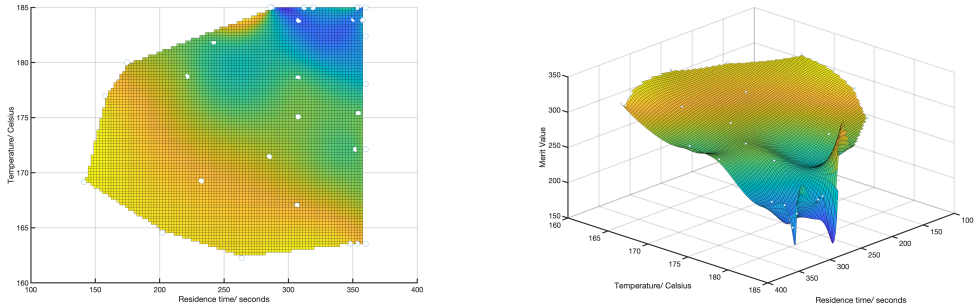

(a) (b)

Figure 4.7: Refitted surfaces excluding measurement 13 and 14. Here, we obtain an increasing consistent surface with clear gradual decline towards the blue region.

From figure 4.7a, we see a clear transition from bright yellow in the lower left corner to blue in upper right corner, which is associated with gradual increase in the intensity. This trend is consistent from our finding in the synthesis behaviour from previous chapter and indicates that increasing the delay time relative to the previous run improved data consistency. Moreover, about 1/3 of the measurements were taken around or below the orange line, which is twice as many as for last optimisation run. This suggests the increased call frequency to the SNOBFit algorithm led to a more evenly distributed mapping of the parameter space.

The global minimum was found at 355 seconds at 185 °C (measurement 27), which is close to the upper limit in the parameter space, with merit value of 190. From 4.7a, we observed that the absolute upper limit (360 s at 185 °C) was also measured and found to have a merit value of 215, which is higher than for measurement 27. However, the 5 seconds difference of in the residence time in a 6-minute synthesis is less likely to cause this product difference, and from the last chapter we found out the spectrometer has around 15% standard deviation which is the more probable cause for this observation. This spectrometer deviation also explains the regional fluctuation in blue edge region of the 3D surface in figure 4.7b, which causes surface fit to return the observed varying gradients. Apart from the fluctuating datapoints in the blue region, we have a smooth surface fitted from the obtain data that declines with increasing temperature and residence time. This suggests the new intensity optimisation experiment with 3 residence time delay by SNOBFit was able to identify the optimum condition while mapping out an

overall intensity distribution of the input parameter space.

This new experiment shows the importance to have a sufficient delay time between setting the reaction condition and testing the product to obtain consistent analysis data. In these two experiments, we were working within 100 ml syringes that contained sufficient volume to carry out a 30-point optimisation, but the goal was to perform a longer optimisation with more points. Therefore, I switched to using the refilling mechanism described in chapter 2 which made it possible to perform indefinitely long syntheses. This also allowed me to increase the delay time further to ensure the measured data were consistent to the reaction conditions.

4.2.3 Experiment 3

In this experiment, by using the refilling mechanism I increased the sampling points and extended the delay time to 4 residence times to ensure sufficiently flushed the optical detection cell with newly formed product.

The new experiment was carried out with pre-filled syringes and run for 16 points with 4 points per batch; syringes were then be refilled to a pre-set volume that corresponds to solution spent in the 16 measurements, and the process was repeated until reaching a user-defined stop point. However, due to a code error in the script, the optimisation was not continued after the first refilling session. This led to an approximately 4-hour break before it was manually restarted to continue the optimisation experiment.

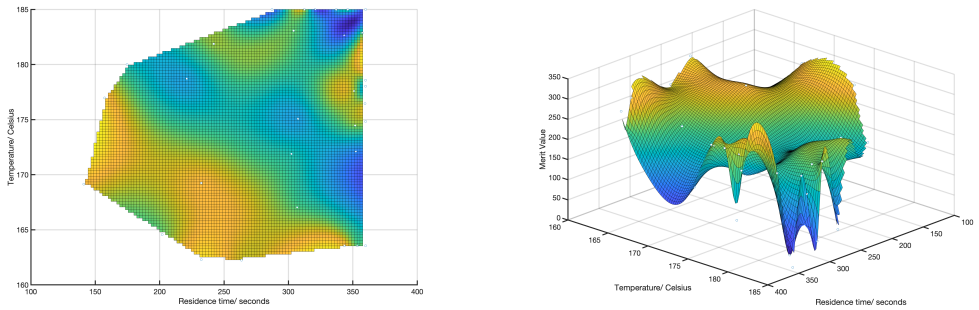

(a) (b)

Figure 4.8: Surface fitted results from optimisation experiment 3. Here, we observe large merit value variations in the same region.

The optimisation experiment was carried out for 32 measurements, with first 16 points run as one dataset, and other 16 points as the second dataset after 4-hour pause. The surface fitted results are presented in figure 4.8 by gridfit.[59] We see observe again the gradual colour transition from lower left to upper right

corner, but with many localised regions at the upper right corner similar to the first experiment but more abrupt. This varying results are rather unexpected, as we have increased delay time to ensure the sufficient products has passed to the optical detection cell for the applied condition, thus ruling out the separator as potential cause. This suggests the accidental four-hour pause might have been the cause to the data inconsistency in this optimisation routine. Figure 4.9 shows the same data into two separate surface fits, with one fit contains the dataset prior to the pause and the other one showing the data after. Figure 4.9a are fitted with the first set of datapoints prior to the refilling, and 4.9b are fitted with second dataset datapoints after restarting the optimisation run manually. Here we see that the individual datasets are smooth with clear downward slope towards the upper limit in the parameter space, which suggests that the datapoints within each dataset are self-consistent. If we were to view the entire experiment as a subset of two 16-point optimisations, we would conclude that the individual optimisations were successful with clear best reaction conditions and consistent mapping of the parameter space.

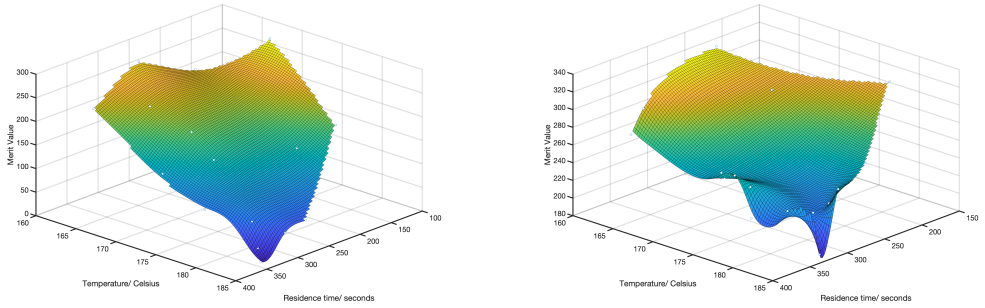

(a) (b)

Figure 4.9: Surface fit with separated datasets, a) is fitted with first batch of 16 points, and b) is fitted with second batch of 16 points.

Since the datasets are individually consistent, it is useful to examine the difference between the two datasets. Figure 4.10 shows the datapoints from the second dataset superpositioned onto surface fitted from the first dataset. The datapoints from the second set are presented as red circle markers. In figure 4.10, we see that points from second dataset are overall elevated with respect to the first dataset. implying a consistent diminished intensity. This explains observed localised gradients in figure 4.8, caused by trying to force two smooth but inconsistent planes onto a single surface.

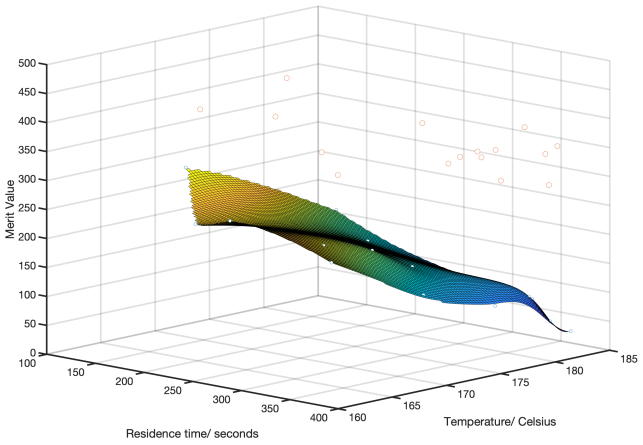

Figure 4.10: A 3D gradfit of the first dataset, with second dataset superpositioned to the fitted surface and is represented in red markers.

Possible causes of the inconsistency were considered and quickly ruled out the possibility of having accidentally knocked the optical detection system as the entire platform was untouched during the pause and restarting phase. Prior to refilling, the system was asked to perform a flushing process with carrier fluid, such no residual quantum dots were left within the system. It is unlikely but possible that the flushing procedure prior to restarting caused the system to behave differently between two syntheses experiment. However, I believe the most likely explanation for the behaviour was the spectrometer being inconsistent between two experiments. Prior to this experiment, all experiments were carried out to completion without such long breaks, therefore it was never tested whether pausing the acquisition for hours and then resuming the experiment would influence the measurement. Due to time and resource limitation in this project, I was unable to get hold of another high-end tabletop spectrometer for the system. However, I was able to establish that the spectrometer is consistent when used with short pauses between measurements of around 40 minutes, so in subsequent optimisation experiments I ensured there was no prolonged interception of the system.

Despite the data inconsistencies with restarting the experiment, SNOBFit was able to find the maximum intensity and the corresponding reaction condition to be 360 seconds residence time at 185 °C. As frequently discussed the upper limit in the parameter space that should provide the maximum intensity value. This suggests that SNOBFit global search logic can efficiently find an optimum region within a small number of searches, which makes it ideal if for searching with more variables or wider parameter space.

4.2.4 Experiment 4

During the last experiment, I observed a large offset in the measured data points when pausing the experiment for a long period due to errors in the controlling code. Therefore, I repeated the refilling experiment with a now functioning control sequence. The refilling was carried out after every 12 runs (3 batches with 4 points per batch, and took around 4 hours to complete with average 3 points per hour). It took 40 minutes to complete a refilling process. From previous experiments is was known that the spectrometer is consistent within a 40 min idle period so I expected a consistent dataset.

The new experiment was successfully carried out for 48 measurements with a 4 times delay from setting a reaction condition and taking a measurement, and took approximately 20 hours to complete the experiment. Previously, I set a flushing procedure with carrier fluid prior to refill, this was changed in this experiment to infuse precursor and carrier fluid as is done during synthesis, but the reactor was set to cold (room temperature). The purpose of the flushing step was to avoid overreaction of the precursor within the heated channel and asscoiated fouling. It was observed after the experiment that half of the product was found in the collector vessel for carrier fluid, suggesting that the separator performance had worsened over the course of the long optimisation run. It should be noted that the decreasing performance was in form of a fraction of product solution exiting the separator via side channel to carrier fluid collector. This meant there was no carrier fluid in the analysis channel and the acquired data are reliable.

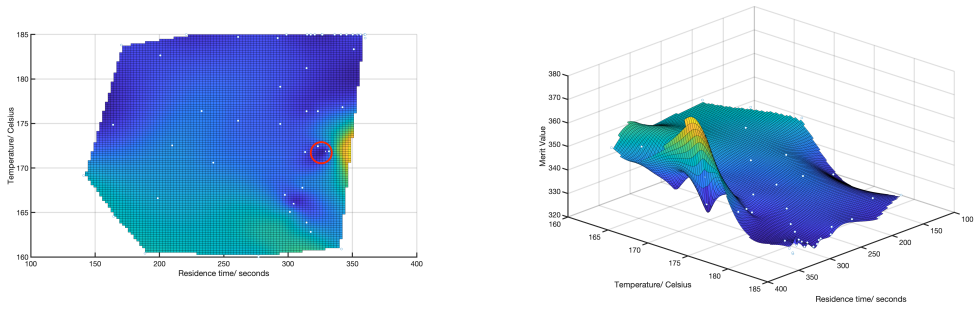

(a) (b)

Figure 4.11: Surface fitted results from optimisation experiment 4. Here, we observe overall similar diminishing trend in the merit value as previous experiments. The large local variation being investigated is around 300 seconds residence time and around 170 °C and is marked with red circle.

The results from this optimisation can be seen in figure 4.11. Consistent

merit values were now obtained throughout the 20-hour run. This indicates the spectrometer was providing consistent intensity measurements as desired. However, large local variations was again observed and is discussed below.

Figure 4.11, shows the same trend with decreasing merit values towards high temperatures and long residence times. In previous runs, I was limited by the small syringe volume, which prevented a detailed search of the parameter space. Here we can see by increased the number of measurements, not only were more datapoints obtained around boundaries (local fits), but also around the centre of the parameter space due to global searching. Figure 4.12 shows the merit values for each measurement, and we can see that the algorithm was again able to identify a minimum at measurement 10, but the merit value then fluctuated between high and low values rather than progressively diminishing. This data demonstrates the local and global search logic used by SNOBFit as previously mentioned. Each SNOBFit call evaluates previous measurements and conditions tested and generates a new batch of points that is a mixture of expected local fits around previously found promising region, and points that are to be evaluated in the unexplored regions in the parameter space where even better solutions might be found. Therefore, we obtain again a periodic rise and fall of the merit values as seen in figure 4.12.

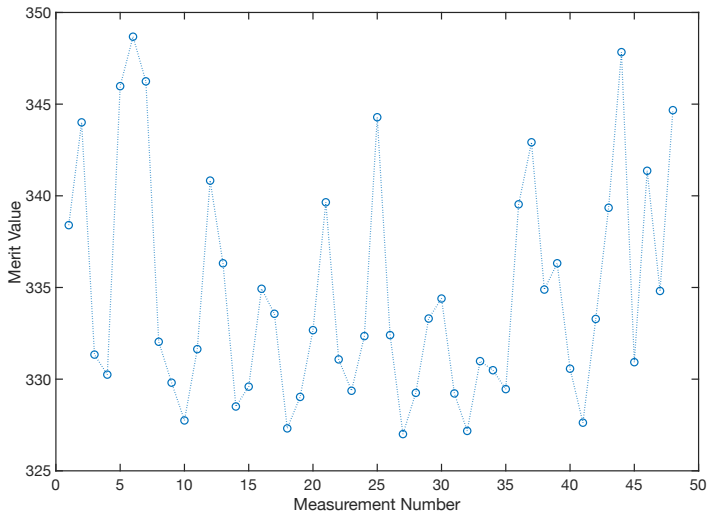

Figure 4.12: Merit values against measurement numbers in experiment 4. Again, we observe the periodic search logic represented by merit values.

From figure 4.11b, we have two very distinctive local features which are rather unusual, both features have similar residence time around 330 seconds, and

temperature around 165 and 170 °C. It is rather hard to analyse the 165 °C case as the points are quite spread in the region. Therefore we will focus the 170 °C case that is marked with a red circle, as the points are closer to each other and allows us to look into the potential cause of the strange behaviour. The measurements around the region were found to be from run 29, 33, 37, 47. From figure 4.12, we see that 29,33 and 47 have similar merit values, while 37 had an extremely high merit value suggests low fluorescing signal from the measurement, which is confirmed by the emission spectrum in figure 4.13.

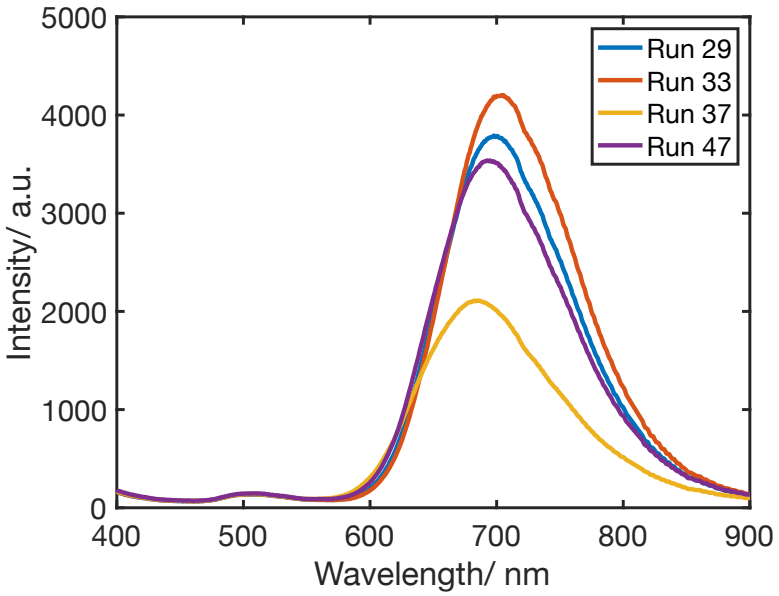

Figure 4.13: Overlaid spectra from datapoints around 330 seconds and 170 °C. Measurement number 37 exhibits extremely low emission intensity compared to other measurements in the local region.

Here we observe the peak intensity for run 37 is approximately half of the other conditions, which is unexpected as they have similar conditions. The syringes were refilled after every 12 measurements, which means run 37 was the first point after the refilling process. It was programmed such that prior and after refilling, the system would push through approximately 1 ml of each fluid into the reaction channel to restabilises the droplet formation and liquid separation. It was expected this would leave the optical detection cell filled with unreacted precursor solution, and as the reaction proceeds, more product would flow into the optical detection cell and homogenise the solution within and push it out to the collector vessel. As mentioned in the beginning of this section, there was a substantial reduction in product collected in the collector vessel, suggesting the

separator performance was impaired by extensive usage. The potential cause for run 37 to have low intensity could therefore be that the product flowing through the straight channel towards optical detection cell was insufficient to flush out the unreacted precursor. This due to the leakage to the side-channel would led to a diluted sample which in turn would reduce the intensity in the emission spectrum as seen here in measurement 37.

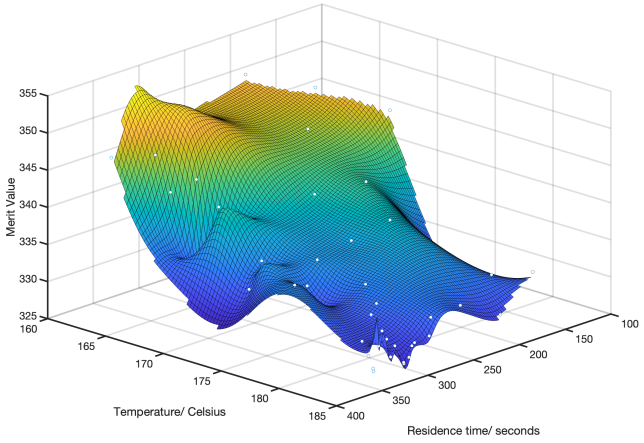

Figure 4.14: Refitted surface excluding measurement 37. Here we see an increasing consistency in the data trend that declines towards high temperatures and reaction times.

Since measurement 37 had an anomalously low intensity with respect to its condition, it is therefore interesting to analyse the surface fit again, excluding run 37 from the dataset. Here in figure 4.14, we see the refitted surface. similar but more distinctive downwards trend in the merit value towards upper boundaries compared to figure 4.11b.

Despite the anomalies and noisy datapoints, SNOBFit was able to identify the optimum region and carry out local fits, with lowest merit value that corresponds to 326 seconds at 185 °C in reaction condition at measurement 27. This is slightly different from our previous findings but within the margins of errors and can be accounted to the intensity fluctuations in the spectrometer as previously discussed. By having around 15% standard deviation in the measured intensities, we can conclude that our spectrometer is sufficient to identify an optimum region, but might struggle with finding a maximum intensity value in the region in a reproducible manner due to this fluctuating behaviour. However, I showed previously that the wavelength measurements from the spectrometer did not have the same fluctuation issue and consistent peak wavelengths were obtained for

identical conditions. Therefore, I decided to carry out a targeted wavelength optimisation to test whether the platform coupled with SNOBFit could find the conditions needed to achieve a specific peak wavelength. This test is crucial for any subsequent constrained optimisation, where we want to fix the peak wavelength within a certain range, while maximising the emission intensity.

4.3 Wavelength Optimisation

From the intensity optimisation experiments, I was able to identify an optimum region in the parameter space with high emission intensities by performing unconstrained 2-dimensional optimisation with SNOBFit and the automated platform, but it was not possible to identify the exact point in a reproducible fashion due to the fluctuating measurements by the spectrometer. From the data presented in the previous chapter, it is clear that the peak wavelength returned by the spectrometer is very consistent, so I tried a wavelength optimisation to validate the SNOBFit's ability to actively search for a target wavelength.

The merit function used here was: $f = (W_c - 675)^2$ as discussed in the introduction. This merit function is a parabolic function that equals zero when the target wavelength at 675 nm is achieved.

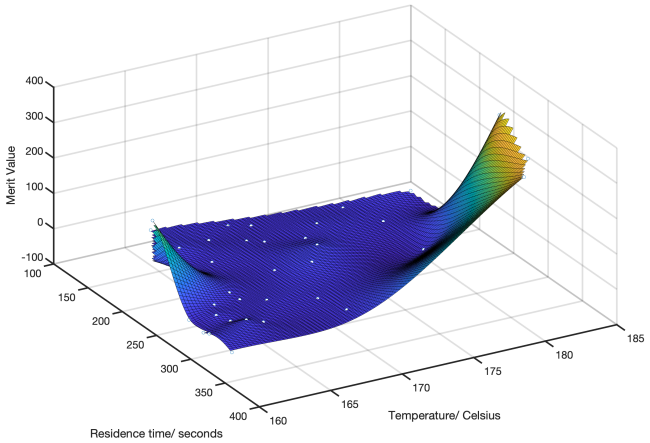

Figure 4.15: Surface fitted results from wavelength optimisation at a targeted wavelength at 675 nm. Here we see an extremely high gradient that is made up by few points at upper parameter limits. Rest of the points are spread in lower temperature region.

The target wavelength for this optimisation was set to 675 nm and the system was set to carry out 37 measurements with two refilling procedures. The capillary

tube within the separator was not changed from the last experiment, and it was observed that there was very little product in the collector vessel downstream of the optical detection channel which again indicates impaired separator performance. The SNOBFit algorithm was able to identify the condition with peak wavelength at 675 nm as targeted, with the conditions: 310 seconds residence time and 162.3 °C. The surface fit from results of the wavelength optimisation can be seen in figure 4.15, with a large declining gradient from the upper right towards lower left corner. Here the yellow regions represent high merit values that corresponds to large deviations from the target wavelength. We observe that SNOBFit was able to identify the unfavourable region with few datapoints (here 3 points at the yellow boundary) and tries to avoid the region with large merit values. As the optimisation used simple parameter space with only 2 dimensions, SNOBFit could quickly move towards the blue region which provides much smaller merit values. The large merit values dominated the plot in figure 4.15 and obscure low merit value. A new fit to the data excluding those three datapoints in shown in figure 4.16.

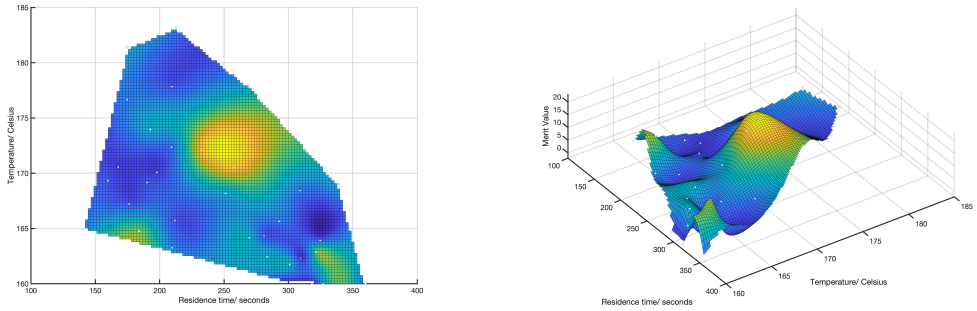

(a) (b)

Figure 4.16: Refitted surface without the three extreme measurements. Here we can see the features at the lower temperature region that was previously dominated by the large gradient at upper boundaries.

In the refitted surface, we observe the datapoints are spread from the lower right corner around 330 seconds and 165 °C region gradually towards the left side of the parameter space around 170 seconds, 170 °C region. We can also see a yellow dome at 250 s and 174 °C region that is made up by two datapoints. From the surface features, we see that the dome represents relatively large deviation from the target wavelength (with high associated merit values), which led SNOBFit to carefully sample around the dome to avoid any undesired high merit value. This sampling method coupled the previously observed large merit value in the high boundaries is a good indicator that the optimisation experiment

was carried out as desired to sample regions for a target peak wavelength and avoided large wavelength deviations.

From figure 4.16a, it is evident that the datapoints are distributed over a broad parameter space but are concentrated at two dark blue regions that were more frequently sampled. These two dark blue regions represent low merit values and are subjected to local fits which returned close matching wavelengths to the target. These two local fits match with the observation in the last chapter, where long residence time and low temperature can be compensated with a higher temperature and shorter residence time to match the peak wavelength. This is due to the emission wavelengths being size dependent, which in turn depends on the growth rate that are proportional to the temperature. The merit values against the measurement number are presented below in figure 4.17. Here we see four large merit values, with three of them having approximately the same value and corresponds to the three datapoints on the yellow boundary in figure 4.15. Due these large merit values, SNOBFit was able to converge rapidly towards the target peak wavelength as the subsequent points had by comparison low merit values.

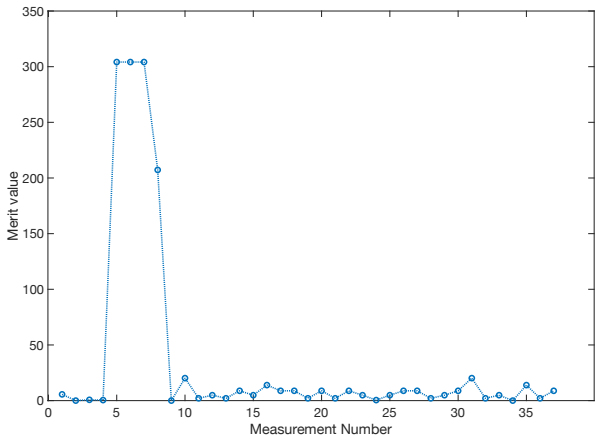

Figure 4.17: Merit values against the measurement number. Here we see four large merit values that corresponds upper parameter range and small merit values suggesting the overall measurements are close to the target peak wavelength.

This small merit value variation suggests that the obtain peak wavelength from these conditions are similar, however, it was known from previous optimisations that the separator drops its performance which leads to lesser volume passing through to the optical cell by increasing usage. Therefore, it was important to check the raw data, to ensure the products measured are not identical to each other in terms of intensity. It is known that different reaction conditions can have similar emission peak, but the emission intensity differs greatly based on the reaction time

due to surface passivation.

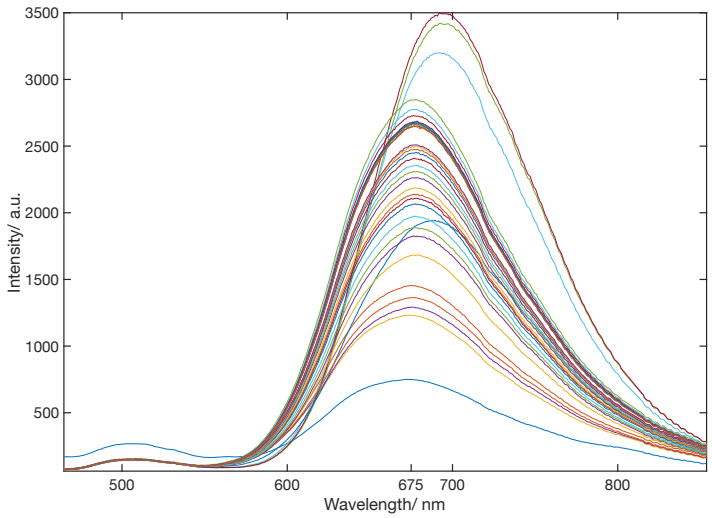

Figure 4.18: Overlaid spectra measured during targeted wavelength optimisation experiment at 675 nm. Here we see most of the spectrum have emission peak around 675 nm, close to the target value. However, the intensities varies depending on the exact reaction conditions.

The full emission spectra from the optimisation experiment are presented in figure 4.18, here it can be seen the peak wavelength lies mainly around 675 nm, with 4 spectra having a large offset which corresponds to the 4 points with comparatively extremely high merit values as shown in figure 4.17. Furthermore, we observe varying emission intensities despite similar emission wavelength in figure 4.18. This suggests the data is consistent with respect to the conditions, otherwise the emission intensities would be similar in values, and therefore eases our concern regarding the separator causing data inconsistency despite performance drop.

The spectral data from figure 4.18 shows also the possibility of performing constrained optimisation, where we can maximise the intensity within a wavelength interval. Here, the peak wavelengths are within few nanometres difference, while the intensities are ranging from 750 to 2900, which is approximate 4-fold increase. However, due to the time limitation, constrained optimisation was not performed in this work.

4.4 Summary

In this chapter, I have carried out multiple unconstrained optimisations with different objective functions by using the automated platform with the SNOBFit global minimum search algorithm. The system was able to identify an optimum region in the parameter space that returned desired high emission intensities in intensity optimisation, and reaction conditions that generate target peak wavelength at 675 nm during wavelength optimisation. The optimisation experiments also demonstrated the global search logic of SNOBFit optimisation algorithm which is suitable for performing a black-box chemical optimisation algorithm.

During the intensity observation, it became apparent that a long break (many hours) between two measurements can lead to inconsistent intensity measurements, while short idle period provides consistent intensity measurements. It was also found that a long delay time of at least four residence timesis need before taking a measurement in order to make sure the measured datapoints are consistent to the set conditions. Additionally, it was found that the separator performance gradually worsened with increasing usage, suggesting the need to liquid combination.

CHAPTER 5

CONCLUSION AND FURTHER WORK

5.1 Conclusion

In this thesis I have described work on the development of an automated self-optimisation synthesis platform for nanocrystals, using flow reactor technology. This was carried out to take advantage of more the uniform and controllable reaction conditions available in flow compared to conventional batch synthesis, as well as the reduced materials consumption and better time efficiency associated with testing multiple reaction conditions sequentially in flow.

The work undertaken in this project included construction of a solid-state heater and optical detection system, as well utilisation of other flow components such as motorised flow valves and an automated separator to complete the platform design. Two syringe pumps were used to deliver the reagents and carrier fluid PTFE reaction channel through a Y-shaped droplet generator that created an alternating flow pattern of the two liquids to minimise fouling. The self-built solid-state heater with high accuracy allowed the user to change the temperature rapidly as well as maintain constant temperature and is suitable for temperature sensitive syntheses. By incorporating motorised valves that alternately connected the syringes to a reservoir or the flow reactor implemented automatic syringe refilling to allow an indefinite number of reaction conditions to be tested. The optical detection system was able to excite the produced nanocrystals and measure the emission properties in real time and feed the result as a spectrum back to a PC for analysis. An automated separator was used to separate the two-phase flow in the reaction channel into separated continuous-flow of each phase and increase the reliability in the optical measurement. Each component was interfaced with a PC to realise the automated synthesis by executing a command script that called each component in a user-defined sequence.

The synthesis of $CuInS_2$ nanocrystals was chosen as an example of a reaction to demonstrate the adaption process and possibility to perform optimisation with competing emission properties. Experiments were carried out in batch to familiarise with the reaction parameters as well as to optimise the precursor

solution for flow synthesis. Additionally, two different types of high temperature tolerant carrier fluids were tested to determine their suitability for use in this platform, with the conclusion being that the low viscosity carrier fluid was the better choice.

When the adaptation process was completed, automated randomised sampling experiments were carried out to investigate the effect of the reaction conditions on the product as well as the reproducibility of the platform by repeating the sampling sequence several times. The results showed highly reproducible products were formed for each specific set of reaction conditions and demonstrated reproducibility needed to be able to carry out nanocrystal synthesis on the automated platform. The sampling experiments indicated that longer reaction times often led to higher emission intensity due to the increasing surface passivation during the synthesis.

Testing revealed substantial variation in intensity measurements due to the spectrometer which could be partially but not completely solved by cooling the detector. The final resulted show a 15% fluctuation in the intensity measurement, which is tolerable for demonstration purposes in an intensity optimisation.

It was observed that undesired aggregates were formed in multiple reaction conditions with high temperatures. This aggregation behaviour led to undesired rapid fouling in the separator. Therefore, a new parameter space was chosen to avoid aggregations during optimisation experiments.

Based on the results from the parameter space sampling, a series of automated intensity optimisations were carried out by utilising the platform coupled with a custom version of SNOBFit algorithm intended for black box chemical optimisation by Walker*et al.*[45] The objective was to maximise the emission intensity within a specified parameter space. The algorithm was able to repeatedly identify same optimum region of the parameter space that yielded high intensity value as intended. However it struggled to reproduce the best reaction condition due to the spectrometer measurement variation. Nonetheless, it demonstrated the ability to perform an optimising reaction condition search without having previous knowledge about the property distribution with the platform and an optimisation algorithm.

Significant spectrometer inconsistency was observed during an optimisation experiment with a long break between two small sessions suggesting the spectrometer might be inconsistent upon restart. For small refilling breaks, the spectrometer data remained consistent as expected.

Furthermore, an unconstrained wavelength optimisation was carried out as I had previously shown that consistent wavelengths could be obtained for the same reaction conditions from the sampling experiments. The results showed SNOBFit was able to identify an optimum reaction condition that gives the desired target peak wavelength while performed global search to find other similar results. The

majority of the conditions searched were very close to the target wavelength with varying intensities. This suggests one can straightforwardly carry out 2-dimensional constrained optimisation, such as optimising intensity at a fixed wavelength.

5.2 Further Work

The optimisations in this work mainly focused on unconstrained optimisation of a single property due to time limitations. However, this work provides the necessary foundation to process to a two-dimensional constrained optimisation. In constrained optimisation, it would be interesting to optimise the emission intensity while constraining the peak wavelength to lie within certain bounds. Once constrained optimisation with temperature and residence time is carried out, other interesting optimisations could be attempted involving for instance the control of the emission linewidth.

The parameters varied during the optimisations experiments were temperature and residence time. However, precursor stoichiometric variations were untested, which it could be interesting to carry out to test how ratios between precursors can influence the product emission features. This includes dividing up the precursor (Copper and Indium), such one can control each flow rate and mix the solution prior to the droplet flow generator. This would result in a more complex three-dimensional optimisation problem for SNOBFit to solve, where the varying parameters are temperature, wavelength and precursor ratio.

After the progressing to 3D optimisation, it would be also interesting to carry out constrained optimisation in for more sophisticated control over product properties.

Additionally, we know the spectrometer has an intensity variation of around 15%, which prevents reliable intensity optimisation as its unable to produce reproducible intensity measurements. Hence there is a need to test out other spectrometers that do not have the same problem.

Moreover, we observed the separator performance dropped with extensive usage, ausing products exit through the carrier fluid channeo. This observation might be limited to this current liquid combination in this work but is an interesting investigation to find out if the problem could be solved by using other liquid combinations or by changing to a different porous capillary.

BIBLIOGRAPHY

[1] Andrew J Harvie, Jack O Herrington, and John C deMello. An improved liquid–liquid separator based on an optically monitored porous capillary. *Reaction Chemistry & Engineering*, 4(9):1579–1588, 2019.

[2] George Lisensky, Ross McFarland-Porter, Weltha Paquin, and Kangying Liu. Synthesis and Analysis of Zinc Copper Indium Sulfide Quantum Dot Nanoparticles. *Journal of Chemical Education*, 97(3):806–812, 2020.

[3] Hong Bai Chin and Chang Dae Han. Studies on droplet deformation and breakup. ii. breakup of a droplet in nonuniform shear flow. *Journal of Rheology*, 24(1):1–37, 1980.

[4] GK Seevaratnam, H Ding, O Michel, JYY Heng, and OK Matar. Laminar flow deformation of a droplet adhering to a wall in a channel. *Chemical engineering science*, 65(16):4523–4534, 2010.

[5] Kelly Sooklal, Leo H. Hanus, Harry J. Ploehn, and Catherine J. Murphy. A blue-emitting cds/dendrimer nanocomposite. *Advanced Materials*, 10(14):1083–1087, 1998.

[6] Aoneng Cao, Zhen Liu, Saisai Chu, Minghong Wu, Zhangmei Ye, Zhengwei Cai, Yanli Chang, Shufeng Wang, Qihuang Gong, and Yuanfang Liu. A facile one-step method to produce graphene–cds quantum dot nanocomposites as promising optoelectronic materials. *Advanced materials*, 22(1):103–106, 2010.

[7] Igor L Medintz, H Tetsuo Uyeda, Ellen R Goldman, and Hedi Mattoussi. Quantum dot bioconjugates for imaging, labelling and sensing. *Nature Materials*, 4(6):435–446, 2005.

[8] Yunqing Wang and Lingxin Chen. Quantum dots, lighting up the research and development of nanomedicine. *Nanomedicine: Nanotechnology, Biology and Medicine*, 7(4):385–402, 2011.

[9] Eunjoo Jang, Shinae Jun, Hyosook Jang, Jungeun Lim, Byungki Kim, and Younghwan Kim. White-light-emitting diodes with quantum dot color

converters for display backlights. *Advanced Materials*, 22(28):3076–3080, 2010.

[10] Hedi Mattoussi, M. Kenneth Kuno, Ellen R. Goldman, George P. Anderson, and J. Matthew Mauro. Chapter 17 - colloidal semiconductor quantum dot conjugates in biosensing. In Frances S. Ligler and Chris A. Rowe Taitt, editors, *Optical Biosensors*, pages 537–569. Elsevier Science, Amsterdam, 2002.

[11] Austin M Derfus, Warren CW Chan, and Sangeeta N Bhatia. Probing the cytotoxicity of semiconductor quantum dots. *Nano letters*, 4(1):11–18, 2004.

[12] Françisco M Raymo and Ibrahim Yildiz. Luminescent chemosensors based on semiconductor quantum dots. *Physical chemistry chemical physics*, 9(17):2036–2043, 2007.

[13] Ronit Freeman and Itamar Willner. Optical molecular sensing with semiconductor quantum dots (qds). *Chem. Soc. Rev.*, 41:4067–4085, 2012.

[14] Anusorn Kongkanand, Kevin Tvrdy, Kensuke Takechi, Masaru Kuno, and Prashant V. Kamat. Quantum dot solar cells. tuning photoresponse through size and shape control of cdse/tio2 architecture. *Journal of the American Chemical Society*, 130(12):4007–4015, 2008. PMID: 18311974.

[15] Pralay K. Santra, Pratheesh V. Nair, K. George Thomas, and Prashant V. Kamat. CuInS2-sensitized quantum dot solar cell. electrophoretic deposition, excited-state dynamics, and photovoltaic performance. *Journal of Physical Chemistry Letters*, 4(5):722–729, 2013.

[16] Alireza Valizadeh, Haleh Mikaeili, Mohammad Samiei, Samad Mussa Farkhani, Nosratalah Zarghami, Abolfazl Akbarzadeh, Soodabeh Davaran, et al. Quantum dots: synthesis, bioapplications, and toxicity. *Nanoscale research letters*, 7(1):1–14, 2012.

[17] Liang Li, Anshu Pandey, Donald J. Werder, Bishnu P. Khanal, Jeffrey M. Pietryga, and Victor I. Klimov. Efficient synthesis of highly luminescent copper indium sulfide-based core/shell nanocrystals with surprisingly long-lived emission. *Journal of the American Chemical Society*, 133(5):1176–1179, 2011.

[18] Ziping Liu, Qiang Ma, Xinyan Wang, Zihan Lin, Hao Zhang, Linlin Liu, and Xingguang Su. A novel fluorescent nanosensor for detection of heparin and heparinase based on cuins2 quantum dots. *Biosensors and Bioelectronics*, 54:617–622, 2014.

[19] Niko Hildebrandt, Christopher M. Spillmann, W. Russ Algar, Thomas Pons, Michael H. Stewart, Eunkeu Oh, Kimihiro Susumu, Sebastian A. Díaz, James B. Delehanty, and Igor L. Medintz. Energy transfer with semiconductor quantum dot bioconjugates: A versatile platform for biosensing, energy harvesting, and other developing applications. *Chemical Reviews*, 117(2):536–711, 2017. PMID: 27359326.

[20] Charles Kittel. *Introduction to Solid State Physics*. Wiley, 8 edition, 2004.

[21] B.H. Bransden and C.J. Joachain. *Quantum mechanics*. Prentice Hally, 2nd edition, 2000.

[22] Sergey V Gaponenko. *Introduction to nanophotonics*. Cambridge University Press, 2010.

[23] Andrew J. Harvie, Matthew Booth, Ruth L. Chantry, Nicole Hondow, Demie M. Kepaptsoglou, Quentin M. Ramasse, Stephen D. Evans, and Kevin Critchley. Observation of compositional domains within individual copper indium sulfide quantum dots. *Nanoscale*, 8(36):16157–16161, 2016.

[24] Huidong Zang, Hongbo Li, Nikolay S. Makarov, Kirill A. Velizhanin, Kaifeng Wu, Young Shin Park, and Victor I. Klimov. Thick-Shell CuInS2/ZnS Quantum Dots with Suppressed "Blinking" and Narrow Single-Particle Emission Line Widths. *Nano Letters*, 17(3):1787–1795, 2017.

[25] Artjay Javier, Donny Magana, Travis Jennings, and Geoffrey F Strouse. Nanosecond exciton recombination dynamics in colloidal cdse quantum dots under ambient conditions. *Applied physics letters*, 83(7):1423–1425, 2003.

[26] T Berstermann, T Auer, H Kurtze, M Schwab, DR Yakovlev, M Bayer, J Wiersig, C Gies, F Jahnke, D Reuter, et al. Systematic study of carrier correlations in the electron-hole recombination dynamics of quantum dots. *Physical Review B*, 76(16):165318, 2007.

[27] Yasushi Hamanaka, Tetsuya Ogawa, Masakazu Tsuzuki, and Toshihiro Kuzuya. Photoluminescence properties and its origin of agins2 quantum dots with chalcopyrite structure. *The Journal of Physical Chemistry C*, 115(5):1786–1792, 2011.

[28] Addis S. Fuhr, Hyeong Jin Yun, Nikolay S. Makarov, Hongbo Li, Hunter McDaniel, and Victor I. Klimov. Light Emission Mechanisms in CuInS2 Quantum Dots Evaluated by Spectral Electrochemistry. *ACS Photonics*, 4(10):2425–2435, 2017.

[29] Masaru Kuno, Jong-Keuk Lee, Bashir O Dabbousi, Frederic V Mikulec, and Moungi G Bawendi. The band edge luminescence of surface modified cdse nanocrystallites: Probing the luminescing state. *The Journal of Chemical Physics*, 106(23):9869–9882, 1997.

[30] WH Qi, MP Wang, and QH Liu. Shape factor of nonspherical nanoparticles. *Journal of materials science*, 40(9-10):2737–2739, 2005.

[31] Jaehyun Park and Sang Wook Kim. CuInS2/ZnS core/shell quantum dots by cation exchange and their blue-shifted photoluminescence. *Journal of Materials Chemistry*, 21(11):3745–3750, 2011.

[32] Margaret A Hines and Philippe Guyot-Sionnest. Synthesis and characterization of strongly luminescing zns-capped cdse nanocrystals. *The Journal of Physical Chemistry*, 100(2):468–471, 1996.

[33] Ingvar T Kraatz, Matthew Booth, Benjamin J Whitaker, Michael GD Nix, and Kevin Critchley. Sub-bandgap emission and intraband defect-related excited-state dynamics in colloidal cuins2/zns quantum dots revealed by femtosecond pump–dump–probe spectroscopy. *The Journal of Physical Chemistry C*, 118(41):24102–24109, 2014.

[34] Chintamani Nagesa Ramachandra Rao, Achim Müller, and Anthony K Cheetham. *The chemistry of nanomaterials: synthesis, properties and applications*. John Wiley & Sons, 2006.

[35] Alan S Edelstein and RC Cammaratra. *Nanomaterials: synthesis, properties and applications*. CRC press, 1998.

[36] Guozhong Cao. *Nanostructures and Nanomaterials: Synthesis,Properties and Applications*. Imperial College Press, 1st edition, 2004.

[37] Klaus Jähnisch, Volker Hessel, Holger Löwe, and Manfred Baerns. Chemistry in microstructured reactors. *Angewandte Chemie International Edition*, 43(4):406–446, 2004.

[38] E Bruce Nauman. *Chemical reactor design, optimization, and scaleup*. John Wiley & Sons, 2008.

[39] James H. Bannock, Siva H. Krishnadasan, Martin Heeney, and John C. De Mello. A gentle introduction to the noble art of flow chemistry. *Materials Horizons*, 1(4):373–378, 2014.

[40] Yong Kweon Suh and Sangmo Kang. A review on mixing in microfluidics. *Micromachines*, 1(3):82–111, 2010.

[41] Lorenzo Capretto, Wei Cheng, Martyn Hill, and Xunli Zhang. Micromixing within microfluidic devices. *Microfluidics*, pages 27–68, 2011.

[42] Matthew B. Plutschack, Bartholomäus Pieber, Kerry Gilmore, and Peter H. Seeberger. The Hitchhiker's Guide to Flow Chemistry â¥. *Chemical Reviews*, 117(18):11796–11893, 2017.

[43] Thomas W. Phillips, Ioannis G. Lignos, Richard M. Maceiczyk, Andrew J. Demello, and John C. Demello. Nanocrystal synthesis in microfluidic reactors: Where next? *Lab on a Chip*, 14(17):3172–3180, 2014.

[44] Adrian M. Nightingale, James H. Bannock, Siva H. Krishnadasan, Flannan T.F. O'Mahony, Saif A. Haque, Jeremy Sloan, Chris Drury, Robert McIntyre, and John C. Demello. Large-scale synthesis of nanocrystals in a multichannel droplet reactor. *Journal of Materials Chemistry A*, 1(12):4067–4076, 2013.

[45] Barnaby E. Walker, James H. Bannock, Adrian M. Nightingale, and John C. Demello. Tuning reaction products by constrained optimisation. *Reaction Chemistry and Engineering*, 2(5):785–798, 2017.

[46] S. Krishnadasan, R. J.C. Brown, A. J. DeMello, and J. C. DeMello. Intelligent routes to the controlled synthesis of nanoparticles. *Lab on a Chip*, 7(11):1434–1441, 2007.

[47] CH Faham, VM Gehman, A Currie, A Dobi, P Sorensen, and RJ Gaitskell. Measurements of wavelength-dependent double photoelectron emission from single photons in vuv-sensitive photomultiplier tubes. *Journal of Instrumentation*, 10(09):P09010, 2015.

[48] Arthur B Shafer, Lawrence R Megill, and Leann Droppleman. Optimization of the czerny–turner spectrometer. *JOSA*, 54(7):879–887, 1964.

[49] George Zonios. Noise and stray light characterization of a compact ccd spectrophotometer used in biomedical applications. *Applied optics*, 49(2):163–169, 2010.

[50] PWJM Boumans and G Brouwer. Studies of photodiodes and phototransistors as detection devices for multichannel emission spectrometry. *Spectrochimica Acta Part B: Atomic Spectroscopy*, 27(6):247–255, 1972.

[51] Liang Li, T. Jean Daou, Isabelle Texier, Tran Thi Kim Chi, Nguyen Quang Liem, and Peter Reiss. Highly luminescent cuins 2/ZnS Core/Shell

nanocrystals: Cadmium-free quantum dots for in vivo imaging. *Chemistry of Materials*, 21(12):2422–2429, 2009.

[52] Thomas J Macdonald, Yatin J Mange, Melissa Dewi, Aoife McFadden, William M Skinner, and Thomas Nann. Cation exchange of aqueous cuins 2 quantum dots. *CrystEngComm*, 16(40):9455–9460, 2014.

[53] Sungjee Kim, Yong Taik Lim, Edward G Soltesz, Alec M De Grand, Jaihyoung Lee, Akira Nakayama, J Anthony Parker, Tomislav Mihaljevic, Rita G Laurence, Delphine M Dor, et al. Near-infrared fluorescent type ii quantum dots for sentinel lymph node mapping. *Nature biotechnology*, 22(1):93–97, 2004.

[54] Alexandra Yashina, Ioannis Lignos, Stavros Stavrakis, Jaebum Choo, and Andrew J. DeMello. Scalable production of CuInS 2 /ZnS quantum dots in a two-step droplet-based microfluidic platform. *Journal of Materials Chemistry C*, 4(26):6401–6408, 2016.

[55] Thomas Cubaud and Thomas G Mason. Capillary threads and viscous droplets in square microchannels. *Physics of fluids*, 20(5):053302, 2008.

[56] Stefano Guido and Valentina Preziosi. Droplet deformation under confined poiseuille flow. *Advances in colloid and interface science*, 161(1-2):89–101, 2010.

[57] Santanu Manna, Huiying Huang, Saimon Filipe Covre da Silva, Christian Schimpf, Michele B Rota, Barbara Lehner, Marcus Reindl, Rinaldo Trotta, and Armando Rastelli. Surface passivation and oxide encapsulation to improve optical properties of a single gaas quantum dot close to the surface. *Applied Surface Science*, 532:147360, 2020.

[58] Kusum Kumari, Umesh Kumar, Shailesh N Sharma, Suresh Chand, Rita Kakkar, VD Vankar, and Vikram Kumar. Effect of surface passivating ligand on structural and optoelectronic properties of polymer: Cdse quantum dot composites. *Journal of Physics D: Applied Physics*, 41(23):235409, 2008.

[59] John D'Errico. Surface fitting using gridfit - file exchange - matlab central.

APPENDIX A

MICROCONTROLLER CODE FOR CONTROL THE AUTOMATED REACTOR COMPONENTS

Code for Heater:

Following is the microcontroller code for the heater written by Dr.Andrew Harvie and modified by the author.

```
/*Pins
 * GND-VCC given 3.3 V
 * CS - 15
 * SCK - 14
 * SO - 12
 * Fan MOSFET is on pin 16
 * Heater MOSFET is on 13 (so it lights up)
 */

#include <PID_v1.h>
#include <SPI.h>

//PID values for coarse and fine adjustments
double coarseP = 100;
double coarseI = 15;
double coarseD = 5;
//Kp=300, KI=20. KD=0.6
//Kp=20, Ki=0.5 Kd=5

double fineP = 20;
double fineI = 5;
double fineD = 5;

// Window in celsius around set point where fine adjustments are
    made

double fineWindow = 0;


```

```
29 double currTemp;
30 double setPoint;
31 double heaterPower;
32 int windowSize = 1000; //one PID window in ms
33
34 bool fanOn = false;
35
36 const byte numChars = 32;
37 char receivedChars[numChars];
38
39 //PID controller and parameters
40 PID myPID(&currTemp, &heaterPower, &setPoint, coarseP, coarseI,
       coarseD, DIRECT);
41
42
43 void setup() {
44   pinMode(15,OUTPUT);
45   pinMode(13,OUTPUT);
46   //fan control pin
47   pinMode(16,OUTPUT);
48   myPID.SetOutputLimits(0, windowSize);
49   myPID.SetMode(AUTOMATIC);
50   SPI.setSCK(14); //default is 13
51   SPI.begin();
52 }
53
54 void loop() {
55   digitalWrite(15, HIGH);
56
57   getSetPoint();  // Get set point from serial (if it's changed)
58   setPoint = double(atof(receivedChars));
59   currTemp = getTemp(); //record current temp
60   myPID.Compute();
61
62
63   myPID.SetTunings(coarseP, coarseI, coarseD);
64
65   heater(); //do heating
66
67   //turn fan on if temperature near setpoint
68   if (currTemp > setPoint - 10) {
69     digitalWrite(16, HIGH);
70     fanOn = true;
71   }
72   else {
73     digitalWrite(16, LOW);
74     fanOn = false;
75   }
76
```

```
77    //monitoring
78    Serial.print(setPoint);
79    Serial.print(" ");
80    Serial.println(currTemp);
81  }
82
83  void heater(){
84    digitalWrite(13,HIGH);
85    delay(int(heaterPower));
86    digitalWrite(13,LOW);
87    delay(windowSize - int(heaterPower));
88
89  }
90
91  float getTemp() {
92    int value = 0;
93    double temp = 0;
94    SPI.beginTransaction(SPISettings(2400000, MSBFIRST, SPI_MODE0)
       );
95    digitalWrite(15, LOW);
96    value = SPI.transfer16(0);
97    digitalWrite(15, HIGH);
98    SPI.endTransaction();
99    value = value >> 3; // discard nonsense bits
100   temp = float(value) / 4; // Divide by four for temp in C
101   return temp;
102 }
103
104 void getSetPoint() {
105   static byte inDex = 0;
106   char endMarker = '\n';
107   char currChar;
108
109   while (Serial.available() > 0) {
110     currChar = Serial.read();
111
112     if (currChar != endMarker) {
113       receivedChars[inDex] = currChar;
114       inDex++;
115       if (inDex >= numChars) {
116           inDex = numChars - 1;
117       }
118     }
119     else {
120       receivedChars[inDex] = '\0';
121       inDex = 0;
122     }
123   }
124 }
```

Code for the photodiode for laser intensity measurement:

```
#include <ADC.h>

ADC *adc = new ADC();
float readA;
float readA_sm = 0;
float sum = 0;
float avg_read;
double counter = 1;
float alpha = 0.0001;// tau=10s
float alpha_min = 1.0 - alpha;
bool first = true;
void setup() {
  pinMode(A0, INPUT);
  //pinMode(9, OUTPUT);


}

void loop() {

  readA = (float)adc->analogRead(A0);

  if (first == true){
    readA_sm = readA;
    first = false;
  }
  else{
    //readA=200;
    readA_sm = alpha*readA + alpha_min*readA_sm;

    sum = sum + readA_sm;
    counter= counter + 1;
    if (counter == 250){
      avg_read = sum / 250;
      Serial.println(avg_read);

      counter = 1;
      sum = 0;
    }
  }


  //Serial.println(readA);
```

```
  delay(1);// in ms



}
```

Code for automated separator:

Following is the microcontroller code for the separator written by Dr.Andrew Harvie.

```
/*
Arduino sketch for automated separator.

Written for a Teensy 3.2 (www.pjrc.com/teensy) via teensyduino, but should work on any arduino board that allows
two hardware interrupts - just change the relevant pins.

Two TSL235R-LF light-freqency converters (at 3.3V) are used to monitor light transmission through each separator
output channel. Segmented flow is detected in a given channel by comparing the differential RSD between the
channels. The valve position is updated by a servo.


Andrew J Harvie Feb 2019
 */

#include <Servo.h>
#include <math.h>

//////////////////////////////PARAMETERS TO CHECK ////////////////////////////////////////////////////
//Pin assignment
#define ledPin 13

//Pins for light-frequency converters
//through channel
#define ltfPin1 23
//side channel
#define ltfPin2 22

//servo pin
#define servoPin 9

//Servo travel limits (depends on manufacturer)
#define maxPosition 1240//1240for ODE, Galden system only
#define minPosition 1000
```

```
34
35 ////////////////////////////PARAMETERS TO TUNE
   ////////////////////////////////////////////////////
36 /*
37 Modify the following parameters if separator performance is
   unsatisfactory for a particular
38 solvent system. Instructions on modification are available in
   supporting information.
39 */
40
41 //multiply these two numbers to find how long getRSDs() takes
42 #define samplingTime 30 //it's in ms
43 #define numberBins 200
44
45 //others
46 #define maxSteps 15 // 40*2 for number of degrees turned by
   servo
47 #define accDiffRSD 0.004 //0.002Value of differential RSD to
   accept (no adjustment)
48 #define delayTime 7000 //number of ms to wait before starting a
   new measurement
49 #define P_coeff 2000 //5000 proportional coefficient (*2 for
   value in degrees)
50
51 //
   ////////////////////////////////////////////////////////////////////////////////
52
53 Servo winchServo;
54
55 //specify starting position here (1000 is fully closed)
56 int servoPosition = 1200;// 1240initial adjustment  is important
    for different solvent system
57
58 //arrays for intensity values from each channel
59 int throughCounts[numberBins];
60 int sideCounts[numberBins];
61
62 volatile unsigned long cnt1;
63 volatile unsigned long cnt2;
64 unsigned long last = 0;
65
66 float throughMean = 0.0;
67 float sideMean = 0.0;
68 float throughRSD = 0.0;
69 float sideRSD = 0.0;
70
71 // IRQs for frequency counting
72 void irq1(){
```

```
  cnt1++;
}

void irq2(){
  cnt2++;
}

void setup() {
  pinMode(ledPin, OUTPUT);
  attachInterrupt(digitalPinToInterrupt(ltfPin1), irq1, RISING);
  attachInterrupt(digitalPinToInterrupt(ltfPin2), irq2, RISING);
  winchServo.attach(servoPin, minPosition, maxPosition);
  //intitialise servo position
  winchServo.writeMicroseconds(servoPosition);
  Serial.begin(9600);
  digitalWrite(ledPin, HIGH);
}

void loop() {
  //delay between iterations
  delay(delayTime);

  // update RSD values
  getRSDs();

  //calculate differential RSD
  float diffRSD = throughRSD - sideRSD;

  //absolute value
  float incorrectitude = abs(diffRSD);

  //decide number of steps
  int steps = int(incorrectitude * P_coeff);

  //decide direction
  if(diffRSD > accDiffRSD){
    tighten(steps);
  }
  else if (diffRSD < -1*accDiffRSD){
    loosen(steps);
  }

  // Monitoring
  Serial.print(throughRSD, 5);
  Serial.print(" ");
  Serial.print(sideRSD, 5);
  Serial.print(" ");
  Serial.print(diffRSD, 5);
  Serial.print(" ");
```

```
122   Serial.println(servoPosition);
123
124
125 }
126
127
128 void loosen(int steps){
129   //increases pwm value (opens valve) more through channel
130   if (steps > maxSteps){
131     steps = maxSteps/2;
132   }
133   servoPosition = servoPosition + steps;
134   // check if outside servo range
135   if (servoPosition > maxPosition){
136     servoPosition = maxPosition;
137     //errorlight();
138   }
139   // set position
140   winchServo.writeMicroseconds(servoPosition);
141 }
142
143 void tighten(int steps){
144   //decreases pwm value (closes valve) more side channel
145   if (steps > maxSteps){
146     steps = maxSteps;
147   }
148   servoPosition = servoPosition - steps;
149   // check if outside servo range
150   if (servoPosition < minPosition){
151     servoPosition = minPosition;
152     errorlight();
153   }
154   // set position
155   winchServo.writeMicroseconds(servoPosition);
156 }
157
158 void getRSDs(){
159   //updates values of global RSDs
160
161   digitalWrite(ledPin, HIGH);
162   int throughSum = 0;
163   int sideSum = 0;
164   float throughSquareSum = 0;
165   float sideSquareSum = 0;
166
167   last = millis();
168
169   //populate arrays of light intensity vs time
170   for(int i = 0; i < numberBins; ++i){
```

```
171     //reset counters
172     cnt1 = 0;
173     cnt2 = 0;
174 
175     // timing
176     while(millis() - last < samplingTime){
177       //don't do anything - waiting on interrupt counters
178       //this is better than using delay() which sometimes
      behaves badly with interrupts
179     }
180 
181     int grab1 = cnt1;
182     int grab2 = cnt2;
183 
184     //add to array
185     throughCounts[i] = grab1;
186     sideCounts[i] = grab2;
187 
188     //increment sum (for calculation of mean)
189     throughSum = throughSum + grab1;
190     sideSum = sideSum + grab2;
191 
192     last = millis();
193 
194   }
195 
196   //calculate means
197   throughMean = float(throughSum)/float(numberBins);
198   sideMean = float(sideSum)/float(numberBins);
199 
200   //calculate  RSDs
201   for(int i = 0; i < numberBins; ++i){
202     throughSquareSum = throughSquareSum  + sq(throughCounts[i] -
      throughMean);
203     sideSquareSum = sideSquareSum  + sq(sideCounts[i] - sideMean
     );
204   }
205 
206   throughRSD = sqrt(throughSquareSum/float(numberBins)) /
     throughMean;
207   sideRSD = sqrt(sideSquareSum/float(numberBins)) / sideMean;
208 
209 }
210 
211 void errorlight(){
212   //flash light 5 times if there's an error (usually reached max
      servo travel)
213   for(int i = 0; i<5; ++i){
214     digitalWrite(13, HIGH);
```

```
215     delay(10);
216     digitalWrite(13, LOW);
217     delay(10);
218   }
219
220 }
```

APPENDIX B

MATLAB CODE FOR CONTROL THE AUTOMATED REACTOR COMPONENTS

Code for the heater :

Matlab code written to read and set the temperature for the built solid-state heater.

```
function avg_temp =  reactiontemp(cmd,temp)

heater=serialport('/dev/cu.usbmodem65590501',9600); %heater at
    lab

configureTerminator(heater,13)

switch cmd
    case 'read'
        temps=zeros(1,5);
        readout = str2num(readline(heater));
        target_temp= readout(1);
        for i=1:5
            feedback = str2num(readline(heater));
            pause(0.2)
            temps(i)=feedback(2);
        end
        avg_temp = mean(temps);
        fprintf('Target temp:%.2f, current temp: %.2f\n',
    target_temp,avg_temp);
    case 'set'
        if temp > 245
            fprintf('Temperature exceeds reactor limit\n');
            return
        else
            set_target = sprintf('%s\n',num2str(temp,'%.2f'));
            writeline(heater,set_target)
            pause(1)
            double_check=str2num(readline(heater));
            if temp ~= double_check(1)
```

```
                writeline(heater,set_target)
            end
            fprintf('Setting reactor to %.2f\n',temp);
        end

end


clear heater
end
```

Code for controlling the syringe pump:

Matlab code for sending appropriate serial commands for controlling the syringe pump.

```
function reply= KDpumpcontrol(device,cmd,f)

configureTerminator(device,13);
writeline(device,'NVRAM NONE');
pause(1);

switch cmd

    case 'set'
        writeline(device,'ctvolume')
        pause(0.5)
        command = sprintf('irate %d ul/min',f);
    case 'run'
        command = 'irun';
        fprintf('Pumping')
    case 'stop'
        command = 'stop';
        fprintf('Stopping')
    case 'crate'
        command ='crate';
    case 'set refil'
       writeline(device,'cvolume')
       pause(0.5)
       command = sprintf('wrate %d ml/min',f);
       %command = 'wrate 10 ml/min';
        %writeline(device,'rrun')
        %pause(60);
    case 'refil'
        volume = sprintf('tvolume %d ml',f);
        writeline(device,volume)
```

```
        pause(0.5)
        command = 'wrun';

end
writeline(device,command);

bytes = 0;

while bytes == 0
    bytes = device.NumBytesAvailable;
    pause(0.5);
end
pause(2)
reply = read(device,device.NumBytesAvailable,'string');
fprintf(reply);


end
```

Code for the reagent delivery and heating:

Matlab code for synchronising the syringe pump and heater to set the reaction parameters.

```
function runReaction(cmd,RT,temp)
%% Setting up pumps and calculate flow rate


fomblin_pump = serialport('/dev/cu.usbmodemD2021801',115200);
precursor_pump= serialport('/dev/cu.usbmodemD2018621',115200);
valves= serialport('/dev/cu.usbmodem66385501',9600);
pause(2)
%% Check flowrate
%confirming the rate
%in uL, use a t splitter

switch cmd
    case 'run'

        reactor_volume = 250*pi*1.5;
        total_flowrate = reactor_volume./(RT./60); %in uL
        precursor_rate = total_flowrate./2; %in uL
        fomblin_rate = total_flowrate./2;
        KDpumpcontrol(fomblin_pump,'set',fomblin_rate);%fomblin
   rate
```

```
21        fprintf('Setting Galden flow rate to  %f ul/min\n',
  fomblin_rate);
22        KDpumpcontrol(precursor_pump,'set',precursor_rate);%
  precursor rate
23        fprintf('Setting Precursor flow rate to  %f ul/min\n',
  precursor_rate);
24        curr_temp = reactiontemp('read');
25        pause(3)
26        reactiontemp('set',temp)
27        fprintf('Setting Temperature from %f to %f\n',curr_temp,
  temp);
28        logfid = fopen('log.txt','a+');
29        fprintf(logfid,'%s Setting condition %.2f RT %.2f Temp\n
  ',datetime,RT,temp);
30        fclose(logfid);
31        while (curr_temp>temp+20 || curr_temp<temp-20)
32            %reactiontemp('set',temp)
33            pause(20)
34            curr_temp =reactiontemp('read');
35            %pause(1)
36        end
37        KDpumpcontrol(precursor_pump,'run')
38        KDpumpcontrol(fomblin_pump,'run')
39    case 'refil'
40        writeline(valves,'1')
41        pause(10)
42        %change valve position to refil
43        KDpumpcontrol(precursor_pump,'set refil',2);
44        KDpumpcontrol(fomblin_pump,'set refil',1.5);
45        %4 RT = 2.35 ml consumption
46        KDpumpcontrol(precursor_pump,'refil',31)
47        KDpumpcontrol(fomblin_pump,'refil',31)
48        pause(40*60)
49        writeline(valves,'0')
50        pause(10)
51        logfid = fopen('log.txt','a+');
52        fprintf(logfid,'%s refilled 31 ml\n',datetime);
53        fclose(logfid);
54        %change valve position to infusion
55    case 'pause'
56        KDpumpcontrol(fomblin_pump,'stop')
57        KDpumpcontrol(precursor_pump,'stop')
58    case 'stop'
59        KDpumpcontrol(fomblin_pump,'stop')
60        KDpumpcontrol(precursor_pump,'stop')
61        reactiontemp('set',22);
62        logfid = fopen('log.txt','a+');
63        fprintf(logfid,'%s Stopped\n',datetime);
64        fclose(logfid);
```

```
    case 'clean'
        KDpumpcontrol(fomblin_pump,'set',250)
        KDpumpcontrol(fomblin_pump,'run');
        KDpumpcontrol(precursor_pump,'stop');
        reactiontemp('set',22);
    case 'cold_run'
        KDpumpcontrol(fomblin_pump,'set',200)
        KDpumpcontrol(precursor_pump,'set',200)
        KDpumpcontrol(fomblin_pump,'run');
        KDpumpcontrol(precursor_pump,'run');
end
end
```

Code for the optical detection system:

Matlab code for controlling the optical detection system, including reading the photodiode measurement and spectrometer recording of the emission spectrum.

```
function [raw_wave,raw_int,laser_int] = SNR_spectra_pd(ratio,
    maxitr)
%% Setting up spectrometer
current_python = pyversion;
wantedversion = '3.8';

if strcmp(current_python,wantedversion) == 0
    py_env = pyenv ('Version','/opt/anaconda3/bin/python');
else
end
import py.seabreeze.*;
spectro = py.seabreeze.spectrometers.Spectrometer.
    from_first_available;
pd=serialport('/dev/cu.usbmodem65619601',9600);
configureTerminator(pd,13);


% spectro.tec_set_enable(1);
spec_temp = spectro.tec_get_temperature_C;
if spec_temp > -4
    spectro.tec_set_temperature_C(-5);
    spectro.tec_set_enable(1)
    while spec_temp >= -5
        spec_temp = spectro.tec_get_temperature_C;
        pause(1)
    end
end
fprintf('Spectrometer cooled to %f\n',spec_temp)
```

```
27
28 background = readmatrix('/Users/DeviceOJ/Desktop/NTNU/V2021/
       Spectrometer Data/dark_cooled-5
       _3000_averaged_with_1s_integrationtime.txt');
29 background = background(:,2)';
30 background(787:801) = [];
31
32 %% Getting raw spectrum wtih signal to noise ratio
33
34 Imin = 500;
35
36 Imax = 900;
37 %wavelength index
38 spectro.integration_time_micros(1000000)%500000=500ms
39 counter = 1;
40 avgint = double(spectro.intensities);
41 avgint(787:801) = [];%laser second  harmonic
42 avgint = (avgint - background);
43 wave = double(spectro.wavelengths);
44 wave(787:801) = [];%laser second harmonic
45 raw_wave=wave(2:end-4)';
46 N = 900;
47 signal = median(avgint(Imin:Imax));
48 slice1 = avgint(Imin:N-4);
49 slice2 = avgint(Imin+2:N-2);
50 slice3 = avgint(Imin+4:N);
51 noise = 0.6052697.*median(abs(2.*slice2-slice1-slice3));
52 signalnoise = signal/noise;
53
54 while signalnoise < ratio
55     spectro.integration_time_micros(1000000)
56     newint = double(spectro.intensities);
57     newint(787:801) = [];%laser second harmonic
58     newint = (newint - background);
59     avgint = (counter.*avgint + newint)/(counter+1);
60     % time synchronous average
61     %a=1/N;
62     %avgint = (1-a).*avgint+newint*a;
63     signal = median(avgint(Imin:Imax));
64     slice1 = avgint(Imin:N-4);
65     slice2 = avgint(Imin+2:N-2);
66     slice3 = avgint(Imin+4:N);
67     noise = 0.6052697.*median(abs(2.*slice2-slice1-slice3));
68     signalnoise = signal/noise;
69     counter = counter +1;
70     if counter == maxitr
71         break
72     end
73 end
```

```
74
75 raw_int=avgint(2:end-4)';
76 flush(pd);
77 pause(1)
78 laser_int =str2num(readline(pd));
79 logfid = fopen('log.txt','a+');
80 fprintf(logfid,'%s Spectrum taken with %d averages\n',datetime,
       counter);
81 fclose(logfid);
82 disp(counter);
83 disp(signalnoise);
84
85 clear pd
86 end
```

Code for the automated synthesis:

Parent script to carry out automated synthesis with optical detection, the script returns measured optical properties as output.

```
1  function output = simple_synthesis(RT,temp)
2  output=[];
3  for i=1:length(RT)
4      delta_t=4*RT(i);
5      runReaction('run',RT(i),temp(i));
6      logfid = fopen('log.txt','a+');
7      fprintf(logfid,'%s Running condition %.2f seconds %.2f
       degree C\n',datetime,RT(i),temp(i));
8      fclose(logfid);
9      pause(delta_t);
10 %      runReaction('pause'); stopping to aquire spectra
11 %      pause(3)
12     [raw_wave,raw_int,laser] = SNR_spectra_pd(290,30);
13     %runReaction('clean')
14
15 %% process spectra
16     wave = raw_wave(300:1020);
17     int = raw_int(300:1020);
18     max_int = max(int);
19     pw = wave(int==max_int);
20     halfMax= (min(int)+max_int)/2;
21     index1 = find(int >= halfMax, 1, 'first');
22     index2 = find(int >= halfMax, 1, 'last');
23     fwhm = wave(index2)-wave(index1) + 1;
24     result=[max_int/laser,pw,fwhm];
25     output(i,:)=result;
```

```
    disp(result)
    %% Write file
    path = '/Users/DeviceOJ/Desktop/NTNU/V2021/Spectrometer Data
   /SNOBfit7/';
    name = sprintf('%s-CuInS2-%.2fseconds-%.2fC.txt',datetime,RT
   (i),temp(i));
    fID = fopen([path name],'w+');
    for k = 1:length(raw_wave)
        fprintf(fID,'%f %f %f\n',raw_wave(k),raw_int(k),laser);
    end
    fclose(fID);
end
disp(output)
end
```

Code for self-optimising synthesis with refilling:

Script for carry out self-optimising synthesis with SNOBFit, with reflling after every 12 points measured.

```
close all
clc

import snobfitclass.*
simple_CIS = snobfitclass.snobclass();
simple_CIS.name = 'CIS_unconstrained_675';
simple_CIS.fcn = 'simple_CIS';
simple_CIS.continuing=0;
simple_CIS.x_lower = [140,160];
simple_CIS.x_upper = [360,185];
simple_CIS.ncall = 12;
logfid = fopen('log.txt','a+');
fprintf(logfid,'%s Starting an optimisation!\n',datetime);
fclose(logfid);
simple_CIS.startExp;
simple_CIS_phase_1 = simple_CIS;
reactiontemp('set',22);
logfid = fopen('log.txt','a+');
fprintf(logfid,'%s Setting reactor to 22 C\n',datetime);
fclose(logfid);
pause(80)
runReaction('stop')
pause(40)


for i = 2:3
```

```
    logfid = fopen('log.txt','a+');
    fprintf(logfid,'%s starting refilling round %d\n',datetime,i
    );
    fclose(logfid);
    runReaction('refil') %refil 31ml
    pause(60)
    runReaction('cold_run')%pushes back to infusion
    pause(600)
    simple_CIS.continuing=1;
    simple_CIS.ncall = i*12;
    simple_CIS.termination = 'n_runs';
    simple_CIS.startExp;
    logfid = fopen('log.txt','a+');
    fprintf(logfid,'%s %d SNOBfit run completed\n',datetime,i);
    fclose(logfid);
    eval(sprintf('simple_CIS_phase_%d = simple_CIS', i));
    reactiontemp('set',22);
    logfid = fopen('log.txt','a+');
    fprintf(logfid,'%s Setting reactor to 22 C\n',datetime);
    fclose(logfid);
    pause(80)
    runReaction('stop')
    pause(50)
end
```

Objective functions used for wavelength and intensity optimisation:

Objective functions used for self-optimising synthesis, here the intensity optimisation is commented out.

```
function f = simple_CIS(SNOB)

    RT = SNOB.next(:,1);
    temp = SNOB.next(:,2);
    output = simple_synthesis(RT,temp);%first should be
    intensity
    %output = synthesis_simulator(RT,temp);
    f = (output(:,2)-675).^2; %wavelength opt
    %f = 355-output(:,1);%intensity opt
    %f = output(:,1);
    SNOB.valuesToPass = output;
end
```

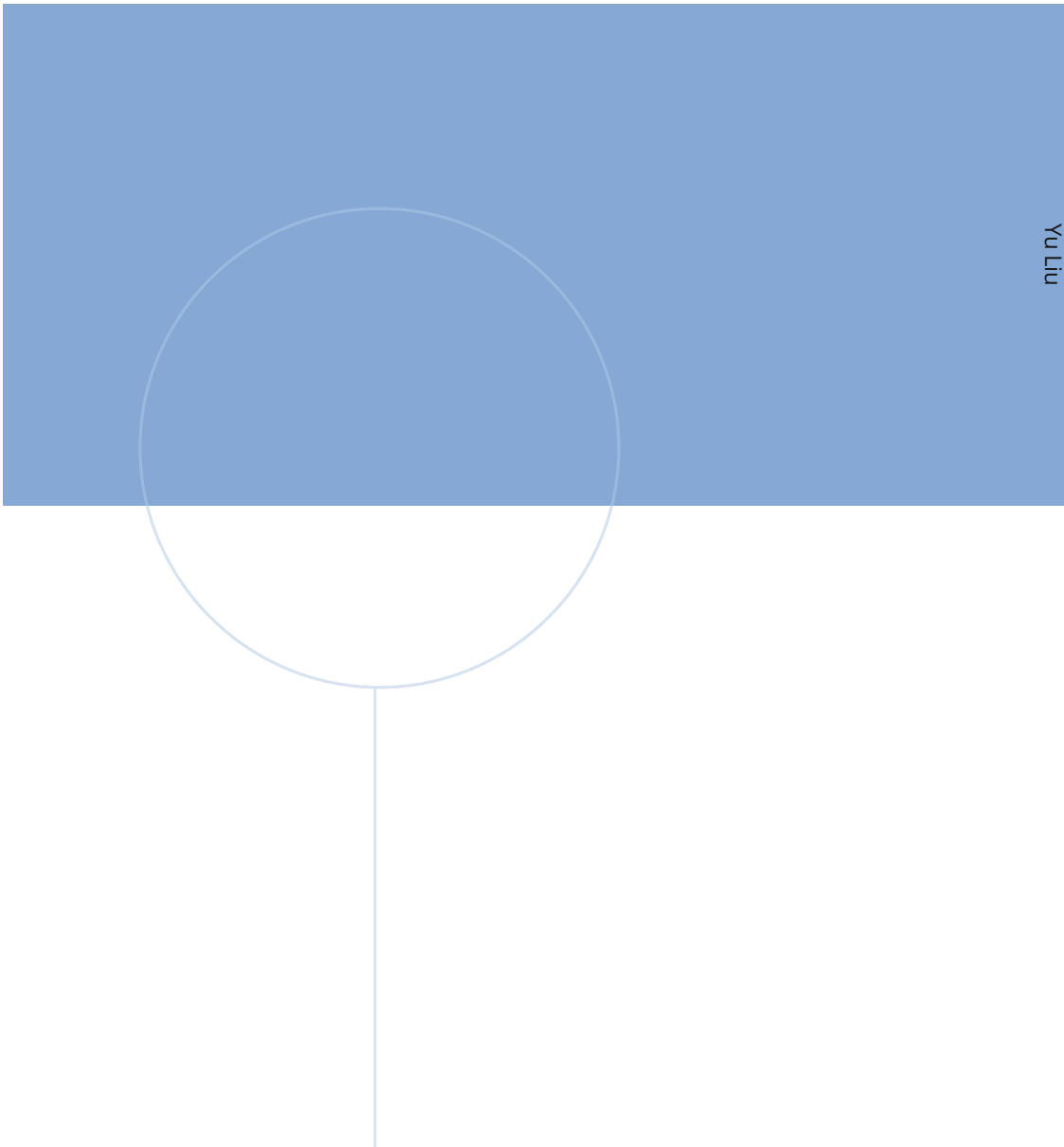

Yu Liu

NTNU
Norwegian University of
Science and Technology